Simulating Pump Rejection Filters For Integrated Photonic Quantum Information Processing

By

ALEXANDER IAIN FLINT

Department of Physics
UNIVERSITY OF BRISTOL

A dissertation submitted to the University of Bristol in accordance with the requirements of the degree of MASTER OF SCIENCE BY RESEARCH in the Faculty of Science.

JUNE 2021

Word count: 15784

Abstract

Quantum information technologies have wide-ranging and novel applications. A promising approach to their implementation is the use of integrated photonics. For this application, integrated photonic chips require the creation and detection of single photons. Nonlinear processes used in the creation of heralded single photons, such as spontaneous four-wave mixing, require effective rejection filtering of bright pump light. In this work, micro-ring resonators in SOI are explored in this filtering capacity. Simulations of these resonators with the addition of absorptive nanowires were produced. The nanowire has the effect of reducing build-up of the electric field within the ring, increasing extinction and suppressing unwanted nonlinear effects within the cavity. Simulations of these rings with $MoSi$, Cr and NbN nanowires were conducted. Systems made up of $N \leq 3$ rings in a cascaded configuration are examined for their filtering properties. The maximum extinction recorded was found to be 46.8dB in a three-ring design with $3\mu m$ of $MoSi$ nanowire deposited with width $400nm$ and height $4.7nm$. The maximum FWHM presented for these rings is $1.8nm$. The advantages and disadvantages of this approach are discussed, materials are compared, and suggestions for further work are made.

COVID-19 STATEMENT

The following is a Covid-19 Statement in conjunction with Annex 17 of the Regulations and Code of Practice for Research Degree Programmes.

The original plan for this research project was to work towards the fabrication of pump rejection filters consisting of ring resonators with deposited nanowire. To this end, the first months of the research year (October 2019-February 2020) were focused on the calculations, training and induction for cleanroom processes and lithographic designs. This preparation included a lecture course in nanofabrication and laser and cryogenic safety training and preparation. Unfortunately, this research plan was deemed not viable due to public health restrictions and university policy on working remotely. These policies meant that the university cleanroom would not be available and all lab work was suspended. As a consequence, in March 2020, the project was pivoted to focus on the simulations of devices. This was the case until the end of the research year (October 2020). The specific fabrication skills gained up to that point were, therefore, not applicable to the work. Instead, the project required familiarisation with simulation techniques and software. This necessary development limited the amount of time available to complete the simulations. In this thesis, suggested fabrication techniques are briefly reviewed as the result of the earlier work in this project. Suggestions are made for their implementation. However, as no findings were collected as a result of the original research plan, all the results presented here are the results of the simulations.

Dedication and acknowledgements

This year has been pretty hectic for everyone. The spread of coronavirus has made everything difficult, taking away alot of the fun of working, chatting and sharing in person with friends, colleagues and family. It is particularly important that I express my thanks to my supervisors Döndü Sahin and Edmund Harbord for their guidance and support in navigating this constantly changing environment. I would like particularity to thank Edmund for his advice and encouragement throughout this year, particularly around PhD applications. Although cut short by the lockdown, I thoroughly enjoyed my few months working around QETLabs.

This year has been particularly rough for more reasons than the pandemic. My dad's cancer diagnosis was a big shock, especially considering that everyone considers him to be the fittest man alive. His remarkable recovery and general refusal to let it beat him down was truly inspiring. I've never been prouder to be his son. A very special thank you to the doctors and nurses at the Great Western. I've never been more grateful to live in a country where healthcare is free. Recently we've all seen how important that principle is. Those NHS workers save lives and don't get given anything close to what they deserve.

Thanks to my flatmates for not killing me after three months in the same flat, without the option to leave. Finally, thank you to Mum and Dad for proofreading and making me cups of tea.

To dad, for getting through.

AUTHOR'S DECLARATION

I declare that the work in this dissertation was carried out in accordance with the requirements of the University's Regulations and Code of Practice for Research Degree Programmes and that it has not been submitted for any other academic award. Except where indicated by specific reference in the text, the work is the candidate's own work. Work done in collaboration with, or with the assistance of, others, is indicated as such. Any views expressed in the dissertation are those of the author.

SIGNED: ..... DATE: .....

TABLE OF CONTENTS

List of Tables

Table **Page**

List of Figures

CHAPTER 1

INTRODUCTION

Quantum information technologies are technologies that harness the properties of quantum mechanical systems that result in exciting and novel applications. These technologies have a range of applications. These include quantum computation [1–4], quantum key distribution, and others [5, 6]. This work is focused on the use of silicon photonics to the implementation of these technologies.

Quantum information technologies have been theorised for decades, notably by Feynman in 1982 [7]. The limitation of classical computation to simulate quantum systems spawned the birth of quantum information research, incorporating quantum computation. In brief, encoding information as qubits rather than in classical bits allows for a broader range of problems to be solved. As opposed to classical bits, which can hold a value of 0 or 1, a qubit can hold values of 0, 1 or some superposition of 0 and 1. This allows for new ways of solving problems. A comprehensive examination of quantum information theory and quantum computation can be found in [8]. Methods of quantum computation and various algorithms have been produced [8–10] with potentially transformative effects on the modern world. Examples include Shor's algorithm for fast prime factoring [9] with vast implications for fields such as cryptography. Grover's search algorithm for searching databases is another example [10].

Aside from work towards useful quantum computers, there has been promising work in the field of quantum key distribution (QKD) [5, 8]. QKD protocols for encryption work on the basic idea that an observation on a quantum state changes it. This can result in encryption systems which are physically secure, subject only to our current understanding of quantum mechanics. This differs from current encryption protocols which rely on the idea that the encryption is unbreakable only because of the resources currently available. These methods hold firm, for the time being, with classical computing techniques. However, this is fundamentally threatened

by ideas such as Shor's algorithm which could potentially be used to break these encryption protocols.

Quantum information systems have been demonstrated on a range of platforms including superconducting qubits [3], trapped ions [1] and others [4]. However, there are key problems that remain when trying to scale to large numbers of qubits. For instance, in order for algorithms to be implemented to a degree to solve problems faster than any current classical computing, a large number of qubits are required (of the order of 10^9) [11]. Therefore attention has been drawn to the design and fabrication of platforms which minimise the problems of scaling, as well as being easy to implement with current manufacturing practices. All the platforms have their advantages and disadvantages for different applications. This work is focused on the integrated photonic platform, namely filters for such systems. In particular this thesis focuses on the use of silicon photonics and the implementation of these quantum technologies with the advantages in readiness, in technological use, scaling, cost and the maturity of fabrication of said platform.

1.1 Integrated Photonics

Integrated photonics is a relatively mature field, having benefited from pioneering work since the 1980s, motivated by integration with electronic devices, as well as on improving communication techniques [12]. For this work, it is key that integrated platforms can also be used for quantum technological applications. The photon is a promising candidate for a qubit. The state can take advantage of different paths in a chip or polarisation [13]. Additionally, photons suffer very little decoherence [14], an essential problem with other approaches. Advances such as addressing the optical CNOT gate [15, 16] and others have demonstrated the optical routes potential in this area. Some of these demonstrations have been shown using bulk optical setups. This has been effective in demonstrating the key concepts, yet the problems of scale as well as coupling losses and the high stability required for quantum experiments still remain. Recent advances in areas such as single-photon detectors have meant that experiments can be done in the telecommunications wavelengths on integrated devices.

1.2 Quantum Information with Silicon Integrated Photonics

Silicon possesses some desirable properties for integrated photonics. Firstly, silicon is transparent at telecommunications wavelengths ($\sim 1550nm$) [17], where infrastructures exist for classical optical communications. Additionally, as the vast majority of integrated circuits are silicon-based, integration with electronics is more feasible, which will enable fully operational device production as well as compact design options. This provides a cost effective alternative. Silicon's third-order non-linearity allows for some desirable effects such as spontaneous four-wave mixing (SFWM), a process utilized for photon pair generation [18]. Single photon generation is vital for quantum technological applications. Silicon is not the only platform which can be used for integrated optical

quantum information processing. There have been many notable demonstrations in materials such as GaAs [19], silicon nitrate [20], and others [21]. They all have their advantages in the areas of compactness, non-linear and linear effects, optical confines as well as manufacture and integration into other technologies. An important challenge in quantum optics is effective filtering. High extinction filters are required. As these technologies require the use of single photons, they must be shielded from inevitable noise in the system. In order for effective use, detectors need to operate with minimal unwanted detection. As some sources of single photons, such as those which rely on SFWM, require bright pump light, filters in the system are needed to suppress these pump photons. The filters need to perform this task without incurring losses that significantly affect detection of the wanted photons. This is a major challenge for the photonic approach.

This work is focused on the use of micro-ring resonators (MRR) in this filtering application. Here, ring resonators are explored with the addition of absorptive nanowires. These nanowires change the spectral properties of the filters. It is proposed that deposition of said nanowires could result in desirable filtering characteristics when added as a post process in the fabrication stage. Materials that are used in superconducting single nanowire photon detectors (SNSPDs) could be deposited at the same stage as the deposition for detectors. This would result in a simplified fabrication process.

CHAPTER 2

THEORY AND BACKGROUND

This section will outline the theory and background of the photonic devices discussed in this work. It will start with brief introductions to some crucial properties of silicon as a waveguiding material. It will move onto waveguides and their integration into an Silicon-on-Insulator (SOI) platform. A simple ray model will be used to outline the key concepts of guided optics. Then some of the relevant electromagnetic theory will be outlined. This theory will become useful when reviewing the FDTD simulation method. Theory specific to the optical devices in this project will be briefly discussed. These include directional couplers. Ring resonators will be addressed in detail as well as the effect of absorptive nanowires and their use as on-chip filters.

2.1 Silicon as an Optical Material

Silicon (Si) is a semiconductor. It's properties for use in integrated circuits are well known. It can be both grown incredibly pure and easily doped. It is mechanically robust, which becomes increasing import at smaller scales. However, its main benefit as a material, in an industrial capacity, is the significant infrastructure available for its fabrication and the cost savings that infrastructure enables. For this project's focus, it is important to lay out some of its properties as an optical medium.

Silicon is transparent at telecommunication wavelengths in the near-infrared ($\sim 1.5\mu m$). This feature is of benefit for use with systems that work around the standard communications infrastructure. The losses in a silicon chip tend to be reliant on the results of its fabrication processes. Effects such as surface roughness (generally a result of the etching process) dominate over intrinsic absorption in the material [17, 22].

There is a range of linear and nonlinear effects in silicon. Linear and nonlinear, in this context, refer to the relationship between the polarisation density of the material and the electric field

present [17]. The polarisation density refers to the density of induced electric dipole moments in the material. This concept can be described by the power series expansion of the dielectric polarisation density (**P**) with respect to the electric field (**E**).

$$\mathbf{P}(E) = \epsilon_0(\mathbf{E}\chi^{(1)} + \mathbf{E}^2\chi^{(2)} + \mathbf{E}^3\chi^{(3)}.....) \tag{2.1}$$

Here ε_0 is the permittivity of free space, a fundamental constant. A linear material will have a dependence on the first tensor term ($\chi^{(1)}$) only. Second-order nonlinearity has a dependence on the second tensor term ($\chi^{(2)}$) and so on. Properties that result from these nonlinearities can be both desired and undesired for optics [23], depending on the application. Crystalline silicon has significant third-order nonlinearity. This nonlinearity results in processes such as two-photon absorption (TPA) and spontaneous four-wave mixing (SFWM) [24]. There are also linear effects, such as free carrier absorption.

How light travels through a material can be described in terms of its complex refractive index $\tilde{n}$. The refractive index is a dimensionless quantity which describes its speed and attenuation through a material.

$$\tilde{n} = n + i\kappa \tag{2.2}$$

The real part of this quantity describes the propagation within the material, and the complex part describes the attenuation. As can be seen in figure 2.1, the complex part κ is low at wavelengths greater than $500nm$. This indicates low absorption in the material at these wavelengths. The relation between the value of κ and the absorption per unit length, α (μm^{-1}) is as follows,

$$\alpha = \frac{4\pi\kappa}{\lambda} \tag{2.3}$$

An important effect to note in silicon is the thermo-optic effect. This effect refers to the changing of the refractive index by changing the temperature. Heating affects the density of dipole moments. This, in turn, changes the polarity and therefore increases the refractive index. In silicon, the rate of change of refractive index is as shown [26].

$$\frac{dn}{dT} = 1.8 \times 10^{-4} K^{-1} \tag{2.4}$$

This means that the phase can be modulated using an active heater [27]. This effect is a key componet in a range of devices in silicon photonics. For example as phase shifters in Mach-Zehnder Interferometers (MZI) [28].

As an optical medium, there are some drawbacks with silicon. It lacks other nonlinearities which limit its applications. As mentioned, the major loss contribution in silicon waveguides

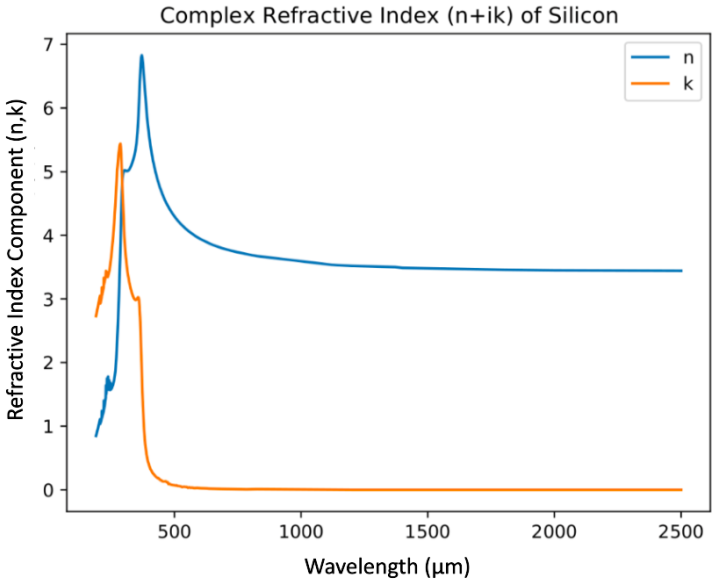

Figure 2.1: Graph showing the variation of the complex refractive index of silicon. Data is taken from [25]

result from its fabrication characteristics. Although systems of manufacture are relatively mature, when devices are produced at the sub-micron scale, fabrication issues become more present. Additionally, as an indirect bandgap material, silicon is less efficient as an optical source. However, as mentioned before, high $\chi^{(3)}$ nonlinearity is present in silicon and that is used to generate a photon pair. This pair are traditionally called signal and idler. They are generated by SFWM where an idler photon is detected to herald a signal photon.

2.2 Single Photon Devices

From an implementation standpoint, some of the challenges with a photonics approach to quantum information is the creation, filtration and detection of single photons. These challenges are complicated further when working on an integrated platform. Reliable and accurate detection methods are required for some key proposed applications. Here, some of the approaches that can be taken will be discussed.

2.2.1 Single Photon Detectors

Single-photon detectors have been demonstrated in several ways. For example, photomultiplier tubes [29] and avalanche photodiodes are available [30] and are useful for many applications. Photomultiplier tubes are vacuum tubes with a photocathode, anode, and an arrangement of

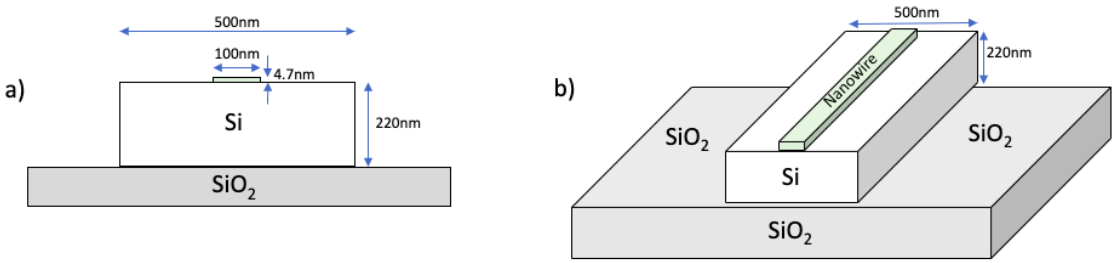

Figure 2.2: Diagram of an SOI waveguide with a nanowire deposited ontop.

dynodes. As a photon hits the photodiode, an electron is released. This electron accelerates towards a dynode which emits secondary electrons which are accelerated towards the next dynode. This process continues until the electrons are registered as a sharp current increase at the anode. Avalanche photodiodes are photodiodes which utilise a high reverse bias voltage and the avalanche breakdown in semiconductors to register a detection. [30]. These, however, suffer from various effects such as dark counts (unwanted photon detection) and jitter (time deviation from the ideal detection). Integration and scalability are also factors (PMTs are bulky devices) [31]. Loss rates can be substantial.

One of the most promising methods are Superconducting Nanowire Single-Photon Detectors (SNSPDs) [31, 32]. They consist of a nanowire deposited atop a waveguide as seen in figure 2.2. These have shown promising characteristics in common areas used to analyse previous sources [33, 34]. These include reduced jitter, dark count rates, efficiency (percentage of photons actually detected), dark time (time that the detector cannot detect after a detection) and the working wavelength range. A drawback is that the operating temperatures are cryogenic with current materials. This means bulky apparatus is required. SNSPDs can be understood by considering a hotspot model [31, 35]. In brief, as a photon is absorbed into the superconducting nanowire through evanescent coupling, the resistivity in the material changes. A hotspot of resistance is formed in the superconductor, and the resistance increases. This resistance can be measured electronically, thus registering a detection. Detailed explanations of the implementation and the hotspot model can be found in [31, 34, 35]. The presence of the nanowire and the coupling affects the optical properties of the waveguide underneath it. It is this which inspires the filtering method which is the subject of this work. Previous work at Bristol demonstrated enhancement of detection efficiencies by placeing the nanowire in an MRR cavity [36]. Superconducting materials which have been used for the nanowires include nibium nitrate (NbN) [32, 37] and NbTiN [38] as well as amorphous alloys such as tungsten silicide (WSi) [39] and molybdenum silicide ($MoSi$) [40].

2.2.2 Photon Sources

For the effective implementation of quantum photonics, a reliable source of single photons is required. There has been good progress in this field in the last few decades. Sources that have been proposed include trapped ions [41] atoms [42] and quantum dots [43]. Another promising process for implementation in silicon is SFWM [18, 44–46].

2.2.2.1 Spontaneous Four-Wave Mixing (SWFM)

As mentioned, SFWM takes advantage of the third-order nonlinearity in silicon. It was first demonstrated in silicon in 2006 by Sharping et al. [47]. As it is a phenomenon of silicon itself, integration into a chip is inherent. It occurs when two photons of a given wavelength combine producing two quantum correlated photons of two different wavelengths. This interaction depends on a phase-matching condition along with momentum conservation [48] as described, in the degenerate case, by ,

$$2\omega_p = \omega_i + \omega_s \tag{2.5}$$

where ω_p ω_i and ω_s are the angular frequencies of the pump (input), signal and idler photons respectively. The case shown in equation 2.5 is known as degenerate SFWM, due the use of two pump photons of the same frequency. This effect has been shown as a useful source of photons, yet effective filtering is required, especially for the pump light present.

There are some key drawbacks with SFWM. The generation of a useful quantum state in this way is a probabilistic process. Therefore, there is a possibility that when pumped: zero, one or multiple states are produced. This unpredictability adds to the noise in a system and means that it is not a necessarily "on-demand" source, a key drawback for technological applications. Additionally, although a useful process in a designed source, SFWM in a chip where it is not expected can result in unwanted noise in experiments, and errors in information processing.

SWFM can be implemented in a number of ways. Across platforms, this is generally done by confining pump light into some form of optical cavity. These include such schemes as fibre Bragg gratings (FBG) and MRRs. The key characteristics of a SWFM are its Purity (which characterises the amount of spectral correlation between the generated photons in the pair) alongside the statistics of emission. The purity can be determined experimentally by the Joint Spectral Intensity. This is not discussed deeply in this work but in-depth explanations can be found [49].

2.3 Filters For Integrated Silicon Photonics

For effective photonic platforms for applications such as quantum information processing, effective filtering of photons is required. Pump processes, such as SFWM, result in unwanted bright pump

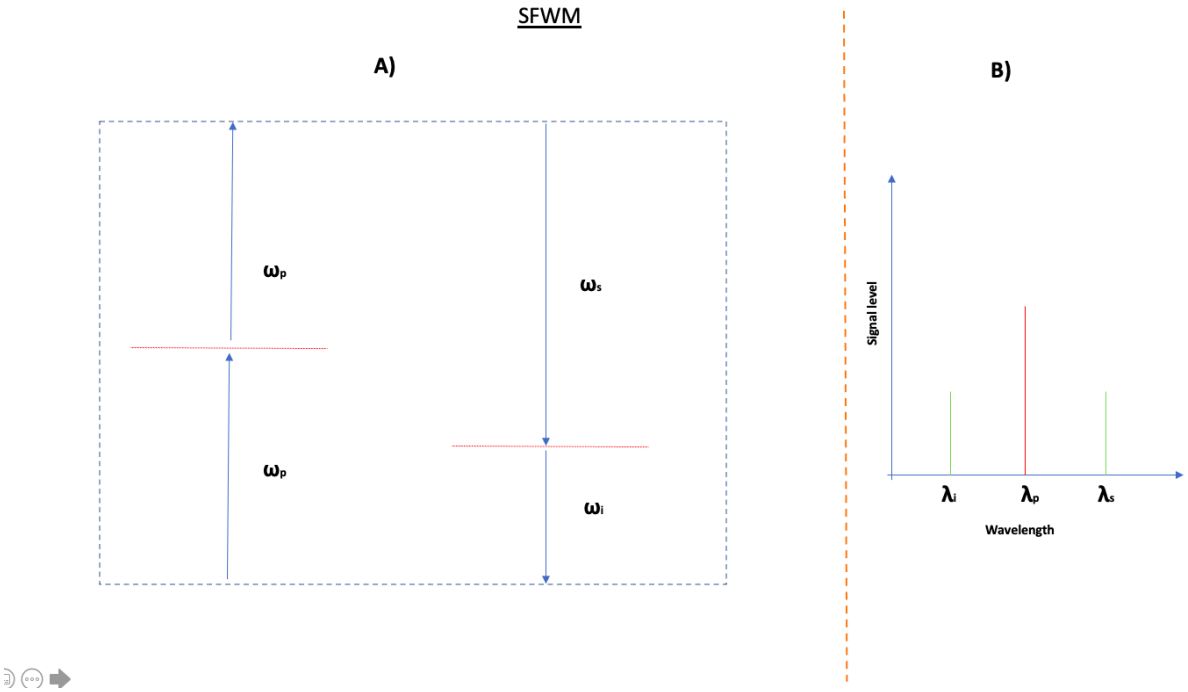

Figure 2.3: A) Simple energy diagram of the process of SWFM. Here two photons spontaneously combine and then convert to two others with different frequencies. B) Diagram showing to resulting spacing of the wavelength of the photons. Red peak (λ_p) shows the pump photons.

photons left in the system [50]. In this section, devices for the filtering and suppression of pump wavelength are discussed. These devices include distributed Bragg reflector based devices (BR), MZIs and MRRs.

2.4 Filtering Characteristics

There are a range of parameters which need to be optimised for effective filtering for pump rejection as described. The first and most obvious for quantum applications is the extinction ratio. This is the ratio of the passband to the minimum allowed pass at resonance. It is desired that this ratio be as high as possible. For an effective implementation for quantum applications, this is $100dB$ [23, 46] for a pump input of $1mw$. Additional noise in the signal and idler channels are undesirable as this interferes in coincidence logic apparatus that may be used later down the circuit for characterization of the single photon emitter. Therefore, highly resonant structures are often used.

Two common features of a filter are the linewidth (or FWHM) of the stop band and the extinction ratio. The size of the linewidth is application dependent. For example, narrowline width (of the order of $1nm$) have been desired as this allows for less spectral difference between the signal and idler pairs. This reduces the dispersion effects in the photon sources which limit the

	Year	Type	Reported Extinction (dB)	Bandwidth (nm)	Insertion losses (dB)
R. R. Kumar et al. [57]	2020	CROW	>110 dB	0.5	0.8
D. Oser et al. [58]	2020	BR	>60 dB	-	2
M. Piekarek et al. [46]	2017	MZI	>56dB	1	1.5
J. R. Ong et al. [55]	2013	CROW	>100 dB	1.69	1.4
N. Harris et al. [59]	2014	MRR +BR	>95 dB	1-2	4.5

Table 2.1: Comparison of some methods of on-chip filtering in silicon.

efficiency of pair production by SFWM [51]. However, with some of the proposed methods, creating such devices is difficult do the the stringent fabrication tolerances required. Additionally, the high temperature coefficient of silicon produces random wavelength shifts [52]. This is often corrected by thermal tuning. There have been some proposed applications of wider pump widths. For example, work such as done in [53] suggests engineering pump input for source MRRs utilising SFWM, resulting in wider pump spectrums. Here this is to reduce the requirements of spectral filtering to reduce the spectral correlation (increase the purity) of the produced pairs. High purity is particularly important for quantum applications. Generally, control over the linewidth is a desirable feature of filtering. This can be achieved by thermal tuning, with the drawback of requiring heating elements on chip, increasing the complexity of design and fabrication.

The free spectral range (FSR) of filters is also a factor in design. The FSR is the distance spectrally between resonances in devices that exhibit a comb like transmission spectra. For applications where a filtering scheme is directly used to filter out the signal and idler photons and pass the pump, the FSR required is half that of the ring, such as in [54, 55]. For a scheme where the filter is suppressing the pump, the desirable scheme would have an FSR as wide as possible to reduce the impact on the signal and idler channels. Generally, this is dependent on the scheme used and the fabrication methods.

In the following section, the devices described are all "on-chip". However for experimental work on quantum experiments it is common to to use existing devices developed for telecommunications such as fibre Bragg gratings (FBGS) [56] and wavelength division multiplexers (WDM) [47]. These have been shown to achieve the high extinction necessary yet have high insertion losses and are inherently unscalable due to their size.

2.4.1 Comparison of Methods

Here a range of current devices proposed to address the pump filtering requirements are discussed. First of all, a promising approach is the use of various BR geometries. In brief a BR is a periodic structure which utilises periodic variations in refractive index to create a reflection. Bragg reflectors are used commonly in such applications as fibre Bragg gratings and dielectric mirrors. For application as pump rejection filters on integrated chips, they have been demonstrated to produce promising filtering characteristics, in particular when considering the high extinction ratios achieved. This is done by designing a waveguide with periodic variations in the refractive

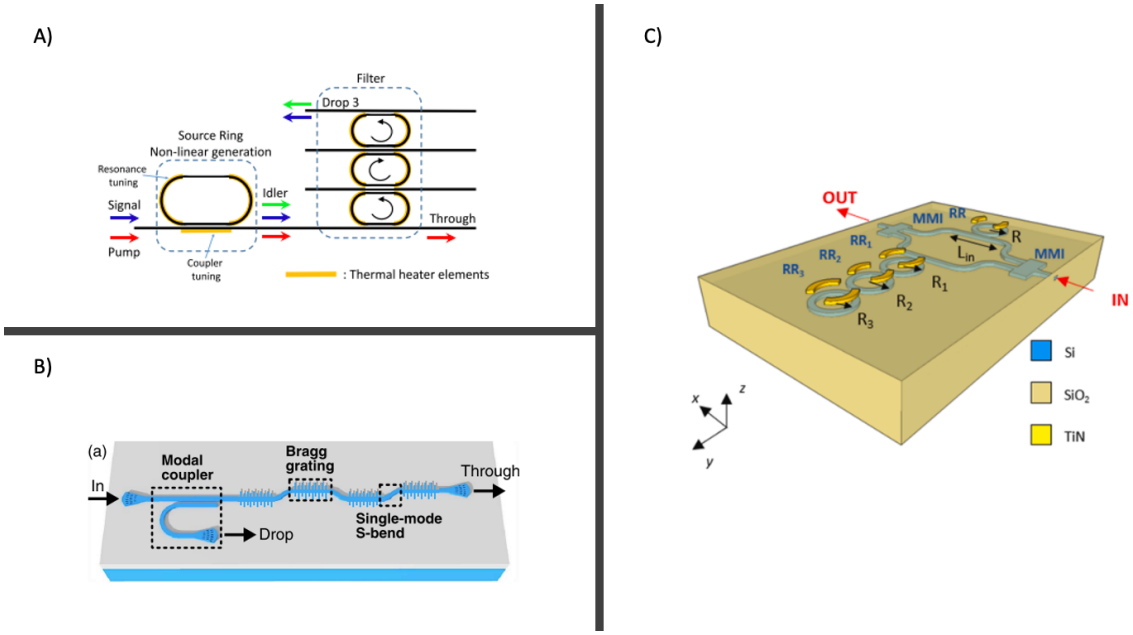

Figure 2.4: Diagrams of some proposed filtering schemes in silicon A) Ring resonater based filtering schemes with cascaded rings. Image taken from [61] B) Bragg grating based pump filtering scheme. Image courtesy of [58] C) MZI filtering scheme with CROW additions. Image taken from [62]

index by altering the dimensions. These dimensions are carefully designed for their application. It has been demonstrated [58] that Bragg grating based geometries in SOI integrated circuits can result in extinctions > $60dB$. It is important to note for all comparisons that alot of demonstrations are limited by the noise floor of the apparatus used to characterise them. Schemes with Bragg reflectors have a few considerations. The first is in size. Some of the high extinction proposed schemes are on the order of high $100nms$ in length, a key limiting factor [51]. Maintaining the phase along such filters is difficult and prone to fabrication issues. This becomes an limiting factor as the size of these filters increases [58]. Promising demonstrations of the attempts to address these issues in SOI include the use of counter-directional coupling in multimode waveguides [60] and dual periodic structures [51].

Other promising filtering applications involve the use of MZIs in the waveguide system. A MZI will produce a resonant structure when the phase difference in the two path lengths is π. This phase difference can be achieved by active tuning using heaters [28, 62]. Additionally, the addition of ring resonators can improve the filtering characteristics [62].These have been shown to produce high extinction ratios [46], achieved through cascading of multiple devices. The resonances are highly reliant on environmental factors further motivating the inclusion of active tuning elements. This, alongside the size of the devices themselves, which often include cascaded MZIs connected up to achieve high extinction, results in a large footprint on the chip.

The final process here discussed, and the focus of this project, is the use of ring resonators.

The theory of such devices is discussed in chapter 2. Ring resonators consist of a waveguide (bus) coupled to another waveguide (ring) which is turned into itself. This results in the formation of an optical cavity and a resulting frequency comb structure in the transmission spectra in the bus waveguide. It is this comb structure which can be utilised for filtering. The smaller the ring the larger the FSR [63]. Rings have the benefit of allowing for some flexibility in the design of the bandwidth. This is achieved by the careful ring design, changing the losses and and coupling coefficients. These structures can be fabricated in a range of different configurations, noticeably in coupled-resonator optical waveguides (CROW) as in [57]. Rings can be fabricated on the microscale in SOI using current nanofabrication techniques such as lithography and dry etching. This results in small scale devices with radii of the order of $10s\mu m$. Various ring based schemes for filtering have shown promising applications in addressing pump filtering. High extinction (100dB) ratios have been demonstrated [55, 57]. This shows the promise of ring based structures. However, for these demonstrations, a large number of rings was required to achieve the high extinction ratios. This results in a in large footprint, comparable to that of the MZI and BR structures discussed. Rings can be fabricated to a very high Q-factor and are often used, as a consequence, as devices for the generation of SWFM photon pairs due the high amounts of electric field that can be present in the ring.

2.5 Waveguides

For the efficient routing of light on a chip, effective waveguides need to be fabricated. A waveguide is a structure that guides electromagnetic waves in a particular direction. They allow for the creation of photonic circuits for a range of applications. The size and shape of these guides determine the wave's propagation and are designed for their specific use. On an SOI, platform waveguides consist of a silicon region surrounded by air or SiO_2 cladding. An example can be seen in figure 2.5. This contrast in material results in high contrast in the refractive indices of the core and cladding ($\sim 40\%$ in the $Si0_2$ case). It is this contrast which confines the waves through total internal reflection. Silicon's relatively high refractive index makes it a desirable material for this application.

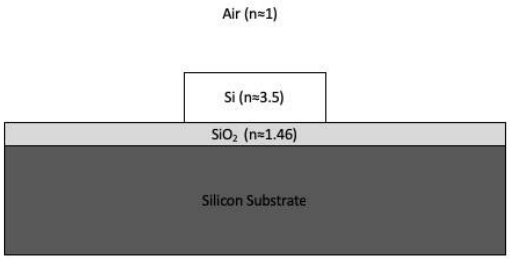

Figure 2.5: Cross section of a rectangular waveguide in SOI.

Waveguides work on the principle of total internal reflection [17, 64]. This principle is illustrated in figure 2.6. Total internal reflection can be described from Snell's law (equation 2.6), occurring when the incidence angle θ_i is greater than the critical angle θ_C.

$$\frac{sin(\theta_i)}{sin(\theta_{r'})} = \frac{n_2}{n_1} \tag{2.6}$$

On the SOI platform, at $1550nm$ wavelengths, the refractive index of silicon is 3.45 compared to 1 for air and 1.48 for SiO_2. This results in the high confinement within the guiding medium. The value of the critical angle θ_c between two materials can be described in terms of their refractive indices,

$$sin(\theta_c) = \frac{n_2}{n_1} \tag{2.7}$$

Figure 2.6 shows the effect of the total internal reflection of a layer of higher refractive index (n_1) between two layers of lower, $n_{2,3}$. It is a 2D representation of a planer waveguide. As the angle of incidence θ_i increases, the refraction in layer 2 decreases until the angle is greater than θ_c and reflection occurs. As long as the same condition is met at layer 3, the light is internally reflected in the waveguides and will continue to propagate within the waveguide, here in the z direction. This propagation, for a vacuum wavelength λ, will have wave vector $\boldsymbol{k_1}$ where the magnitude is $k_1 = \frac{2\pi n_1}{\lambda}$. The propagation constant, β, describes the competent of $\boldsymbol{k_1}$ that travels in the waveguide's propagation direction.

$$\beta = \frac{2\pi n_{eff}}{\lambda} \tag{2.8}$$

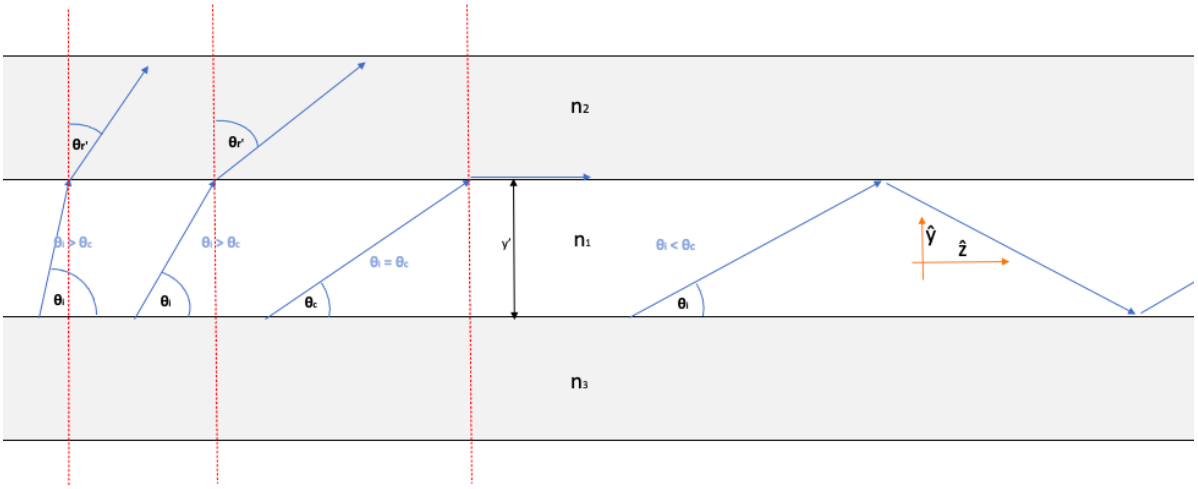

Figure 2.6: Diagram showing the basic geometrical formulation of total internal reflection. As light travels through medium 1 with refractive index n_1 it meets the boundary of medium 2 (n_2). At this boundary it is refracted, travelling off at an angle of refraction $\theta_{r'}$, through medium 2. This angle depends on the angle incident (θ_i) by Snell's law. The angle of refraction decreases as the angle of incidence decreases. Eventually, the angle of refraction is 0. This occurs when the incidence angle equals the "critical angle", θ_c. At incident angles less then θ_c the beam is reflected back into medium 1 and reflection occurs.

Here n_{eff} is the effective refractive index of the waveguide. This is dependent on the specific geometry of the waveguide. The size and geometries of a waveguide determine the allowed modes which can propagate independently along a waveguide [17, 64]. In this case, modes are usually denoted as transverse electric (TE), magnetic (TM) and electromagnetic (TEM) [17]. Transverse here tells us that the propagation of the mode is transverse (in the z-direction of figure 2.6) to the function of the mode. As the wave reflects between the layers interferes with itself, which results in this transverse effect. Therefore a key dependency for the allowed modes is on the phase shift which occurs at the reflection boundary.

The origin of this phase shift is described by the Fresnel equations [17]. For a refection at a boundary between n_1 and n_2 the reflection coefficient r is described as

$$r_{TE} = \frac{n_1 cos(\theta_i) - n_2 cos(\theta_{r'})}{n_1 cos(\theta_i) + n_2 cos(\theta_{r'})} \tag{2.9a}$$

$$r_{TM} = \frac{n_2 cos(\theta_i) - n_1 cos(\theta_{r'})}{n_2 cos(\theta_i) + n_1 cos(\theta_{r'})} \tag{2.9b}$$

and the transmission equal to $1-t$. The value r linearly relates the incident field to the reflected field. Therefore, t relates the incident field to the transmitted field. When $|t| = 0$ then

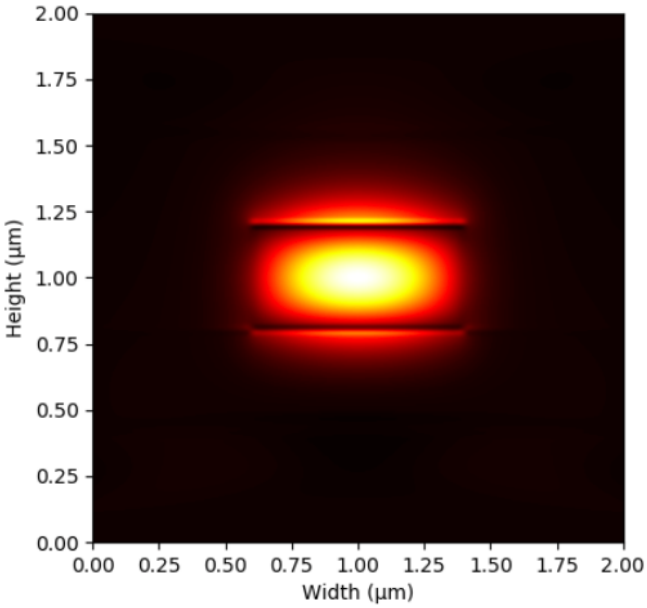

Figure 2.7: Simulation of the TE mode of a SOI waveguide of the type shown in figure 2.5. This image was produced using FDTD simulation software MEEP [65]

$|r| = 1$. The r is complex, which results in a phase shift described by [17, 66].

(2.10a) $$\phi_{TE} = 2tan^{-1}\left[\sqrt{\frac{sin(\theta_i)^2 - \frac{n_2^2}{n_1^2}}{cos(\theta_i)}}\right]$$

(2.10b) $$\phi_{TM} = 2tan^{-1}\left[\sqrt{\frac{\frac{n_1^2}{n_2^2}sin(\theta_i)^2 - 1}{\frac{n_2}{n_1}cos(\theta_i)}}\right]$$

For the guiding layer in the planar waveguide shown in figure 2.6, the light gains a phase shift of,

(2.11) $$\phi_m = k_1 n_1 y' sin(\theta_i)$$

at the boundary of two materials n_1 and n_m, and a guiding layer thickness y'.

In order for a mode of propagation to be allowed, the conditions have to allow for constructive interference, for our example

(2.12) $$2p\pi = 2k_1 n_1 y' sin(\theta_i) - \phi_2 - \phi_3$$

where p is an integer. This integer indicates the mode number. Here the effective refractive index can be defined as the effective propagation of the mode in a waveguide, for our example,

$$n_{eff} = n_1 sin(\theta_i) = n_2 cos(\theta_{r'}) \tag{2.13}$$

if we assume TE polarisation and $n_2 = n_3$, equation 2.12 can be rearranged to

$$tan^{-1}\left[\frac{kn_1 ycos(\theta_i) - p\pi}{2}\right] = \frac{\sqrt{sin^2(\theta_i) - (n_1/n_2)^2}}{cos(\theta_i)} \tag{2.14}$$

This equation allows us to determine the incidence angle θ_i for values of n_1, n_2, k, and for the mode number p. This in turn allows for the calculation of the effective refractive index n_{eff}. In order to expand this analysis to a two-dimensional rectangular waveguide, as used for this project, the waveguide can be considered as one planar waveguide and then a second, perpendicular one. This is shown in figure 2.8. For the SOI waveguide setup used in this project, the effective index can be deduced by first solving for the planar waveguide bounded by air $n_2 = 1$ giving a value for $n_{eff,1}$. Then the waveguide refractive index n_{eff} can be solved using equation 2.14 where $n_2 = 1$ and $n_3 = n_{eff,1}$. This method of analysis is known as the effective index method.

Waveguide dimensions can be designed for various purposes within integrated photonics. A single moded waveguide, as shown in figure 2.7, is desirable as it limits modal dispersion [17, 24]. They are also smaller therefore more scaleable. A multimoded waveguide is useful as a optical device such as a beam splitters [67, 68]. Additionally, they have larger critical dimensions, which makes fabrication simpler.

2.5.1 Waveguides from Maxwell's Eqautions

With the previous geometric picture laid out, it is useful to provide an analysis using Maxwell's equations for the waveguides. Maxwell's equations are the equations which describe the classical properties of electromagnetic phenomena. They were published by James Clark Maxwell in 1873. They describe electromagnetic waves and therefore, waveguides. The following analysis is taken from Reed [17]. Assuming an isotropic, linear, dielectric and lossless medium for simplicity, we can write the Maxwell curl relations as

$$\nabla \times \mathbf{E} = -\frac{\partial \mathbf{B}}{\partial t} \tag{2.15}$$

$$\nabla \times \mathbf{H} = \mathbf{J} + \frac{\partial \mathbf{D}}{\partial t} \tag{2.16}$$

The vectors **E**, **H**, **D**, **B** and **J** are the values of the electric field, magnetic field, electric field flux density, magnetic field flux density and the charge density, respectively. With our assumptions, **D** and **B** are related to the electric and magnetic fields as,

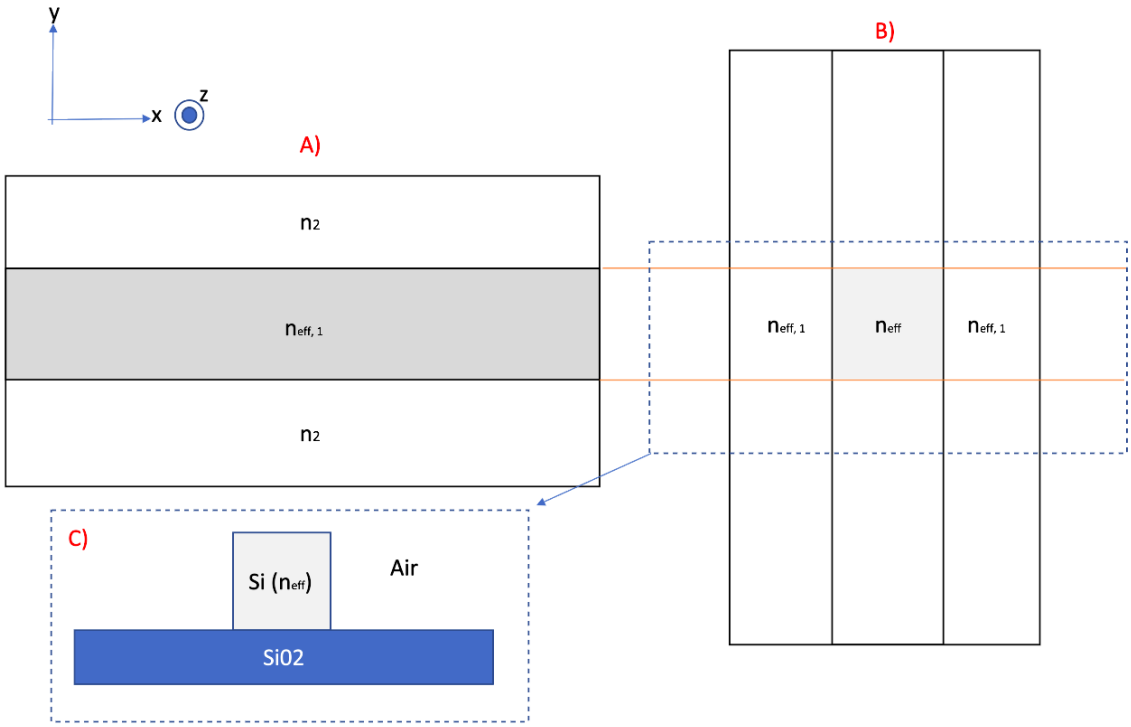

Figure 2.8: Simple diagram detailing the formation of the effective index of a rectangular waveguide. A) The effective index ($n_{eff,1}$) of a slab waveguide can be determined taking into account the indices of the outer cladding slabs (n_2). B) This can be repeated using the new effective index perpendicular to that in A to find the index of the rectangular waveguide. C) The result of this method.

(2.17) $$\mathbf{B} = \mu\mathbf{H}$$

(2.18) $$\mathbf{D} = \varepsilon\mathbf{E}$$

Where μ anf ε are the permeability and the permittivity of the medium, respectively so that,

(2.19) $$\mu = \mu_0\mu_r$$

(2.20) $$\varepsilon = \varepsilon_0\varepsilon_r$$

The constants here μ_r and ε_r are the relative permeability and permitivity of the material in question. The fundamental constants μ_0 and ε_0 are the permitivity and permeability of free space where the speed of light in a vacuum is,

$$c = \frac{1}{\sqrt{\varepsilon_0 \mu_0}} \tag{2.21}$$

and the speed in the medium,

$$v_m = \frac{1}{\sqrt{\varepsilon \mu}} \tag{2.22}$$

The current density can be expressed in terms of the electric field as.

$$\mathbf{J} = \sigma \mathbf{E} \tag{2.23}$$

where σ is the conductivity. From these equations, the wave equation for electromagnetic waves can be deduced.

$$\nabla^2 \mathbf{E} = \varepsilon \mu \frac{\partial^2 \mathbf{E}}{\partial t^2} \tag{2.24}$$

$$\nabla^2 \mathbf{B} = \varepsilon \mu \frac{\partial^2 \mathbf{B}}{\partial t^2} \tag{2.25}$$

In order to describe a guided wave, boundary conditions need to be applied. Here it is again assumed a 2d planar waveguide, infinite in the z-direction and constricted in the y (figure 2.6). Focusing on the electric field, in the transversely polarised conditions of a waveguide with TE modes, the electric field only propagates in the z-direction. Therefore the wave equation in the E_y component can be written as,

$$\frac{\partial^2 E_x}{\partial y^2} + \frac{\partial^2 E_x}{\partial z^2} = v_m \frac{d^2 E_x}{\partial t^2} \tag{2.26}$$

With plane wave solutions,

$$E_x = E_x(y) e^{(i\beta z)} e^{(-i\omega t)} \tag{2.27}$$

These solutions are sinusoidal in time with angular frequency ω and propagate with propagation constant β. Differentiating and substituting, it can be shown [17] that the wave equation can be written in the following form.

$$\frac{\partial^2 E_x}{\partial y^2} = [\beta^2 - k_0^2 n^2(y)] E_x \tag{2.28}$$

In these equations, β is the propagation constant, k_0 is the vacuum wavenumber and n is the refractive index.

Fully analytical solutions for rectangular waveguides in 3 dimensions is an impossible task [69]. Modes propagating in the z direction are solutions to the following analogous equations

$$\frac{\partial^2 E_z}{\partial y^2} + \frac{\partial^2 E_z}{\partial x^2} = [\beta^2 - k_0^2 n^2(x,y)]E_y \tag{2.29}$$

$$\frac{\partial^2 H_z}{\partial y^2} + \frac{\partial^2 H_z}{\partial x^2} = [\beta^2 - k_0^2 n^2(x,y)]H_y \tag{2.30}$$

Approximate methods of analysis which make assumptions include the Marcatilii method [70], the Kumar method [71], and the effective refractive index method. There are numerical methods, some packaged in professional software such as FIRMMWARE and Lumerical. It is the latter which is used for the majority of the analysis in this project.

2.5.2 Loss Factors in Waveguides

The analysis so far has assumed the use of a lossless medium. This assumption, however, is not the case in practice, and there are always inherent losses in photonic systems. In this section, loss factors in SOI waveguides will be briefly discussed. These include absorption processes in silicon as well as scattering due to interfaces and the material properties. Finally, radiation in bends will be discussed.

2.5.2.1 Absorption

There are two main sources of absorption losses in semiconductor waveguides, interband and free carrier absorption [17, 24]. Interband absorption is a phenomenon that occurs when photons with sufficient energy are absorbed when they excite electrons in the valance band of the semiconductor into the conduction band. This process can be seen in figure 2.9.

This is an effective key limiter on the usable wavelengths of such materials. This effect is significant for wavelengths which are less than the infrared. It is less prominent at common communication wavelengths $\approx 1.5\mu m$. Free carrier absorption is also to be considered in semiconductors. It refers to the absorption of a photon by electrons present in the conduction band. This absorption promotes said electron into a higher unoccupied energy state. This process is described in figure 2.10.

Free carrier absorption requires less energy comparatively then Interband absorption as there is no band gap to breach. As a consequence, the effects are observed at higher wavelengths [17, 72] and should be considered thusly.

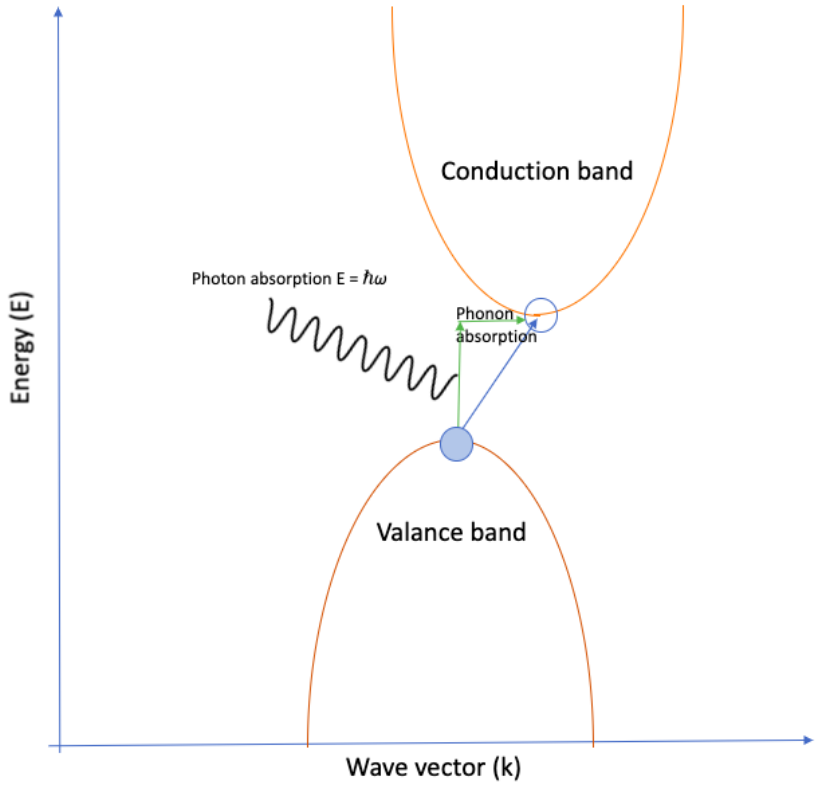

Figure 2.9: Simple diagram of the process of interband absorption. An incident photon excites an electron in the valence band up to the conduction band and is subsequently absorbed. As this transition is also in momentum, a phonon is also required.

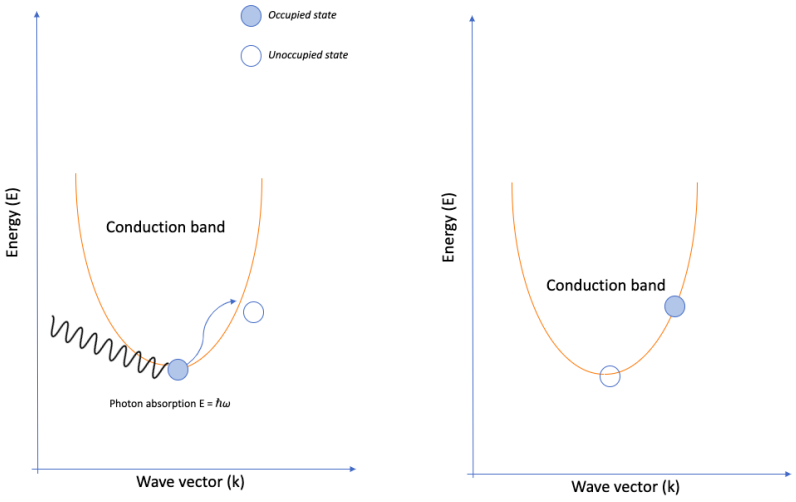

Figure 2.10: Simple diagram of free carrier absorption. Here electrons are promoted up from a lower energy state in the conduction band into a higher unoccupied state with the aid of a phonon.

2.5.2.2 Scattering

Volume scattering in waveguides results from defects in the material such as gaps, contaminant atoms and defects in the lattice. Scattering also occurs due to features of the interfaces such as surface roughness of a waveguide. These effects are the result of the fabrication. Surface roughness can be reduced by improved fabrication techniques, particularly in the etching stage. Different etching recipes can have significant implications on the final surface roughness. This surface roughness is especially problematic for devices with smaller critical dimensions. Careful characterisation of waveguides must be done. This can be achieved via processes such as the cutback method [17]. This allows for the material to be characterised along with other factors. Coupling losses from devices such as grating couplers can be substantial.

2.5.2.3 Radiation

Radiation losses are also present in waveguides. This refers to leakage out of modes that are defined by the theory laid out above. This can be useful as it underpins devices such as the directional coupler and SNSPDs as has been discussed. This leakage can be seen in figure 2.7. Reducing these losses can be done by increasing the waveguide size, although in practise this can be impractical as it can result in scaling issues.

2.5.2.4 Bends

Bends in waveguides are required for a tightly packed chip. Tighter packing results in higher component density and scalability. However, bends have intrinsic losses. This arises from the fact that as the bend turns, the incidence angle changes in the waveguide. This means that there is unavoidable refractive leakage out of the waveguide. This results in losses out into the cladding. These losses are higher for tighter bends, so the first way of reducing this effect is by increasing the bend radius. All this has the effect of pushing the mode profile out towards the outer side as can be seen in figure 2.11. Silicon is relatively less effected by bending losses due to its high refractive index contrast.

2.6 Ring Resonators for On-Chip Filtering

For this work, a detailed understanding of the parameters of ring resonators are required. A ring resonator is a type of optical cavity. They consist of two or three waveguides, one in a ring shape, bending round back into itself, creating a cavity. The others are straight, coupled into or out off the ring. Interference between the straight waveguide which carries the input ("Bus waveguide") and the ring waveguide results in comb-like transmission spectra. It is this spectra that can be used for filtering applications. The following sections outline the theory of ring resonators, starting with directional couplers, carrying on to simple rings systems and finishing with the

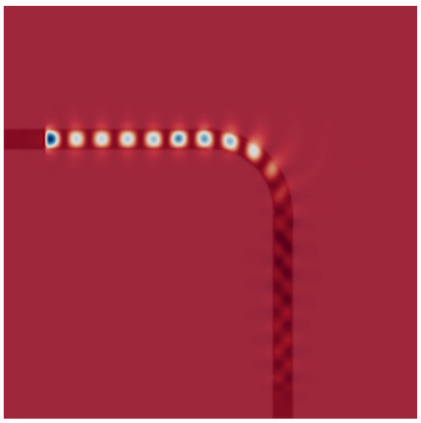

Figure 2.11: FDTD simulation of a tight waveguide bend. The bend here is of radius $3\mu m$. The power is seen to leak out as the waveguide turns. Waveguide here is Silicon with width $500nm$ and height $220nm$. The cladding is air. This was simulation was produced using MEEP [65]

behaviour of these systems with the addition of absorptive nanowires. All resonators here will be in the "Single Bus" or "All-Pass" configuration, with directional couplers. These consist of a single straight waveguide and a ring waveguide (figure 2.15).

2.6.1 Directional Couplers and Coupled Mode Theory

A basic component for integrated photonic devices, and in particular for ring resonators, is the directional coupler [68]. In simple terms, a directional coupler is a device for transferring light from one waveguide to another. This is a key part in the operation of a ring resonator and is a common way of splitting light in integrated photonics. It should be noted, there are also examples of using other beam splitting methods such as Multi-Mode Interferance devices [68, 73], but this is not applicable to this work. Directional couplers consist of two waveguides in close proximity, as shown in figure 2.12.

Here, an explanation of the coupled mode theory as relevant for a directional coupler will be laid out. This theory is taken from a range of sources, in particular Hunsperger [74], Rabus [68] and Haung [75]. Assume a mode in a single waveguide as shown in figure 2.12. Its electric field can be described as,

$$\mathbf{E}(x,y,z) = A(z)\tilde{\mathbf{E}}(x,y) \tag{2.31}$$

where $A(z)$ is the complex amplitude and $\tilde{\mathbf{E}}(x,y)$ is the solution for the normalised field distribution of the mode in one waveguide, taking into account the boundary conditions. The

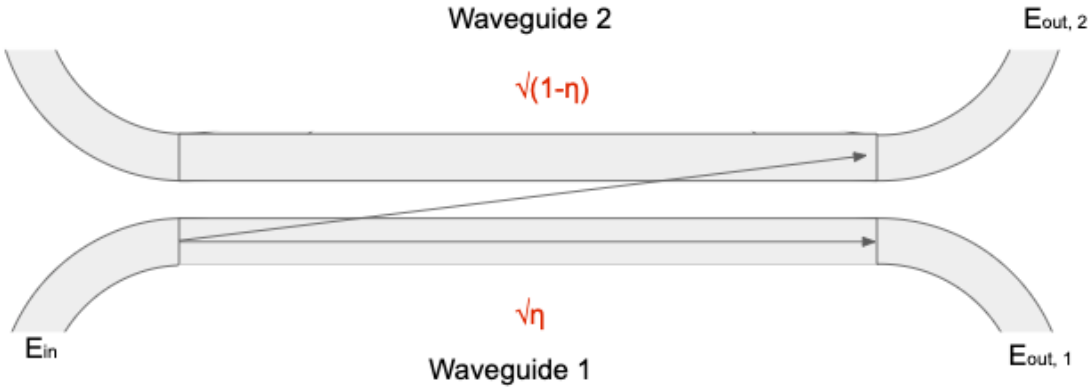

Figure 2.12: Diagram of directional coupler. The reflection and transmission here are shown as $\sqrt{1-\eta} = r$ and $\sqrt{\eta} = t$.

power at a point z in the waveguide is therefore equal to the modulus squared of this amplitude,

$$P(z) = A(z)A^*(z) = |A(z)|^2 \tag{2.32}$$

If a second waveguide is introduced as seen in figure 2.12, coupled mode equations can be introduced showing the variation of the respective amplitudes in the respective waveguides.

$$\frac{dA_1}{dz} = -i\beta_1 A_1(z) + \kappa_{12} A_2(z) \tag{2.33}$$

Likewise,

$$\frac{dA_2}{dz} = -i\beta_2 A_2(z) + \kappa_{21} A_1(z) \tag{2.34}$$

is the case in the second waveguide. Here $\beta_{1,2}$ are the propagation constants of the modes and $\kappa_{12,21}$ are the coupling coefficients. Here we will assume the waveguides are identical and thus the coupling coefficient between then is the same ($\kappa_{12} = \kappa_{21} = -i\kappa$) and the propagation constant is the same ($\beta_1 = \beta_2 = \beta$). Considering boundary conditions as shown in figure 2.13, solutions of these equations are,

$$A_1(z) = cos(\kappa z)e^{-i\beta z} \tag{2.35}$$

$$A_2(z) = -isin(\kappa z)e^{-i\beta z} \tag{2.36}$$

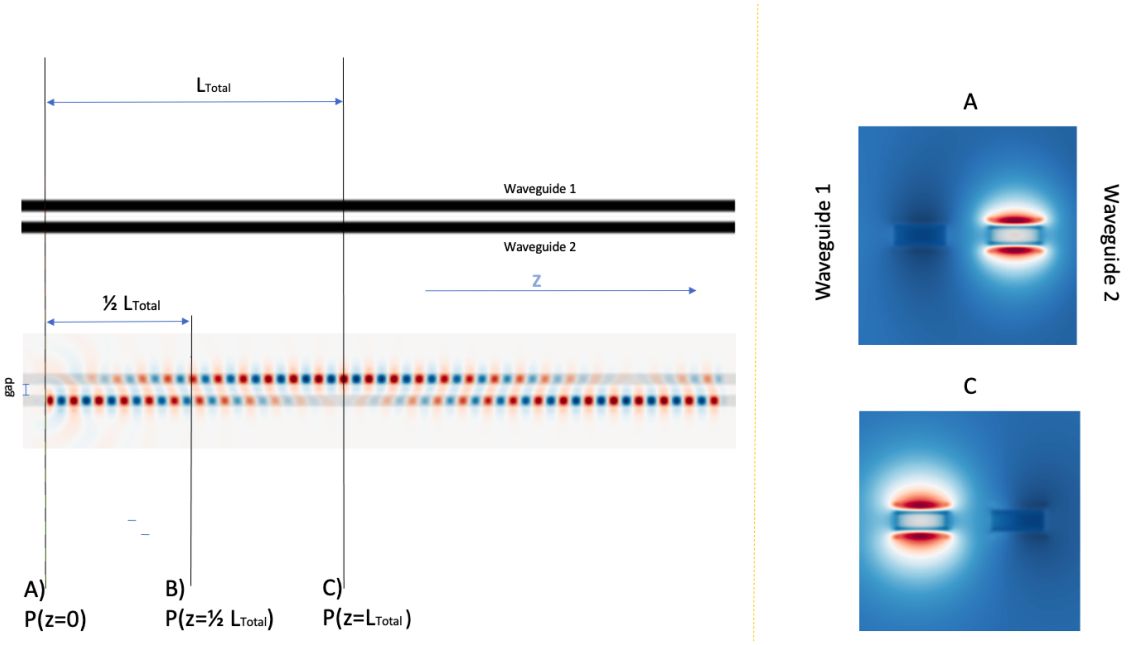

Figure 2.13: Simulation of a directional coupler with silicon waveguides. The E Field can be seen in the bottom left with the TE mode profiles can be seen on the right. at the point A the power is confined to waveguide 2. At B the power is confined in equal amounts in both. At C, after the length L_{Total}, the power is transmitted 100% into waveguide 1.

Assuming an exponential loss coefficient in the waveguide,

$$\beta = Re\{\beta\} - \frac{\alpha}{2}i \tag{2.37}$$

Therefore power can be shown as

$$P_1(z) = cos^2(\kappa z)e^{-\alpha z} \tag{2.38}$$

$$P_2(z) = sin^2(\kappa z)e^{-\alpha z} \tag{2.39}$$

Giving rise to the transmission and reflection. The value of κ is dependent on the modal overlap of one waveguide to another. For a well confined mode, as assumed for this project, it can be shown as equal to,

$$\kappa = \frac{\pi}{2L_{Total}} \propto exp(-C/\xi) \tag{2.40}$$

Where L_{Total} is the length for a given geometry where power transmission from one waveguide to another is 100%, the distance C is the distance between the waveguides and ξ is the decay

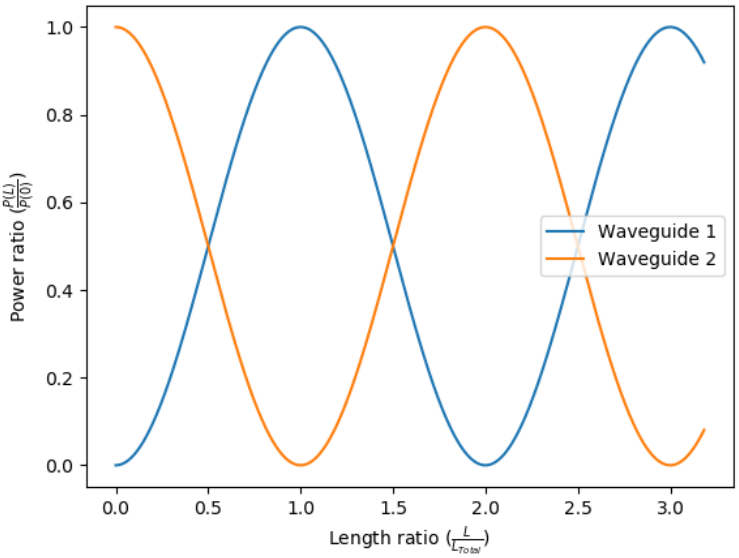

Figure 2.14: A graph showing the variation of power along a directional coupler as described in figures 2.12 and 2.13. Here the plot shows ratio of the power at a point $z = L$ along the length of a directional to the power at $z = 0$, $\left(\frac{P(L)}{P(0)}\right)$. The loss coefficient is ignored ($\alpha = 0$). This is plotted against the ratio of the length L over the total length L_{Total}, $\left(\frac{L}{L_{Total}}\right)$.

factor outside the waveguides. The value of κ can be analysed by a range of methods including the Marcatili [70] and Kumar [71] methods. In figure 2.12 the resulting coupling coefficients are visible. For lossless waveguides, a reasonable assumption for this project,

$$\eta = cos^2(\kappa L_{dc}) \tag{2.41a}$$

$$1 - \eta = sin^2(\kappa L_{dc}) \tag{2.41b}$$

Here $\sqrt{\eta}$ is the $reflection$ with η as the $reflectivity$. Similarly, $\sqrt{1-\eta}$ is the $transmission$ with $1-\eta$ as the $transmitivity$.

From equations 2.40 and 2.41b the key features for a certain splitting ratio in set mediums are the gap between the waveguides, C, and the length of the coupler itself L_{dc}. These become key design parameters for fabricating effective filters with ring resonators.

2.6.2 Ring Resonators

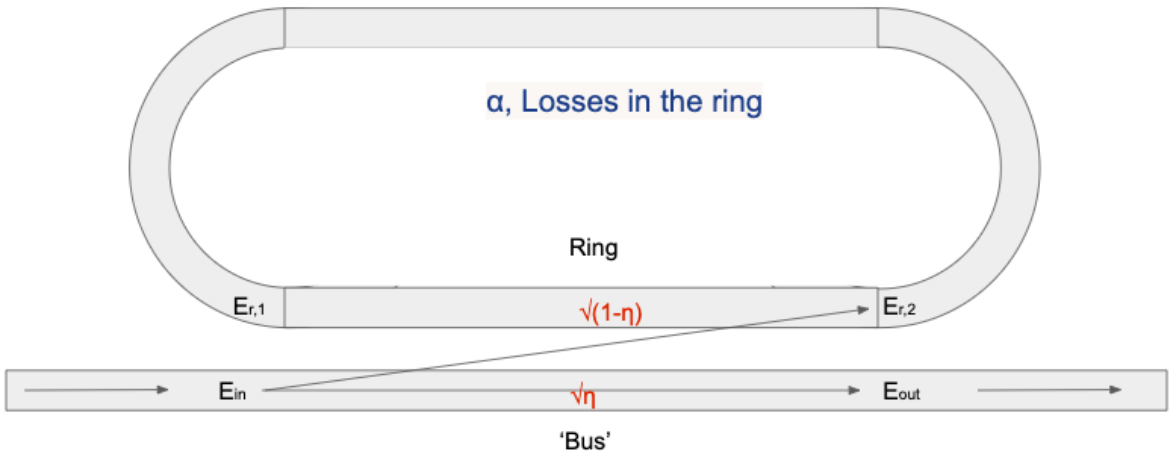

Figure 2.15: A diagram of a ring resonator. The value α represents the losses present in the ring. The relations of the reflection and transmission to the electric field intensity in the ring can be seen.

Ring resonators are a cavity that can be used in various applications in silicon photonics [23, 63, 68]. These include modulators [68], single-photon generation [44], as well as filters which is the topic of this work. The basic setup is shown in figure 2.15. This shows an $All-Pass$ resonator with an input Bus waveguide and another waveguide in a ring configuration. When an integer multiple of the length of the ring L_{ring} is equal to the wavelength divided by the effective refractive index, λ/n_{eff}, then constructive interference occurs in the ring. The wavelength at this occasion is the resonant wavelength, λ_{res}. The following analysis will follow the "field-matching method" as described by many authors [63, 68, 76]. The electric field at the points in the ring, E_{in},E_{out},$E_{r,1}$ (into the directional coupler from the ring) and $E_{r,2}$ (out of the directional coupler in the ring) are related by the coefficients of the directional coupler and the round trip transmission in the ring α. Contributions to α include propagation losses in the waveguide (see section 2.5) as well as bending losses. The electric field is coupled into the ring from the bus through the coupler with behaviour as described in the previous section. As the portion of the field propagates around the ring, a phase θ is produced where,

$$\theta = \frac{2\pi L_{ring} n_{eff}}{\lambda} \tag{2.42}$$

This allows for the description of $E_{r,1}$ in relation to $E_{r,2}$,

$$E_{r,1} = \alpha e^{i\theta} E_{r,2} \tag{2.43}$$

The use of the coupler allows for the relation of the fields E_{in},E_{out},$E_{r,1}$ and $E_{r,2}$ by the following transfer matrix.

$$\begin{pmatrix} E_{out} \\ E_{r,2} \end{pmatrix} = \begin{pmatrix} \sqrt{\eta} & i\sqrt{1-\eta} \\ i\sqrt{1-\eta} & \sqrt{\eta} \end{pmatrix} \begin{pmatrix} E_{in} \\ E_{r,1} \end{pmatrix} \tag{2.44}$$

This, along with equation 2.43, allows for,

$$E_{out} = \sqrt{\eta} E_{in} + i\sqrt{1-\eta} E_{r,1} \tag{2.45a}$$

$$E_{r,2} = i\sqrt{1-\eta} E_{in} + \sqrt{\eta} E_{r,1} \tag{2.45b}$$

$$E_{out} = \frac{\sqrt{\eta} - \alpha e^{i\theta}}{1 - \sqrt{\eta}\alpha e^{i\theta}} E_{in} \tag{2.45c}$$

which describes the input and output fields for the bus waveguides. The transmitted power is proportional to the squared electric field intensity. This means the ratio of the power inputted P_{in} and the power outputted P_{out} from the bus is

$$\frac{P_{in}}{P_{out}} = \left[\frac{E_{in}}{E_{out}}\right]^2 = \frac{\alpha^2 + \eta - 2\alpha\sqrt{\eta}cos(\theta)}{1 + (\alpha\sqrt{\eta})^2 - 2\alpha\sqrt{\eta}cos(\theta)} \tag{2.46}$$

As stated, this relationship is dependent on the coupling and the losses of the waveguide. There are three regimes of coupling.

$$\sqrt{\eta} < \alpha \;\; under\, coupling \tag{2.47a}$$

$$\sqrt{\eta} > \alpha \;\; over\, coupling \tag{2.47b}$$

$$\sqrt{\eta} = \alpha \;\; critical\, coupling \tag{2.47c}$$

Under coupling occurs when the reflection is less than the loss in the ring, over coupling when the reflection is greater than the losses and critical coupling when they are equal. For filtering, the critical coupling is desired as it results in the most amount of extinction.

Figure 2.17 shows the P_{out}/P_{in} ratios for a typical ring resonator as a function of wavelength. From this typical spectra, various features of ring resonators can be seen. There are a number of dips in the transmission where the resonance wavelengths can be observed. The depth of this dip shows extinction. The distance between these dips is the FSR as the wavelengths between them are free to pass through the resonator. This can be seen in figure 2.17. These free to pass

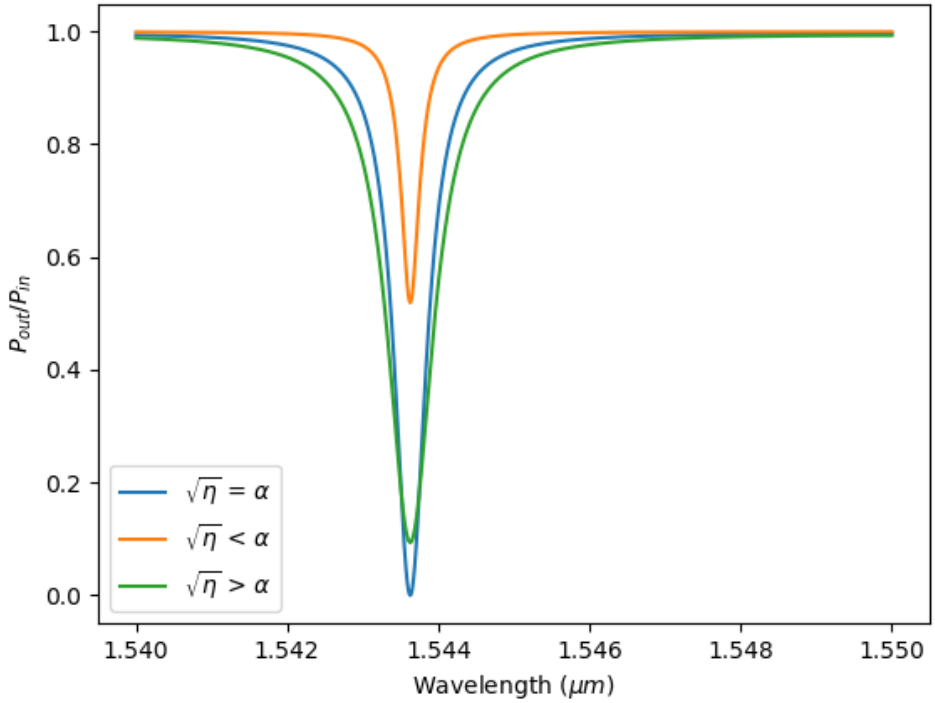

Figure 2.16: Graph showing calculations of the transmission spectra of the three coupling regimes. Here the transmission $\sqrt{\eta}$ is fixed at 0.95. The spectra are shown for the three regimes of over coupling, under coupling and critical coupling. The over coupled curve (green) shows a wider linewidth less a reduced extinction. The under coupled curve (orange) shows a greatly reduced extinction and linewidth. Critical coupled curve (blue) shows the maximum amount of extinction.

wavelengths make up the Passband. The FSR is dependent on the length of the ring, L_{ring}, and the group index, n_g.

$$FSR = \frac{\lambda_{res}^2}{n_g L_{ring}} \tag{2.48}$$

The shape of the resonance details the linewidth of the filter and can be described by the FWHM of the dip. The FWHM can be described as

$$FWHM = \frac{(1-\sqrt{\eta}\alpha)\lambda_{res}^2}{\pi n_g L_{ring}\sqrt{\sqrt{\eta}\alpha}} \tag{2.49}$$

With these describers defined, the Finesse and the Q-factor of the filter can be deduced. The finesse F describes the sharpness of the dip in relation to the FSR. The Q-factor describes the, amount of energy in the ring and by its dependence on the FWHM, sharpness of the peak with

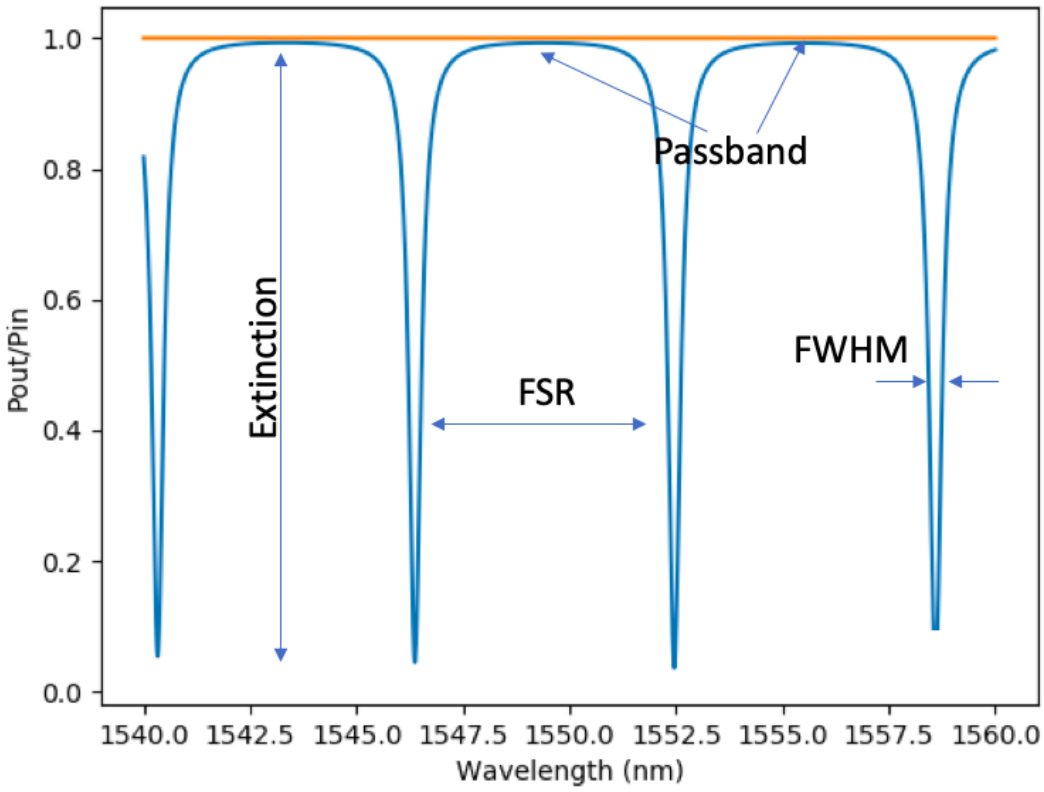

Figure 2.17: A typical transmission plot showing FWHM, FSR and extinction.

respect to the central resonance wavelength. In a resonator, such as the rings here, the Q-factor works as a measure of the losses. A lower Q-factor indicates a ring with higher losses. The Finesse and the Q-factor are defined in terms of the FWHM as follows,

$$F = \frac{FSR}{FWHM} \tag{2.50}$$

$$Q = \frac{\lambda_{res}}{FWHM} \tag{2.51}$$

2.6.3 Nanowires For Absorption

Deposition of nanowires has been shown to have a range of applications in silicon photonics [37]. These include superconducting nanowire single-photon detectors (SNSPDs) [23, 37]. Furthermore, it has been suggested that absorptive nanowire deposition can be used to improve on-chip filtering for quantum experiment circuits [66].

The wire itself has a few possible benefits. Control over the stopband linewidth is desirable, here achieved by varying the losses in the ring. This could open up the use of rings to wider

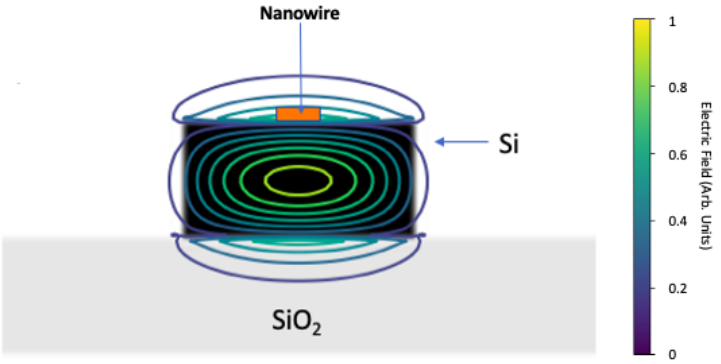

Figure 2.18: Diagram of a waveguide with a nanowire deposited on top, indicated by the arrow. The TE_0 is shown in the contours for a unloaded waveguide. The overlap of the mode with the wire can be clearly shown

linewidth if required, whilst maintaining high extinction. Relatively wider linewidths have some proposed applications for increasing photon purity as discussed in section 2.4. This control could come as a consequence of post-process deposition of the nanowire. If high extinction can be demonstrated by the post processing of under-coupled rings to achieve critical coupling, but with lower Q-factors, this may be of benefit to such applications. Spectrally, wider passbands and stopbands and the steep gradients between them reduce the need for high fabrication tolerances and tuning [46]. Achieving these characteristics passively has all the benefits that come without using heating elements. Additionally, an absorptive nanowire on the filter reduces the electric field within the ring, thus naturally reducing the generation of unwanted pairs within the filters, which produce unwanted counts in single photon statistics measurements.

2.6.3.1 Beer-Lambert Law

The absorptive properties of nanowires can be understood by the Beer-Lambert Law [17]. The Beer-Lambert Law for solids describes the absorption in bulk solids.

$$I = I_0 exp(-aL) \tag{2.52}$$

Equation 2.52 shows the relation of a signal intensity I as it is absorbed by a material absorption per unit length, a, over a distance L.

The value of the attenuation coefficient a is reliant on the geometry of the nanowire and its material. Specifically, a is related to the refractive index of the material.

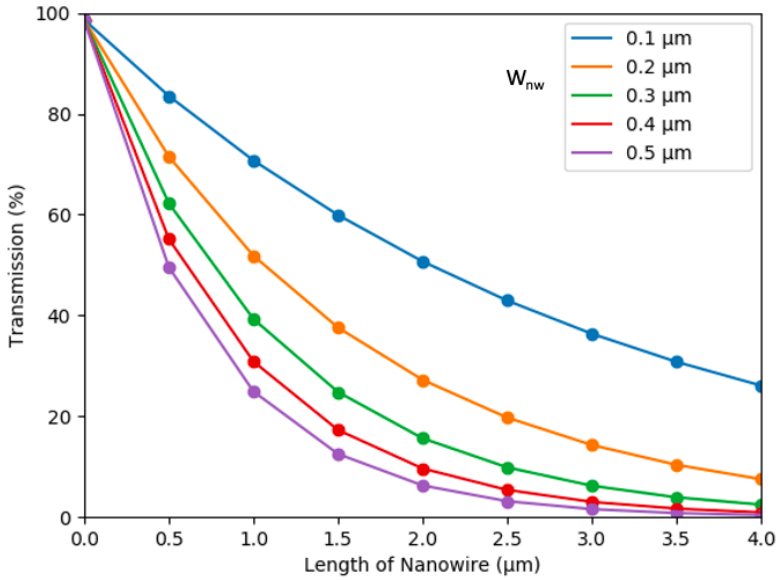

Figure 2.19: Simulation if Beer-Lambert Law behaviour of an absorptive nanowire of Cr atop a silicon waveguide. The nanowire has varying width W_{nw} and the waveguide has width $0.5\mu m$ and $5nm$ height. Simulations were done using FDTD with Lumerical MODE software.

Material	n	κ
Cr [25]	4.13	5.03
NbN	5.23	5.82
Ti	4.04	3.82
Ni	3.38	6.82
MoSi [77]	5.25	4.77

Table 2.2: Refractive index of materials at $1550nm$

2.6.4 Modified Ring Resonators For Filtering

For this work, the addition of a nanowire atop the ring in a resonator must be considered, as described in figure 2.20. This modification changes the absorptive properties of the proportion of the ring with the nanowire. This, in turn, modifies the losses in the ring, represented by α and the phase accumulated though the ring, θ. The losses can be shown as,

$$\alpha = 10^{-\frac{a_{Si}L_{ring}+a_{nw}L_{nw}}{20}} \tag{2.53}$$

and the phase as,

$$\theta = \frac{2\pi(n_{eff}(L_{ring}-L_{nw})+n_{eff,nw}L_{nw})}{\lambda} \tag{2.54}$$

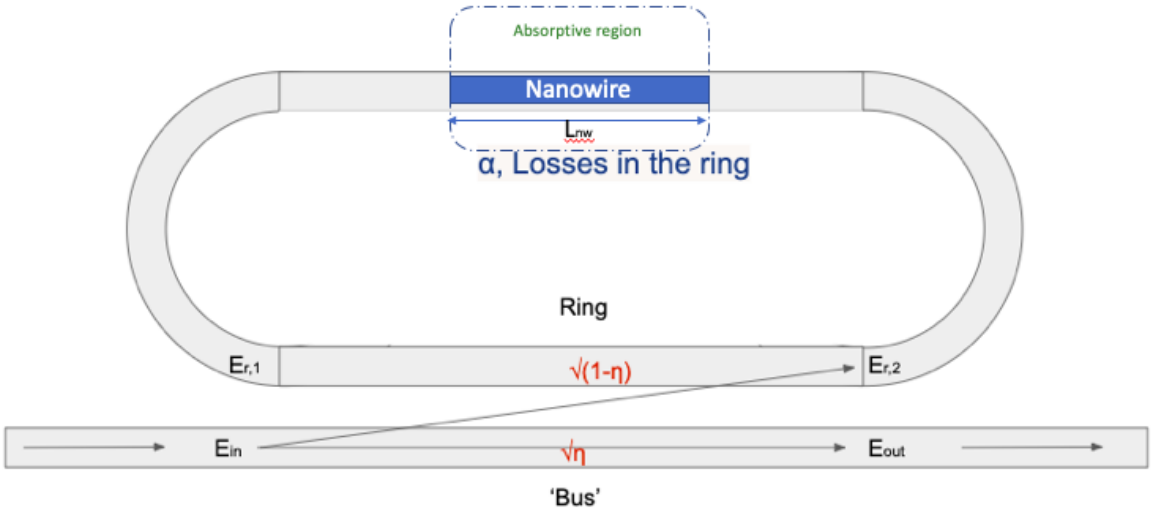

Figure 2.20: Diagram of resonator now including nanowire. This nanowire reduces the round trip transmission α, resulting in an increased FWHM.

Here L_{ring} and L_{nw} are the lengths of the ring and of the nanowire region respectively. This is shown in figure 2.20. The variables a_{si} and a_{nw} are the absorption per unit length in silicon and the nanowire medium respectively, (in dBm^{-1}). The effective indices n_{eff} and $n_{eff,nw}$ are the effective indices in the undeposited and deposited regions, respectively. This allows for the losses in the ring to be tuned. Consequently, this allows for the FSR, FWHM and therefore, the Finesse and the Q-factors to be tuned. Therefore, by implementing deposition as a post-process, desired filtering characteristics can be achieved. For filtering applications, these include suppression at pump wavelengths as well as high extinction levels. The presence of the nanowire can also absorb photon pairs generated in the ring by SFWM, reducing noise in the rest of the system.

2.6.5 Multiple Cascaded Rings

In order for the high extinction ratios required for quantum information applications to be achieved, a multiple ring approach can be considered. This multiple ring configuration can be seen in figure 2.21.

The power ratios can be described in this cascaded configuration in equation 2.55 analogous to equation 2.46

$$\frac{P_{in}}{P_{out}} = \left[\frac{E_{in}}{E_{out}}\right]^2 = \left[\frac{\alpha - \sqrt{\eta}}{1 + (\alpha\sqrt{\eta})}\right]^{2N} \tag{2.55}$$

where N is the number of rings and the values of α and $\sqrt{\eta}$ are as described above.

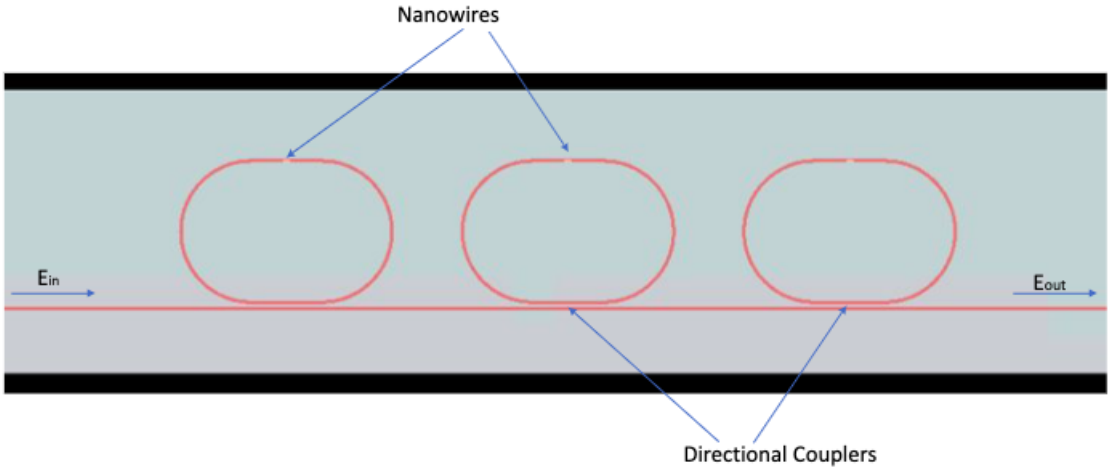

Figure 2.21: Image showing the layout of an example multiple ring system. The locations of the rings, nanowire and directional couplers can be seen. This image is taken from a Lumerical simulation.

2.6.6 Considerations With The Approach

2.6.6.1 Backscatter

The configuration with the nanowire alters the refractive index profile of the waveguide system. This results in a changing of the effective index. Therefore, backscatter in the system is a key consideration [78]. As light propagates into the absorptive region, there is an inevitable reflection in the waveguide. There could be a major contribution reflection from the boundary from an unloaded waveguide without nanowire to a loaded waveguide with nanowire. The reflectance due to this absorption region can be described by,

$$R = \left| \frac{n_{eff} - n_{eff,nw}}{n_{eff} + n_{eff,nw}} \right|^2 \tag{2.56}$$

where n_{eff} and $n_{eff,nw}$ are the effective refractive indices of the waveguide region and the region of the waveguide loaded with nanowire, respectively. All this results in the excitation of modes in the opposite direction to the counterclockwise described by the theory laid out in the previous sections. A good model of this is laid out by Matres and Sorhin [78].The experimental result of this, combined with imperfection in the ring itself, is visible splitting in the resonance.

The reflectance is therefore dependent on the geometry of the nanowire as deposited. It is also dependent on wavelength, meaning that the effect will be different for different resonant peaks across the spectrum.

2.6.6.2 Passband Losses

A drawback with the absorption approach is the loss in the passband of the ring with a lower Q-factor. This effect can be seen in figure 2.16. The transmission spectra show the losses of wavelengths that do not couple into the ring. As Q-factor decreases and the absorptive material is applied, the losses in the ring increase. This is a key consideration and is analysed in the simulations in chapter 4.

CHAPTER 3

METHODS

In this section, the methods of analysis used in this project to investigate the micro-ring filtering system will be discussed. This discussion will focus on the FDTD method of analysis. Following on from there, the concept of perfectly matched layers (PML) will be discussed. From there, the specific uses of these methods in this project will be explained. Additionally, details of fabrication methods which were intended to be used for fabrication of test devices will be detailed. This will allow for suggestions to be made for the fabrication and experimental realisation of these filters.

3.1 FDTD Simulations

The Finite Difference Time Domain (FDTD) method is a numerical finite difference method for solving Maxwell's equations. It was first devised by Kane S. Yee [79] in 1966. It has become a standard method for modelling electromagnetic systems.

This section will briefly outline the method and then describe its application to this work. The simulations in this project were done in two ways. Primarily, a software package called Lumerical was used [80]. Lumerical is a piece of software which includes a graphical interface for computer-aided design of photonic structures. In addition, for this project, an additional library called MEEP was used for illustrative images. The description of the method is taken from [81] and [82].

3.1.1 Maxwell Equations With a Yee Lattice

Finite difference methods are numerical methods for solving differential equations. They use difference equations (equations which describe the relations of quantities on some form of gird

in relation to each other). They are used extensively to solve a range of different differential equations with many applications across disciplines. They have been applied to electromagnetism in the form of the FDTD. Time-domain refers to the use of finite difference methods which update in time. There is also Finite Difference Frequency Domain methods which update in frequency.

It is important to reintroduce Maxwell's equations at this point. The curl relations for anisotropic material are,

$$\frac{\partial \mathbf{D}}{\partial t} + \mathbf{J} = \nabla \times \mathbf{H} \tag{3.1}$$

$$\frac{\partial \mathbf{H}}{\partial t} = -\frac{1}{\mu_0} \nabla \times \mathbf{E} \tag{3.2}$$

With the D field field $\mathbf{D}(\omega)$ as

$$\mathbf{D}(\omega) = \varepsilon_0(\omega)[\varepsilon_r(\omega)] * \mathbf{E}(\omega) \tag{3.3}$$

with the tensor $[\varepsilon_r]$ describing the permittivity . Assuming an isotropic, dispersive medium, we can write these relations as

$$\mathbf{D}(\omega) = \varepsilon_0(\omega)\tilde{\varepsilon_r}(\omega) \cdot \mathbf{E}(\omega) \tag{3.4}$$

with the relative permittivity tensor reduced to the complex number $\tilde{\varepsilon_r}(\omega)$.

These describe the relation of a magnetic field with an electric field. A changing in time electric field induces a curled magnetic field and vice versa. These are the fundamental descriptions of electromagnetism and are used to describe the classical effects of electromagnetic radiation. They are coupled partial differential equations. Therefore, they can be discretised and approximated using a finite difference method.

Here $\tilde{\varepsilon}_r$ is the complex relative permittivity. It is this quantity that describes the proportionality between the two fields, with respect to propagation in a vacuum. It is a complex number, where the imaginary part describes loss effects in a dispersive medium.

This describes the frequency dependence of the material. It is this variable which allows for general modeling of materials such as silicon and chromium. For a dielectric material, the relative permittivity can be described as below,

$$\tilde{\varepsilon_r} = \varepsilon_r + \frac{\sigma}{i\omega\varepsilon_0} \tag{3.5}$$

where σ is the conductivity, relating the current density $\mathbf{J}$ to the electric field $\mathbf{E}$,

$$\mathbf{J} = \sigma \cdot \mathbf{E} \tag{3.6}$$

It can also be described in its real and imaginary parts,

$$\tilde{\varepsilon_r} = \varepsilon_r' + \varepsilon_r'' \tag{3.7}$$

For three dimensions, Maxwells equations can expressed as 6 scaler equations [81].

$$\frac{d\tilde{D}_x}{dt} = \frac{1}{\sqrt{\varepsilon_0 \mu_0}} \left[\frac{dHz}{dt} - \frac{dHy}{dt} \right] \tag{3.8}$$

$$\frac{d\tilde{D}_y}{dt} = \frac{1}{\sqrt{\varepsilon_0 \mu_0}} \left[\frac{dHx}{dt} - \frac{dHz}{dt} \right] \tag{3.9}$$

$$\frac{d\tilde{D}_z}{dt} = \frac{1}{\sqrt{\varepsilon_0 \mu_0}} \left[\frac{dHy}{dt} - \frac{dHx}{dt} \right] \tag{3.10}$$

$$\frac{dH_x}{dt} = \frac{1}{\sqrt{\varepsilon_0 \mu_0}} \left[\frac{d\tilde{E}y}{dt} - \frac{d\tilde{E}z}{dt} \right] \tag{3.11}$$

$$\frac{dH_y}{dt} = \frac{1}{\sqrt{\varepsilon_0 \mu_0}} \left[\frac{d\tilde{E}z}{dt} - \frac{d\tilde{E}x}{dt} \right] \tag{3.12}$$

$$\frac{dH_z}{dt} = \frac{1}{\sqrt{\varepsilon_0 \mu_0}} \left[\frac{d\tilde{E}x}{dt} - \frac{d\tilde{E}y}{dt} \right] \tag{3.13}$$

They describe the relation of an electric flux density (D), and a magnetic field (H). Here, for simplicity, the values of $\tilde{\mathbf{D}}$ and $\tilde{\mathbf{E}}$ are normalised by dividing as shown,

$$\tilde{\mathbf{E}} = \sqrt{\frac{\varepsilon_0}{\mu_0}} \mathbf{E} \tag{3.14}$$

$$\tilde{\mathbf{D}} = \sqrt{\frac{1}{\varepsilon_0 \mu_0}} \mathbf{D} \tag{3.15}$$

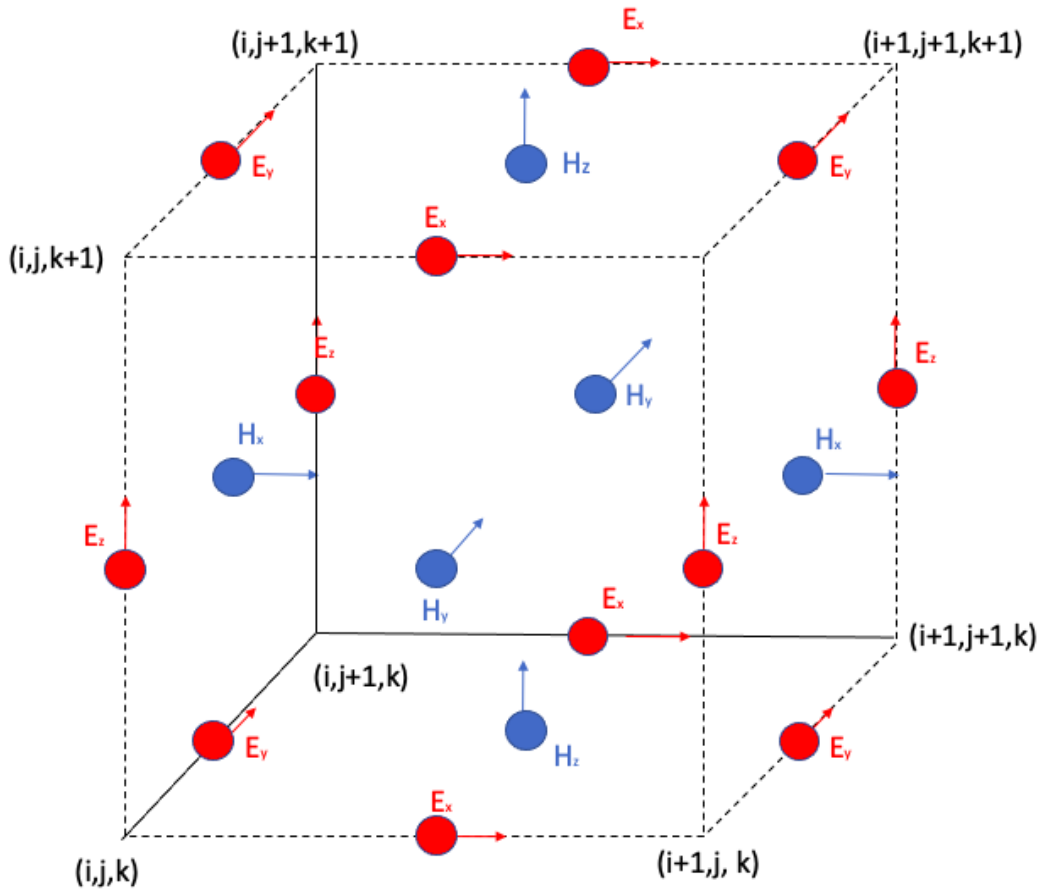

Figure 3.1: Diagram of a 3D Yee lattice. The electric field components are updated using the electric and magnetic field components from their neighbours. Here electric field nodes are in red and the magnetic, blue.

The equations can be approximated using a finite difference method in the time domain. For this, a grid system of nodes is used. This grid can be seen in figure 3.1. Here it can be seen that the electric and magnetic fields overlap, with the H field points in the y-direction with nodes positioned between those of the electric field which points in the x-direction. This grid structure is called a Yee lattice, named for its creator [79].

The various nodes of the Yee lattice hold values of either the electric or magnetic field. These are updated every time step taking into account the value of neighbouring nodes. The nodes are related by the following equations and their cyclic permutations. They are central difference approximations of the Maxwell equations shown in equations 3.8 and 3.11.

$$\frac{\tilde{D}_z^{n+0.5}(i,j,k+0.5)-\tilde{D}_z^{n-0.5}(i,j,k+0.5)}{\Delta t} = \frac{1}{\sqrt{\varepsilon_0\mu_0}}\left[\frac{H_y^n(i+0.5,j,k+0.5)-H_y^n(i-0.5,j,k+0.5)-H_x^n(i,j+0.5,k+0.5)-H_x^n(i,j-0.5,k+0.5)}{\Delta x}\right]$$

(3.16)

$$\frac{H_z^{n+1}(i+0.5,j+0.5,k)-H_z^n(i+0.5,j+0.5,k)}{\Delta t} = -\frac{1}{\sqrt{\varepsilon_0\mu_0}}\left[\frac{\tilde{E}_y^{n+0.5}(i+1,j+0.5,k)-\tilde{E}_y^{n+0.5}(i+0.5,j,k)-\tilde{E}_x^{n+0.5}(i+0.5,j+1,k)+\tilde{E}_x^{n+0.5}(i+0.5,j,k)}{\Delta x}\right]$$

(3.17)

Here the term $n = 0,1,2,3...$ is the number of the iteration, Δt is the size of the time step (difference in time between each iteration), Δx the distance each node is from its neighbour and i,j,k, the location of the node as shown in figure 3.1. These terms allow for the discretisation of the equations. This means that the time at a point in the simulation is,

$$t_n = n\Delta t \tag{3.18}$$

The value of Δt is limited by the Courant condition for numerical stability [82]. This results in,

$$\Delta t \leq \frac{\Delta x}{\sqrt{3}\,c} \tag{3.19}$$

which is required for convergence. Increasing the number of nodes in a computational cell (decreasing the value of Δx) results in a higher accuracy of simulation. With these, the value of the fields at each node (denoted by the value of (i,j,k)) can be updated iteratively. The surrounding values, and previous values of the H field, can be used to update the D field, and the E field can be used to update the H field. However, there is still the need to update the D field from the E field, taking into account the material properties as described by the complex permittivity.

In order to do this the electric field flux density $\mathbf{D}(\omega)$ needs to be expressed in the time domain. Assuming a dielectric medium, the electric flux density can be expressed in the frequency domain as,

$$D_{x,y,z}(\omega) = \varepsilon_r E_{x,y,z}(\omega) + \frac{\sigma}{i\omega\varepsilon_r} \tag{3.20}$$

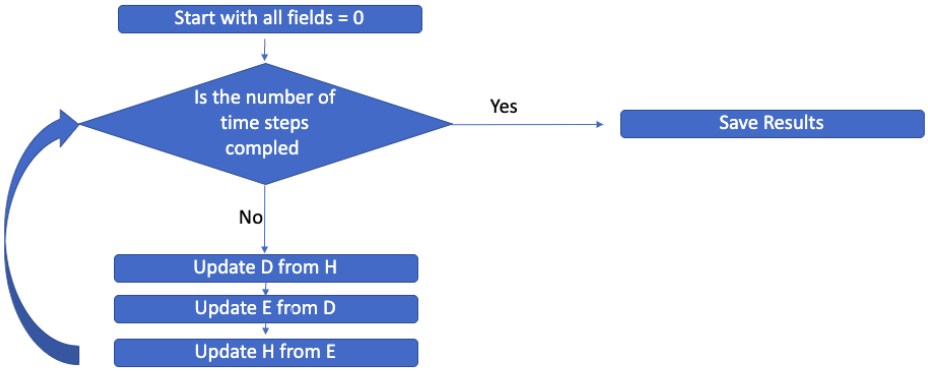

Figure 3.2: Simplified outline of FDTD process, ignoring boundaries.

Applying a Fourier transform we get,

$$D_{x,y,z}(t) = \varepsilon_r E_{x,y,z} + \int_0^t E_{x,y,z}(t')dt' \tag{3.21}$$

which can be solved by decreasing and summing over all Δt up to the n value,

$$D^n_{x,y,z} = \frac{D^n_{x,y,z} - (\sigma \Delta t/\varepsilon_0)\sum_{i=0}^{n-1} E^{i-1}_{x,y,z}}{\varepsilon_r + (\sigma \Delta t/\varepsilon_0)} \tag{3.22}$$

Therefore we can express the algorithm used for this simulation as shown in figure 3.2.

As the FDTD operates in the time domain, it can model the response of many frequencies in one simulation. This is especially useful for this work as transmission spectra can be modelled easily for a range of frequencies. Additionally, as it directly approximates Maxwell's equations in the time domain, it produces results that are simple to consolidate in animations and in intuitive graphics. This makes the method an excellent educational tool as well as making errors in its implementation easier to find. The major trade-off for its use, however, is in computational resources. Due to the discretisation, doubling the grid points in a 3D structure results in an x16 increase in computational time. This is a struggle when simulating large structures to high accuracy. Additionally, highly resonant structures require long simulation times (high numbers of n) to allow for field decay and produce useful results. As the method uses a Cartesian grid, simulation of curved structures are more complex.

3.1.2 Perfectly Matched Layers (PML)

When a numerical model such as one which uses the FDTD method is employed, consideration must be taken to address the boundary of the grid. As a waveform propagates towards the grid boundary, often it is required that it be simulated as if it is propagating to infinity. Otherwise, undesired interference can affect the simulation, causing inaccuracies in the final result.

In order to deal with the boundary condition problem, a perfectly matched layer (PML) approach can be used. This approach surrounds the computational cell edges with a medium that will absorb all frequencies without reflection. This means that there is no back reflection in the devices being simulated. There are numerous methods of implementing PML. Here we will discuss Uniaxil PML as used in the software used in this project. Good discussions of other methodologies can be found [82, 83].

Reflection at a boundary can be described in terms of the reflectance.

$$R = \frac{(1-n_1)^2 + \kappa_1^2}{(1+n_2)^2 + \kappa_2^2} \tag{3.23}$$

Where n and κ are the real and imaginary parts of the refractive index. This was seen in the explanation of backscatter.

It is useful to define the impedance here as

$$\eta = \frac{|\mathbf{E}|}{|\mathbf{B}|} = \eta_0 \sqrt{\frac{\mu_r}{\varepsilon_r}} \tag{3.24}$$

This shows that there is dependence on the loss coefficient of the refractive index on reflection at a boundary. This causes a problem when adding a perfectly matched layer. A layer of medium with the same refractive index $n_1 = n_2$ but differing κ would still induce a reflection.

Therefore, careful manipulation of the complex relative permittivity is required, to not change the impedance of the PML and the medium but demonstrate absorption.

This is done by considering an anisotopic medium. So far all materials have been assumed to be isotropic, with the same optical properties in all directions. An ansisotropic medium can be represented by substituting the complex number values of the permittivty $\tilde{\varepsilon}$ and the permeability μ_r used so far with tensors, namely,

$$[\varepsilon_r] = \begin{bmatrix} \varepsilon_{xx} & \varepsilon_{xy} & \varepsilon_{xz} \\ \varepsilon_{yx} & \varepsilon_{yy} & \varepsilon_{yz} \\ \varepsilon_{zx} & \varepsilon_{zy} & \varepsilon_{zz} \end{bmatrix} \tag{3.25}$$

$$[\mu_r] = \begin{bmatrix} \mu_{xx} & \mu_{xy} & \mu_{xz} \\ \mu_{yx} & \mu_{yy} & \mu_{yz} \\ \mu_{zx} & \mu_{zy} & \mu_{zz} \end{bmatrix}$$

(3.26)

This allows us to create a Uniaxil PML. As is shown in [84], if two tensors are set $[\varepsilon_r] = [\mu_r]$ so that,

$$[s_z] = [\varepsilon_r] = [\mu_r] = \begin{bmatrix} a & 0 & 0 \\ 0 & b & 0 \\ 0 & 0 & c \end{bmatrix}$$

(3.27)

where

$$\sqrt{ab} = 1, 1/c = a = b \tag{3.28}$$

The required properties of the PML are achieved for the boundaries perpendicular to the z-axis. For s_x we have the conditions

$$\sqrt{bc} = 1, 1/a = c = b \tag{3.29}$$

and s_y,

$$\sqrt{ca} = 1, 1/b = c = a \tag{3.30}$$

Specifying these tensor values as a material and assigning them to the outer layer grid points of a Yee lattice gives a good approximation of the perfectly matched layer in 3D and avoids the unwanted interference of other boundary approaches.

This is a useful technique; however, it is important to take a few details into account. First of all, the layers must be a distance away from any structures. Any absorption by the PML can introduce losses in the system, picking up and dissipating evanescent fields. Additionally, the finite difference implementation of PML requires a sizable number of grid points in order to be effective. This size tends to require a PML width of the order of a wavelength, and the number of points needs to be chosen accordingly, considering the value of Δx.

3.1.3 Variational FDTD Solver

For this project, large simulations of ring systems were conducted using the Lumerical MODE Solutions 2.5D VarFDTD solver. Here, the difference to the 2.5D and 3D FDTD methods will be briefly outlined, alongside its drawbacks and advantages.

The standard 3D FDTD method, as outlined in this section, is computationally intensive. When simulating larger systems, this can become a problem. An alternate approach is using a variational propagation method. In essence, this works by computing the effective indices of 3D structures. This can then be transplanted onto a 2D plane. Then a 2D FDTD Yee grid can be used to compute the electric fields. This use of a 2D grid significantly increases the computational speed that simulations are completed in.

This "collapse" of a 3D structure is done in two ways in the Lumerical software. These include a variational principle laid out by Hammer and Ivanova [85] and reciprocity theorem, as laid out by Snyder and Love [86]. These methods transform a 3D structure of optical properties into a 2D structure of effective refractive indices n_{eff}.

Once these effective materials are calculated, a 2D FDTD simulation is produced and run instead of a 3D simulation. These run under the same principles described, with discretisation, PML layers, etc. This has shown high agreement with the 3D FDTD for use with an SOI ring resonator by the manufacturer and therefore considered a reasonable approach.

Using solvers that utilise this method allow for a much quicker calculation time. This was critically important to this project. Highly resonate structures, when simulated in FDTD methods, require long simulation times in order to allow fields outside the structures to decay sufficiently. It was found that this was a major problem with the original 3D FDTD simulations produced for this project. Therefore, the 2.5 FDTD method was used to overcome this.

3.1.4 Applications in this Project

In this project, simulations were performed using two types of software. Firstly, a Python package called MEEP [65] was used to simulate images used in theory (figures 2.7 and 2.11). All other results presented used Lumerical commercial software. Simulations of the simple nanowire absorption properties were conducted using Lumerical MODE Software. The material database was used for the inclusion of the materials Si, SiO_2 and Cr. The materials NbN and $MoSi$ were simulated using refractive index data from [87]. Example ring systems can be seen in figures 3.4, and 3.5.

Simulations were originally built in 3D FDTD using the Lumerical FDTD software. However, computational resources limited their use and the simulations were instead preformed with Lumerical MODE 2.5D VarFDTD.

All simulations were built and run using Lumerical Python API. This simplified the process of building, running and analysing the simulations. Final simulations were run as the result of two python scripts. The first ran simulations for an SOI waveguide with the deposited nanowire

on-top. This allowed for the deduction of loss per unit length for waveguides with differing widths of the nanowire. This script also run simulations of various lengths of material, thus allowing for the deduction of the transmission through the absorptive region. An example structure and E field can be seen in figure 3.3.

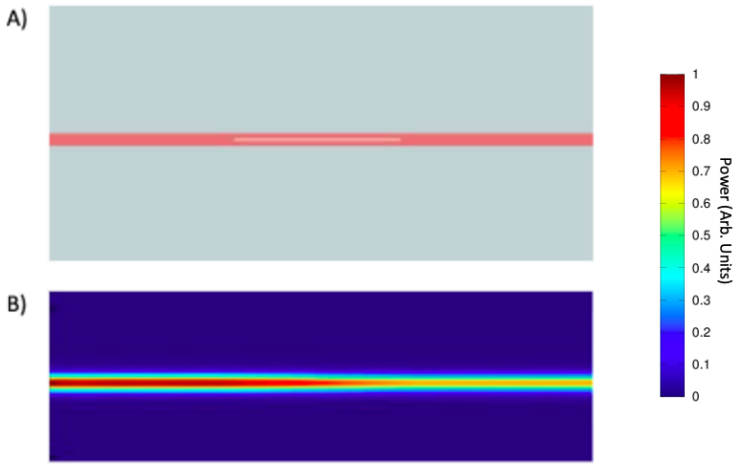

Figure 3.3: A) Example diagram of the nanowire absorption simulations. This is taken from the CAD Lumerical interface. B) Example colour map showing the loss of power.

The second script built and ran simulations of single ring systems. The script allowed for the variation of a range of parameters. These included the bend radii of the rings, the coupling length of the coupler, the width, length and height of the nanowire and the gap in the directional coupler. All of these were fixed in all simulations other than the material of the nanowire, length of the nanowire, and the gap, so that critical coupling be achieved. Here critical coupling was assumed to be present when output power was at the minimum and determined by sweeping simulations with various gaps until the minimum was determined to within $5nm$. An example structure and electric field can be seen in figure 3.4.

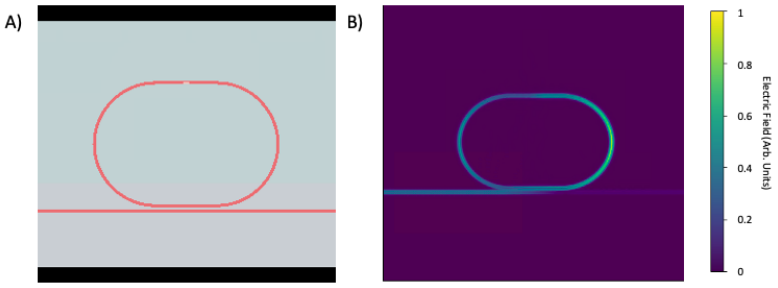

Figure 3.4: A) Example ring simulation. Here the ring has a $10\mu m$ bend radius with a $10\mu m$ coupling length. B) A colour map showing the electric field through the ring.

The final simulations were run with the same script method with the addition of multiple rings at a separation of $10\mu m$. Simulations were run for nanowire lengths of $1,2$ and $3\mu m$ and $1,2$ and 3 rings. An example simulation structure and electric field are shown in figure 3.5. These scripts are presented in the Appendix.

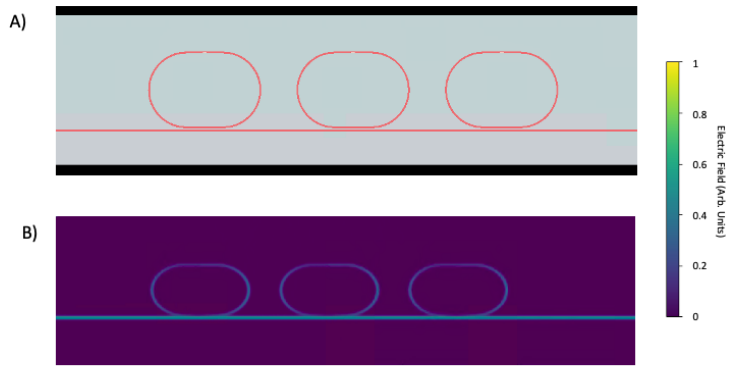

Figure 3.5: A) Example multiple ring simulation. Here 3 rings have a a $1\mu m$ nanowire and length 83 μm. B) A colour map showing the electric field through the rings.

Data from these simulations were collected into CSV files and either presented directly using python's Matplotlib or imported into Origin Lab software. Origin was used in particular for peak analysis as required for the calculation of FWHMs, extinction values, FSR and Q-Factors of filter systems.

3.2 Fabrication and Further Work

Originally, this project was planned to focus on fabrication of the filter devices. This was unfortunately not possible due to public health restrictions, disallowing laboratory work. However, as progress was made in the fabrication direction, and due to the possibility of further work being done in this space, it is useful to briefly review this work as it may be useful for further research.

For the experimental testing of the devices as described, a test process flow was designed. This involved, some key processes including Electron Beam Lithography (EBL), Inductively Coupled Plasma Reactive Ion Etching (ICP-RIE), and Physical Vapour Deposition (PVD) by evaporation. Here we will briefly discuss these processes individually and the process flow itself with suggestions for further application.

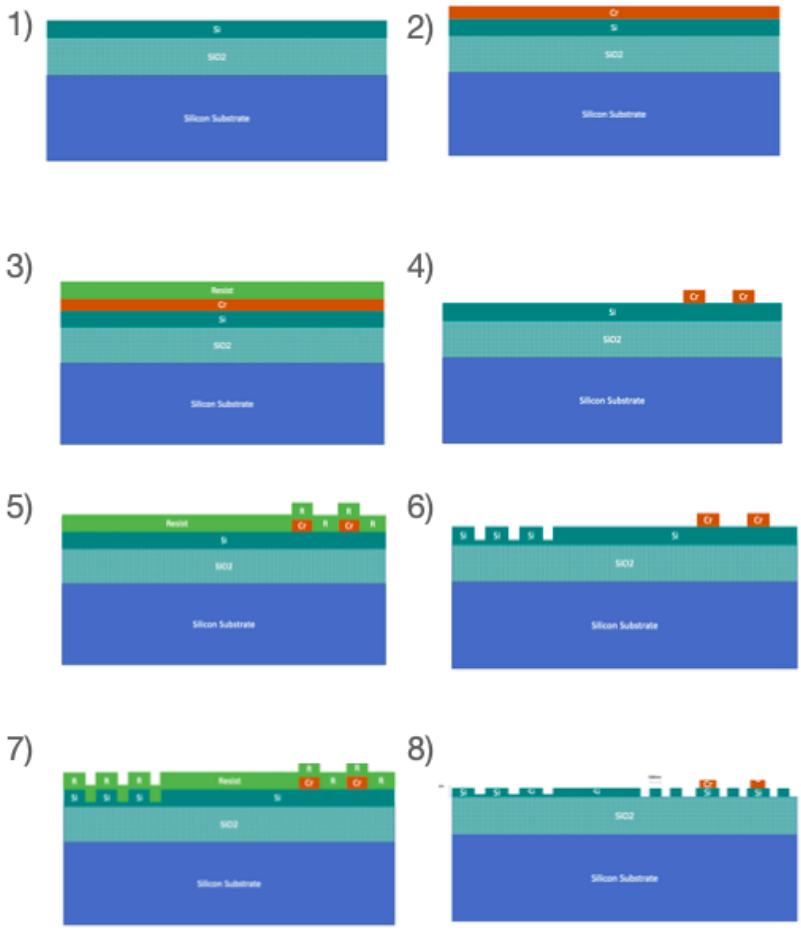

Figure 3.6: Cross sectional diagram showing the results of suggested stages of a process flow for the fabrication of devices. 1) Starting wafer 2) Deposition of of Cr by PVD. 3) Spin-coat application of resist for metal liftoff. 4) Metal liftoff. 5) Spin-coat application of resist for EBL. 6) EBL and ICP-RIE to produce silicon waveguides.7-8) Repeat of 5-6 for the creation of grating couplers.

Electron beam lithography is a form of lithography used in nanofabrication processes. Lithography is the process of imprinting some pattern into a resist. A resist is a material in which a pattern is imprinted buy changing its chemical structure. This pattern is then used in the fabrication process of some nanoscale device, normally involving some form of etching. Lithography processes are relatively mature due to extensive use in the semiconductor industry and have been refined to a remarkably high degree. There is a range of lithography processes, including photolithography and ion beam lithography.

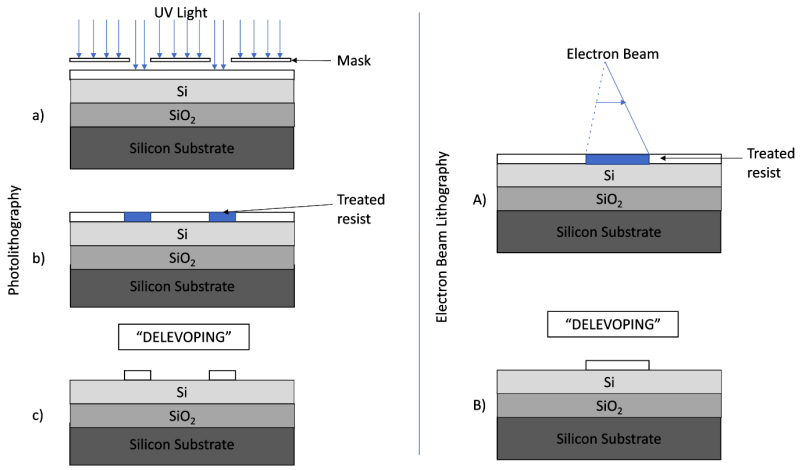

Figure 3.7: Two lithography process outlines. A physical mask is used to block light from a UV source which results in some chemical change in the resist. Left) Stages of a photolithography process. Right) Stages of a Electron Beam Lithography process.

EBL is a process which utilises a beam of electrons. The use of electron beam is advantageous due to its small diffraction effects and no need for a mask. However, the major drawback with electron beam lithography is its writing time which is much longer than comparative, mask based, lithographic techniques.

The choice of the lithography, resist and following etching process are highly dependent on one another. The resist used for a certain lithographic technique changes chemically in some way when either the electron beam or the light is present. After the resist is exposed, the un-wanted resist is removed. There are two categories of resist. Either the exposed resist is removed, leaving the desired pattern (positive resist) or the exposed resist is left on (negative resit). Both methods result in leftover resist on the material, which will affect the following etching process.

Etching refers to the process of removing unwanted and unprotected parts of a material. For SOI device nanofabrication, there are two types, wet and dry etching. Wet etching involves treating the material with chemicals which remove the parts uncovered by the resist. Dry etching uses a low-pressure plasma for the same function. In this project ion coupled plasma reactive ion etching was proposed. ICP-RIE uses a RF powered magnetic source to produce the plasma. This results in a high density plasma. Recipes made up of gases such as SF_6 and CHF_3 form a plasma when a strong electric field is applied. The alternating electric field induces and alternating magnetic field. This results in the creation of the reactive particles. The resulting reactive ions can be transported towards the lithographically treated wafer and react with exposed silicon, resulting in its removal. Choice of gases, recipe and parameters such as the flow rate of the gases, pressure and power used in the electrode needs to be monitored carefully, as they affect the resulting etch rates and by-products. These need to be optimised for surface roughness, etch rate and selectivity (ratio of etch rate of resist to target material). The careful characterisation is needed for the recipe beforehand.

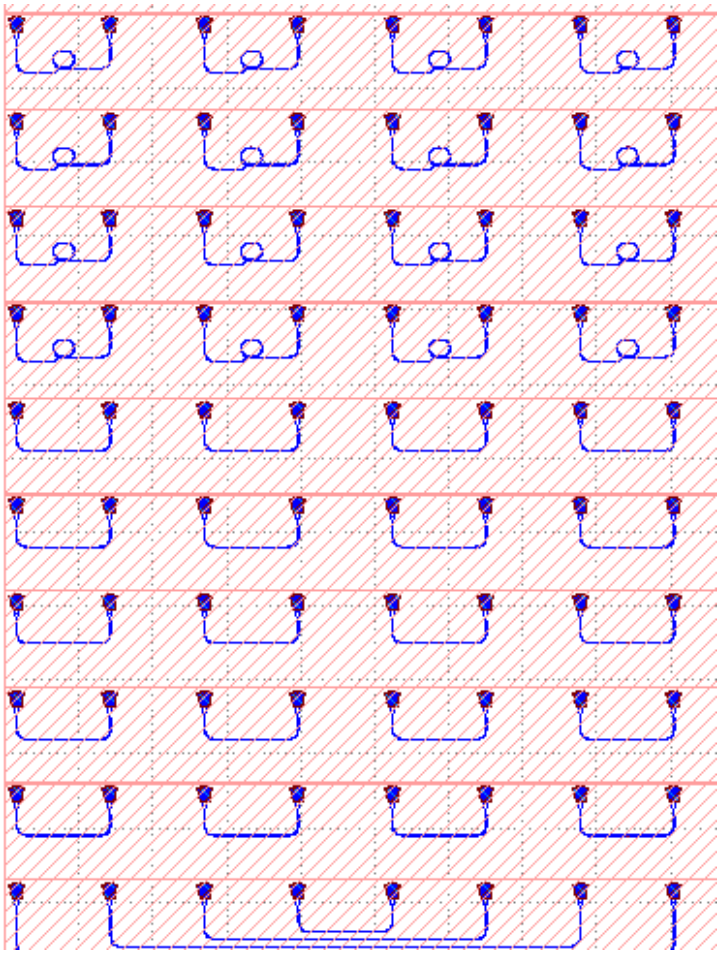

Figure 3.8: An example mask design produced for this project as a GDSII file. Single ring systems can be seen along with test structures. Various test structures featuring grating couplers and waveguides would allow for characterisation of the fabrication process, a necessary step towards the planned ultimate characterisation of the filters themselves.

In order to assess the effect of nanowires on the micro-ring filters, some form of absorptive material deposition is required. For this, Chromium was decided as a nanowire material due to its relatively simple process of deposition and its well-known properties. This deposition was proposed using physical vapor deposition (PVD). PVD describes a range of processes which deposit thin films by producing and condensing a vapour of material. For this project, an evaporation technique was proposed. Thin film deposition by evaporation takes place in a vacuum. Materials evaporated using heating elements are transported on-top of the wafer where it is condensed. In order for this to be used for the patterning of absorptive nanowire, it is used in conjunction with a lift off process. This process involves the deposition of resist and then the patterning and etching of the resist. Then the metal is deposited. Finally, the resist is developed, removing unwanted deposited material and leaving behind the nanowire.

An important consideration is the alignment of the nanowire atop of the waveguide. Similar simulations suggest that the backscatter and the absorption is dependent on the positioning of the nanowire. This is due to the overlap of the TE modes simulated with the nanowire being dependent on the position. Due to the critical dimension of proposed fabrication, this is an issue in the fabrication and design stages.

EBL setups can achieve resolutions of the order of 10s of nanometeres, with the EBL proposed for this work originally having a resolution of $30nm$. This limits the design of the nanowire as wider wires run the risk of deposition overlapping the edge of the loaded waveguide and there being variation in the deposited nanowire width and length. Careful measurement of these parameters would be key in any further experimental realisation. The error would also play a role in the effect of the resonance of the rings themselves. The coupling coefficient is exponentially dependence of the gap of the ring resonator. Therefore any use of deposition would require careful characterisation of the resonators before post processing.

The waveguides themselves can be manufactured to a high degree of width uniformality and repeatability. Previous work [88] has shown 500nm wide SOI waveguides with less than $0.5nm$ variation of width using a similar proposed fabrication process using EBL with HSQ negative tone resist. Additionally, waveguides of loss $< 1dbcm^{-1}$ were recorded using similar proposed etching chemistry. As mentioned, the major factor in the reproducability in the rings of this system would be the combination of the alignment of the nanowire to the waveguide. With the Voyager Raith system using alignment marking, this could be estimated at $60nm$ [66]. This would limit useable widths of wire to $< 400nm$ to avoid misalignment of the wire off the waveguide.

CHAPTER 4

SIMULATIONS

In order to explore the described filtering concept, numerical simulations were produced in Lumerical. These simulations allowed for comparison with the theory laid out in chapter 2. This section is split into three parts. First, absorption of the nanowire on top of a silicon waveguide will be explored. This will allow for discussion around the effects of the geometry of the nanowire. This discussion will aid any further work involving fabrication, where stringent fabrication tolerances come into play. The second section addresses the filtering process for a single ring system, detailing extinction, passband losses and comparison with the theory. Finally, the effect of a multiple ring system will be investigated numerically. This analysis considers the materials chromium (Cr, as originally planned for fabrication), niobium nitride (NbN) and molybdenum silicide ($MoSi$). These materials were chosen due to Chromium's original role in this project as a test medium and the use of NbN and $MoSi$ in SNSPDs. The refractive indices of thin films of these materials can be seen in figure 4.1

4.1 Nanowire Absorption

The first numerical simulations conducted involved the investigation of the absorptive effects of a nanowire deposited on a waveguide, as shown in figure 4.2. These simulations included an analysis of the effect of increasing length on the power transmission through the waveguide. They also included an investigation into the effects of changing the geometry of the waveguide, specifically the width of the waveguide on the absorption. In order to produce these simulations, refractive index data for thin films of NbN and $MoSi$ were taken from [87]. As a consequence, the height of all simulated nanowires in this project was set at $4.7nm$. The lengths that were investigated varied from $0\mu m - 15\mu m$ and the widths varied from $0nm - 500nm$.

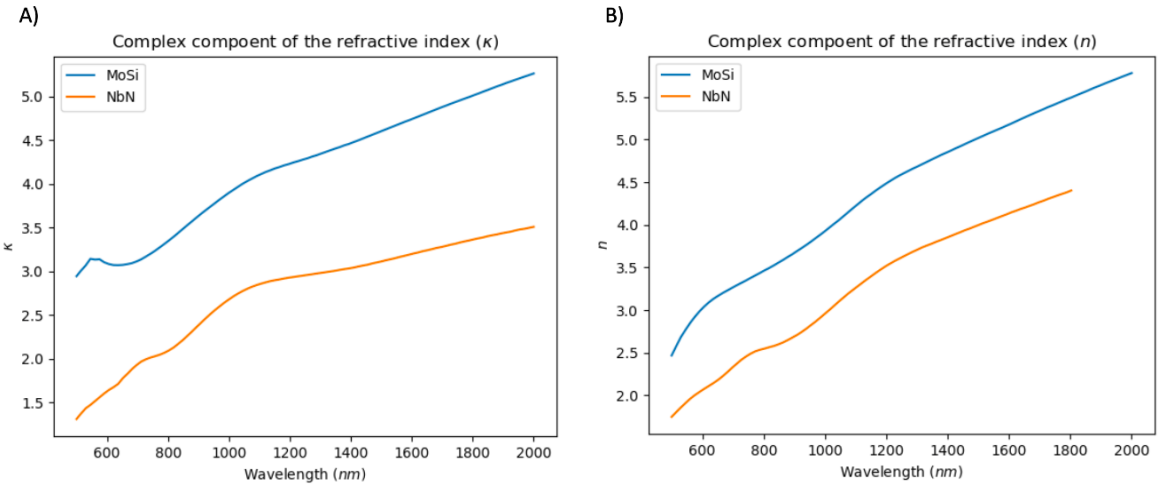

Figure 4.1: The complex and real refractive index components (κ, n) of the NbN and $MoSi$ thin films taken from [87].

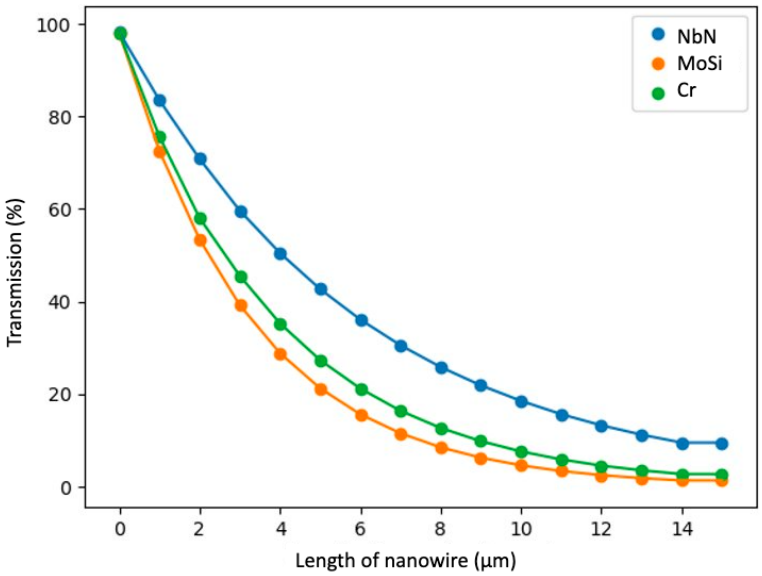

Figure 4.2: FDTD simulation of transmission as a function of the length of the nanowire. In these simulations the width of the nanowire is 0.4μm and the height is 4.7nm. exponential decay is here visible for the three materials simulated in this project, Niobium nitrate (NbN), Molybdenum silicide ($MoSi$) and Chromium (Cr). Simulations are based on optical properties from [87] for chromium and [25] otherwise.

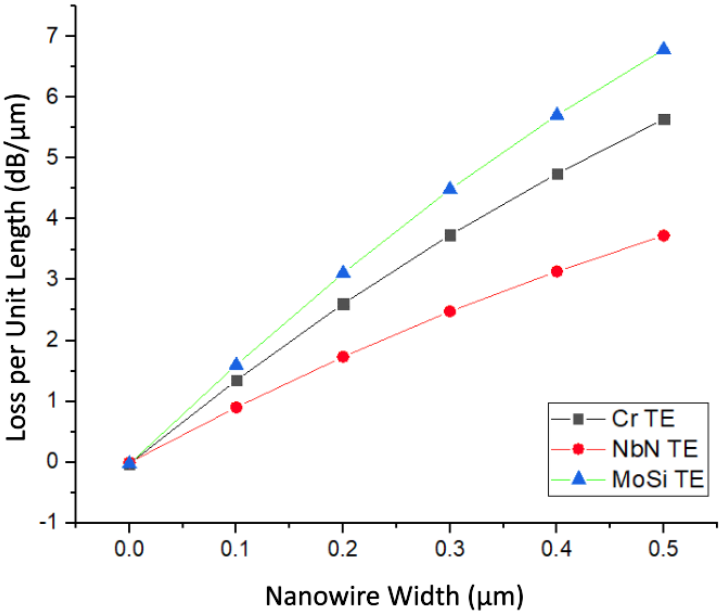

Figure 4.3: The variation of the loss per unit length a_{nw} in the absorptive region as a function of the width of the nanowire deposited above. Here the values are relevant to the fundamental TE mode present in the 220nm X 500nm waveguides used throughout this project. This simulation was produced in Lumerical MODE software using the VarFDTD solver.

The increase in the length of the nanowire clearly shows the absorptive properties laid out in chapter 2. The transmission dependence is seen for all the materials simulated. The most absorptive is $MoSi$ followed by Cr and then NbN as expected from the values of their complex refractive indices and seen in table 2.1. For all materials, the absorption saturates quickly at approximately $14\mu m$. Most of the change in the behaviour is present between the values of $0\mu m$ and $4\mu m$. It can be noted that NbN is distinctly less absorptive than the other materials. This is an important consideration when designing filters.

4.1.1 Nanowire Width

Figure 4.3 shows us that for all materials, the value of a_{nw} increases as expected with increasing nanowire width. This indicates that the effective refractive index ($n_{eff,nw}$) of the waveguide increases. It is also clear that the materials with the higher complex refractive index exhibit higher attenuation as expected. The NbN results agree with those of similar simulations done in QETLabs [66]. $MoSi$ shows the highest rate of change, varying from $1.6dB\mu m^{-1} - 6.8dB\mu m^{-1}$ for $100nm - 500nm$, respectively.

4.2 Single Ring Filters

In order to investigate the proposed systems numerically, FDTD simulations of MRR systems were conducted. These were also conducted using the Lumerical software suite Python API. This allowed for the numerical calculation of the transmission spectra as it varies with the deposition of different lengths of materials in the configuration discussed. This, in turn, allowed for the deduction of the features discussed in section 2.6.4. These include the extinction, FWHM and Q-factor. In this section, the results will be presented and discussed for these features.

In all simulations in this section, all systems were of the configuration in figure 2.20. They consisted of a ring critically coupled into the bus waveguide. These rings had a $10\mu m$ coupling region with a $10\mu m$ bend radius, resulting in a cavity length of $82.8\mu m$. Nanowires consisted of the three materials discussed with height $4.7nm$ and width $400nm$. Lengths of nanowires varied from $0.25\mu m$ to $3\mu m$, corresponding with the expected maximum difference in the transmission through the absorptive region, as shown in figure 4.2. FWHM, Q-factors, passband losses and extinctions were deduced using the equations 2.49 and 2.51 along with peak analysis tools in Origin Lab 2019b.

For this discussion, it is useful to recall the definitions of the FWHM and Q-factor in relation to the round trip transmission.

$$FWHM = \frac{(1-\sqrt{\eta}\alpha)\lambda_{res}^2}{\pi n_g L_{ring}\sqrt{\sqrt{\eta}\alpha}} \tag{4.1}$$

and

$$Q = \lambda_{res}/FWHM \tag{4.2}$$

4.2.1 Extinction

The first feature of the ring's transmission spectra to consider is the extinction recorded for the configurations. Here, average extinction across the peaks varying between $1500nm$ and $1600nm$ was recorded for the three materials with the lengths of nanowires discussed. These results can be seen in figure 4.4. The values of the extinction can be seen to generally increase with the increasing length of the nanowire. The highest extinction is present in the rings with $MoSi$ deposition with length $1\mu m$ at $24.8dB$. All extinction for all materials above $1\mu m$ were above $19dB$. These extinctions are high but do suggest the need for cascaded rings for the suppression to be comparable to existing pump suppression techniques [55, 59].

The trend is evident, but there is a large variation in the recorded results. This variation could be due to a few reasons. Sharp critical coupling peaks in the transmission spectra in the systems with less deposition could result in simulation errors. The simulation takes a sweep with

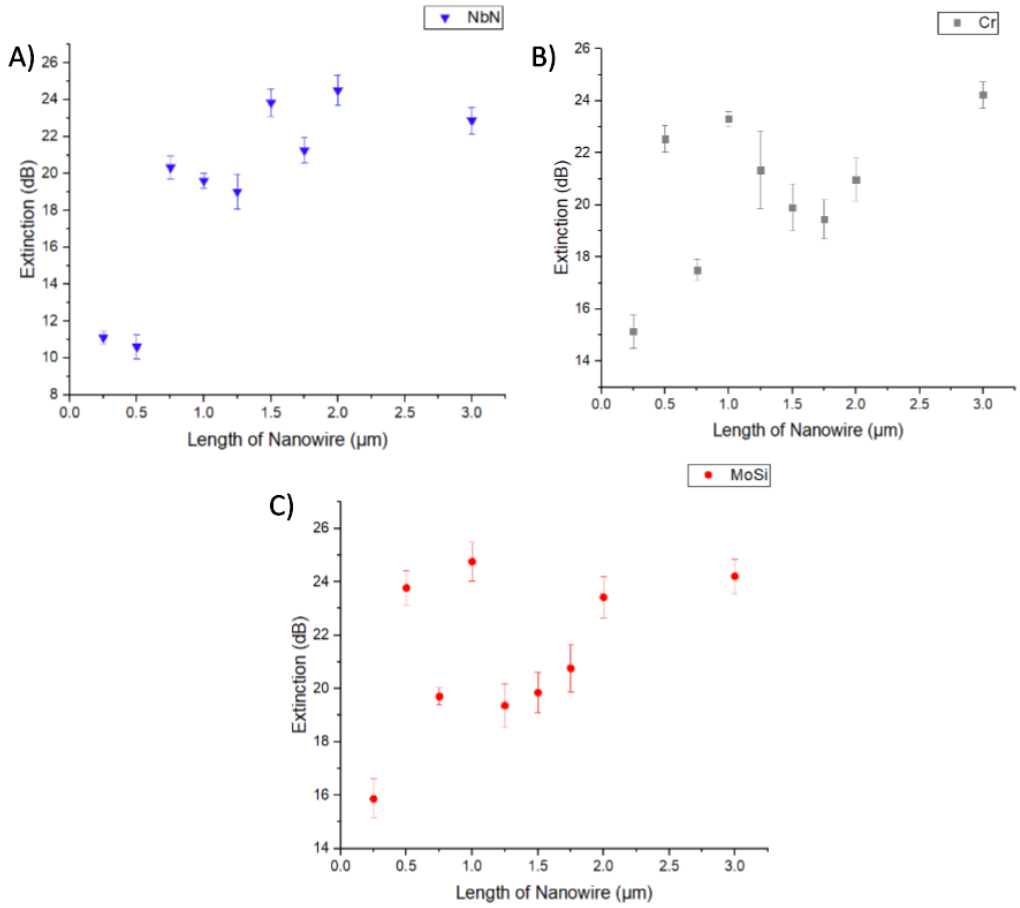

Figure 4.4: A) The simulated average extinction for all peaks in the range of 1520nm to 1580nm as a function of the length of the deposited NbN nanowire. B) The simulated average extinction for all peaks in the range of 1520nm to 1580nm as a function of the length of the deposited Cr nanowire. C) The simulated average extinction for all peaks in the range of 1520nm to 1580nm as a function of the length of the deposited $MoSi$ nanowire.

a finite number of wavelengths. With sharper peaks, it could be suggested that the maximum extinction is not recorded due to this lack of precision. This could be accounted for by running more detailed simulations with a number of higher frequency points, although this does require more computational resources than were available.

4.2.2 FWHM and Q-factor

In addition to the extinction, the FWHM was recorded for the rings. As the absorption increases with increasing nanowire length, the FWHM should also increase as described by equation 4.1. With assumed critical coupling ($\alpha = \sqrt{\eta}$), the FWHM is expected to increase with increasing absorption as the round trip transmission is decreased. Figure 4.5A shows a general increase in the FWHM. The highest recorded average FWHM was $0.85nm \pm 0.03nm$ for $MoSi$, $0.76nm \pm$

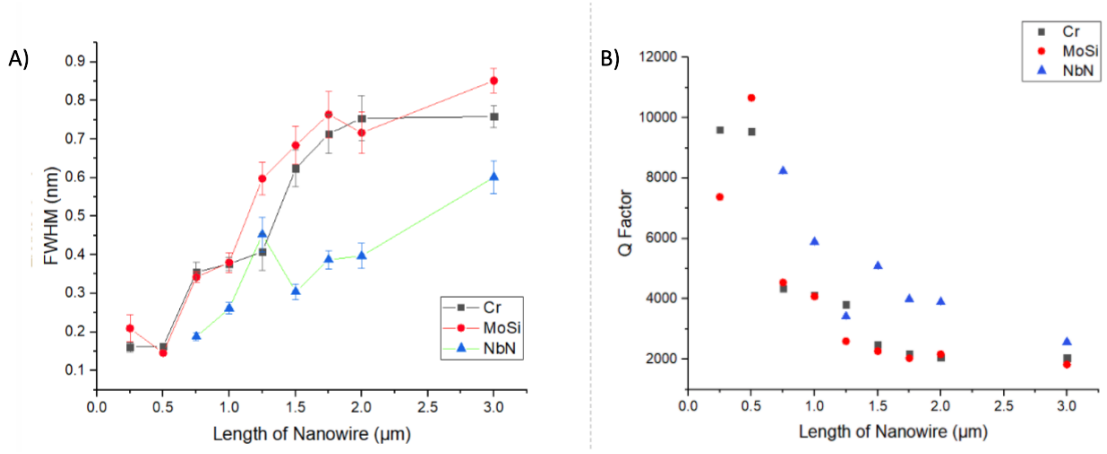

Figure 4.5: A) The simulated average FWHM for all peaks in the range of 1520nm to 1580nm as a function of the length of the deposited nanowires for all three materials (Cr, NbN and $MoSi$). B) Corresponding Q-factors for the systems in A).

$0.03nm$ for Cr and $0.60nm \pm 0.04nm$ for NbN. All of these were measured at values of the length of nanowire $L_{nw} = 3\mu m$.

This increasing trend of FWHM is also visible in figure 4.5B where the Q-factor is seen to be decreasing as expected from equation 2.51. In the Cr case, the maximum recorded Q-factor was found to be 9608 at $L_{nw} = 0.25\mu m$ decreasing to 2047 for a $L_{nw} = 3\mu m$. There is a visible saturation of the decrease of the Q-factor with the length of the nanowire. This is clearly present with the $MoSi$ and NbN cases more so than with the NbN case. This may be due to the increase in the length of the nanowire not affecting a large change in the round trip transmission for the less absorptive NbN. This is an important factor when considering fabrication as the relatively high change in the α of the ring present at these low L_{nw} for the $MoSi$ and Cr may be a challenge when small fabrication tolerances are considered.

The ability to vary FWHM would allow a post processes deposition of nanowire to fit ring systems to required filtering characteristics for specific applications. This demonstrates the benefit of this approach. Incorporation into a SNSPD detector chip would allow this to occur with minimal addition to the fabrication process. Here, NbN's apparent slower increase could be an advantage it allows for more tolerance in the length of the deposition.

4.2.3 Passband Losses

In addition to the FWHM, the passband losses on all the simulations were deduced. These losses are an important property of this project as losses to the passband will affect single-photon detection and manipulation on an integrated chip.

The relative absorptive behaviour of the materials was again present, here with $MoSi$

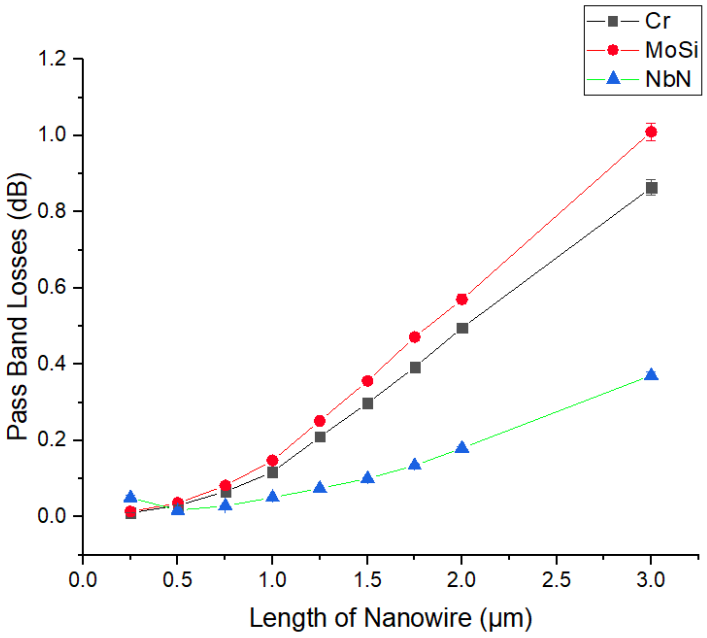

Figure 4.6: The passband losses for the the single ring systems simulated. Three materials are shown here (Cr, NbN and $MoSi$).

demonstrating the highest losses. The highest passband loss recorded was $1.01dB$ for $MoSi$ with a deposited nanowire of $3\mu m$. The corresponding maximum passband losses for Cr and NbN were $0.86dB$ and $0.37dB$ respectively.

The losses for the materials Cr and $MoSi$ are significant (corresponding to 20.7% and 18.0% respectively). The losses for NbN were significantly better with the maximum losses being 8.1% at $L_{nw} = 3\mu m$.

The passband losses can be seen to be increasing with the length of the nanowire. This is prominent at longer lengths. This is to be expected, as demonstrated in figure 2.16 and discussed in Chapter 2. This is a result of the lower Q-factor. The large losses evident in the Cr and $MoSi$ longer wavelength structures suggest that such devices would be incompatible as filters. The lower lengths do not suffer so severely; however, the losses are still significant. NbN shows losses less than $0.4dB$ consistently throughout these simulations, even at the maximum length of $3\mu m$. This suggests the material's greater applicability to this scheme.

4.3 Multiple Ring Systems

Furthering work done on the single ring systems as discussed in the previous section, systems with multiple rings were investigated. Systems with up to three rings were simulated with the three materials focused on in this project. Cascaded rings may be required to reach extinction

levels comparable to other work [59, 89]. The dimensions of the rings were identical to the rings in the previous section, namely with a coupling region of length and bend radius of $10\mu m$. The values of the extinction and the FWHM for the resulting transmission spectra were collected and are presented here.

4.3.1 Extinction

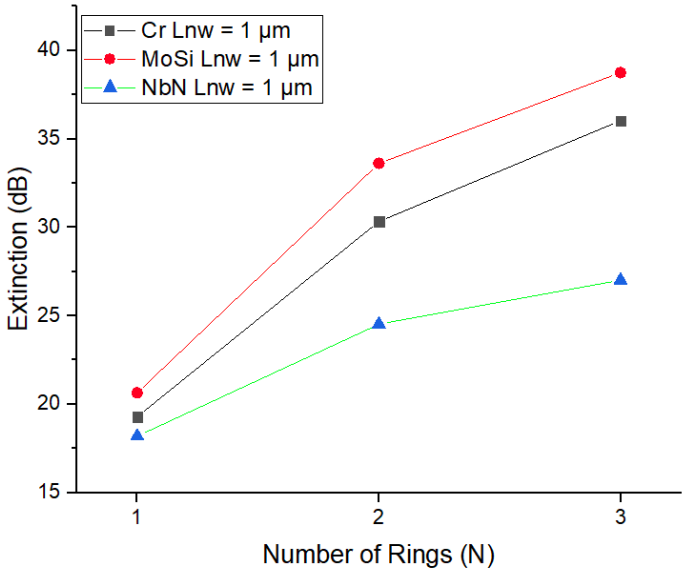

Figure 4.7: The maximum extinction measured for the multiple ring systems up to the three ring systems. $MoSi$, NbN and Cr are all shown.

Figure 4.7 shows the maximum extinction for systems with deposited nanowire of length $1\mu m$. Measurements were made for $N = 2$ and $N = 3$ rings in addition to that of the single ring systems, with a seperation of $10\mu m$. The extinction can be seen to be increasing with the number of rings resulting in the highest extinction found in a three-ring system with $3\mu m$ deposited nanowire of $MoSi$. This result was found to be $46.8dB$. The corresponding values for the Cr and NbN were found to be $43.1dB$ and $30.0dB$ respectively.

The addition of multiple rings is expected to decrease the output power as described by equation 2.55. The maximum recorded extinction value is $47.8dB$. This was present in the $MoSi$, $N = 3$ ring system with $L_{nw} = 2\mu m$. The results follow a similar trend for the Cr material with the maximum extinction recorded at $43.0dB$. The highest extinction for the NbN systems was found to be $46.9dB$ for the $N = 3$ ring system with $L_{nw} = 2\mu m$. Figure 4.7 shows the increase for the rings of the three materials with $L_{nw} = 1\mu m$. A general increase is seen in the rings. However, there is a noticeable decrease in the final ring output. It could be suggested that this is the result of backscatter effects, resulting in peak splitting at high extinctions.

4.3.2 FWHM

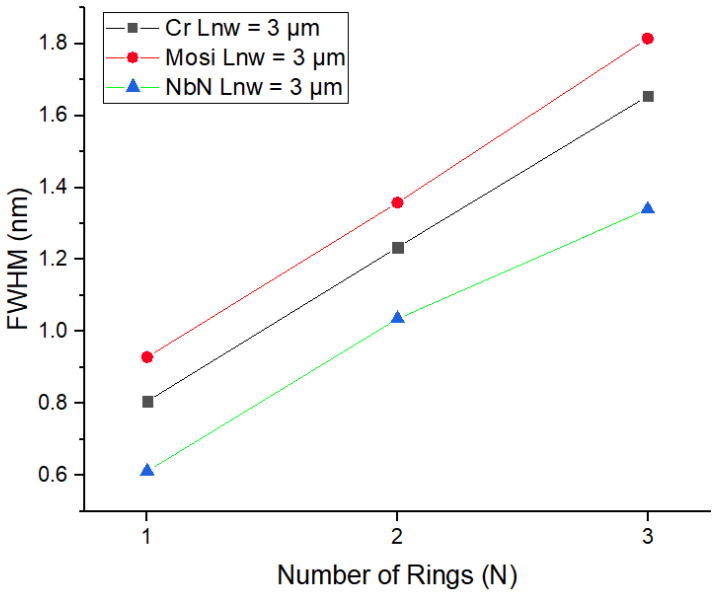

Figure 4.8: The FWHM of the filtering systems with a deposited $3\mu m$ nanowire as a function of the number of rings. The three materials Cr, $MoSi$ and NbN are shown here.

In addition to the extinction the FWHM was also recorded from the transmission spectra. The average FWHM can be seen in figure 4.8. The FWHM is seen to be increasing with the number of rings. This is true for all materials, with the maximum FWHM being recorded for the three-ring system with $3\mu m$ of $MoSi$. This was recorded as $1.8nm$. The corresponding values for Cr and NbN were recorded as $1.7nm$ and $1.4nm$.

The FWHM increased consistently with the number of rings present as can be seen in figure 4.8. This graph shows the results for the respective systems with $3\mu m$ deposition. This is to be expected from the compounding effects of multiple rings. This suggests widening of the linewidth with increasing N. This is an important consideration in practical application as post process tuning will become more significant with more rings.

4.3.3 Passband Losses

The final simulation results presented in this thesis concern the passband losses present in multiple ring systems. The results are shown here in figure 4.9 A-C. They show the increase for all materials present from increasing nanowire length as discussed, as well as a clear increase in gradient due to the number of rings.

The highest passband losses were present in the $MoSi$ rings, as suggested by figure 4.6. The maximum passband losses were recorded in the $MoSi$ systems $3\mu m$ $N = 3$ system. This

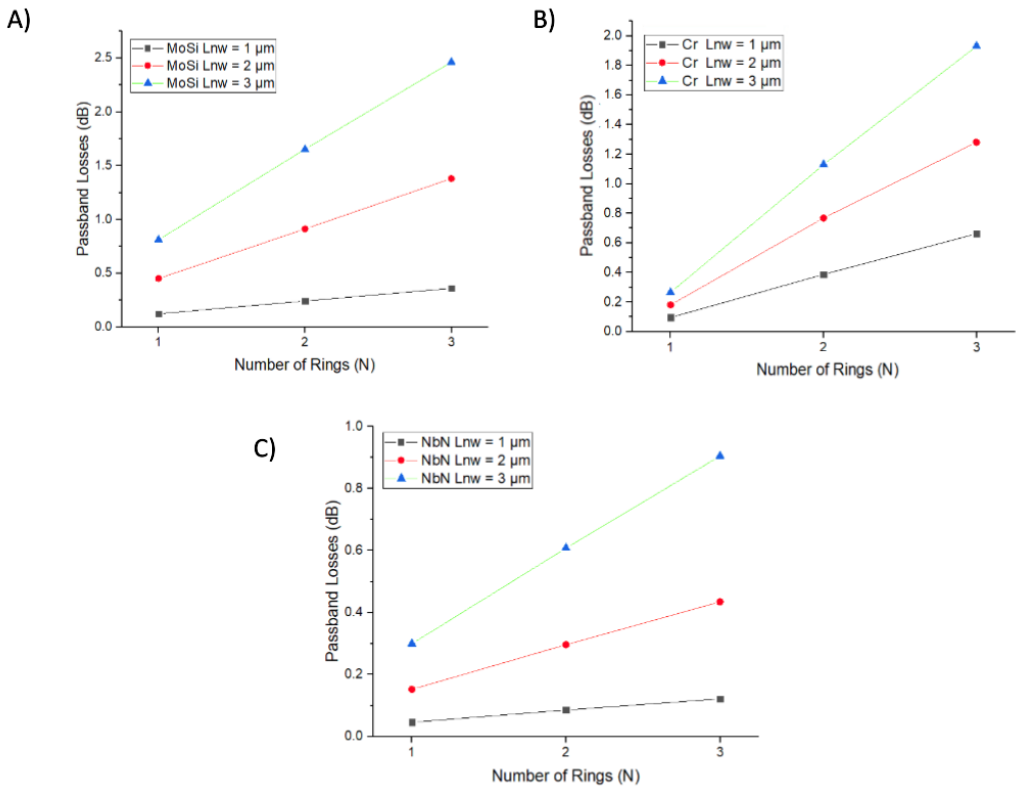

Figure 4.9: A) The passband losses for rings with a deposited $MoSi$ nanowire. Three lengths of the nanowire are shown here $1\mu m$, $2\mu m$ and $3\mu m$. B) The passband losses for rings with a deposited Cr nanowire. Three lengths of the nanowire are shown here $1\mu m$, $2\mu m$ and $3\mu m$. C) The Passband losses for rings with a deposited NbN nanowire. Three lengths of the nanowire are shown here $1\mu m$, $2\mu m$ and $3\mu m$.

was recorded as $2.5dB$. The corresponding results for Cr and NbN were $2.0dB$ and $0.9dB$ respectively

The passband sees a significant increase per rings. For Cr and $MoSi$ systems of $N > 2$, losses are greater than $0.4dB$. This would pose a major drawback for practical applications for the multiple ring systems and effectively eliminates the possibility of systems with more rings ($N > 3$) as losses would become too great. This suggests these materials are less applicable to this filtering application. Systems here with NbN suffer less from these losses. For systems of all N with $L_{nw} \leq 3\mu m$, all passband losses were less than $0.4dB$. It is important to note here that the simulations did not consider any insertion or coupling losses, so for any experimental work, total losses in the passband would be exacerbated.

Material	Reflectance at 1550nm (dB)
Cr	-42.1
NbN	-45.8
MoSi	-40.6

Table 4.1: Measured reflectance due to the absorptive region. Here presented are values at 1550nm for the three material's fundamental TE mode.

4.3.4 Backscatter

As discussed in Chapter 2, the addition of a nanowire on top of the waveguide in the ring would result in an intrinsic back reflection as described by equation 2.56. This, along with contributions from back reflections from the directional coupler, would result in the excitation of a mode in the ring propagating counter to the designed mode. This is wavelength selective and would result in a splitting of the wavelength peak.

Table 4.3.4 shows the reflectance for the TE modes for the three materials discussed at the boundary of the absorptive nanowire at $1550nm$ wavelength. They are all of the order of $40dB$. The highest recorded is that of for NbN ($45.8dB$) followed by Cr ($42.1dB$) and finally $MoSi$ ($40.7dB$).

However, for the ring simulations, observable splitting was seen for some rings. This was especially present in the high extinction $N = 3$ systems. An example is shown in figure 4.10. Although results are inconclusive, it could suggest an effective limit on the utility of the passive rings solely as filters for quantum optics use.

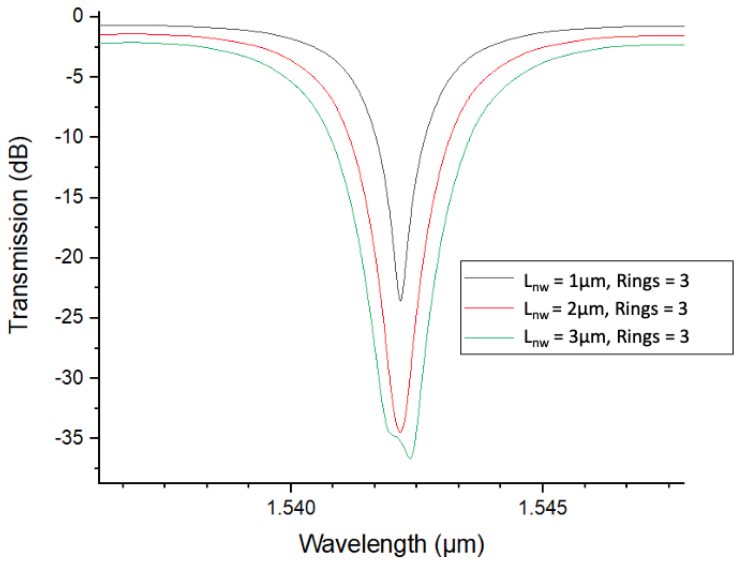

Figure 4.10: Example transmission spectra of cascaded $N = 3$, $MoSi$ systems. Visible peak splitting can be seen at the higher L_{nw} with higher extinction.

4.3.5 Summary

In this section, a range of features of MRR filters with deposited nanowires has been investigated. In summary, the addition of the nanowires exhibited expected effects, increasing FWHM and a noticeable trend of increasing extinction was observed. This demonstrates the possible advantage of this approach. However, as expected, passband losses were found to be dependent on both materials as well as the level of deposition. These losses were significant at higher L_{nw}, limiting the filtering capacity. Finally, at high extinction, backscatter effects came into play, limiting the maximum extinction.

Although highest extinction was found in systems of $MoSi$, significant passband losses suggest it is not an optimum material for this filtering application. NbN does not suffer the same passband losses for the systems investigated. For further investigation, deposition of NbN would be the suggested material as a combination of these lower passband losses, combined with similar extinction behaviour to the other materials suggest it is more desirable for this application. The inclusion of Cr in this work was to investigate its potential use as a proof of concept material. As it cannot be used in SNSPDs, the benefits to the fabrication process flow, for final detector chip for example, are not so evident. However, this work does suggest it could be used as a test material, as was originally proposed for this work, as all trends found are evident in its application.

4.3.6 Filtering Characteristics and Discussion

All the filters shown show some of the promising properties of the MRR approach to filtering. These include a relatively small linewidth ($< 2nm$). The linewidths were found in 3 ring multiple ring systems at $1.8nm$. In addition, extinction ratios are high, however not as high as some of the other schemes [55]. Here all rings had extinction varying form $16dB$ to $47dB$, with the higher extinction present in multiple ring systems. This is comparable with other ring based geometries demonstrated [61, 90], alongside MZI and BR geometries, yet is not the state of the art. Limits on the extinction seemed to be partly a result of back scattering effects, as evident in peak splitting. The nanowire does, therefore, seem to restrict the effectiveness of this filtering system to, by itself, meet the high extinction ratios required for pump filtering. It would seem increasing the number of rings to meet $100dB$ would exacerbate the two keys flaws in the design, namely backscatter and passband losses. Backscatter could be reduced by editing the geometry of the wire, making it thinner, or by using less absorptive materials such as NbN. However, the effects of the passband losses cannot be avoided as this is a unavoidable property of this lower Q-factor regime. The trade off between reducing the build-up of the electric field and allowing for wider control of the linewidth is that the passband losses are potentially high. If these rings were to be used in a filtering system on chip, it would have to be in conjunction with other devices such as the rings used in [59], perhaps alongside BRs or MZIs. Here the high extinctions could be reached but the flaws of the wider bandwidth and their thermal tuning, particularly in the MZI case, would still

be present. Additionally, the size could be an issue, thus reducing an advantage in the rings in scalability terms.

The rings do show limited promise in the post processing of preformed filters. Producing under coupled rings and then using the post process deposition of the nanowires could realise critical coupling, reducing the stringent fabrication tolerances required in fine engineering of the gaps required to realise critical coupling. The exponential dependence of the coupling coefficients in ring to the gap is the main constraint on the achievement of critical coupling. However, this approach may not be a necessary advantage as there would still be small ($10nm$) precision required in the deposition process, particularly when considering reducing the backscatter by altering the width. This may not be as much of an issue with modern EBL techniques, and this precision issue would still be present if detection on the same chip is done with SNSPDs due to their stringent critical dimensions. All this considered, a key finding of this work is the high absorption of the $MoSi$ would rule it out of any application along these lines, even before fabrication is considered.

Concluding the discussion of the application of the modelled ring system to pump filtering, it seems that it would not be advisable to use such systems solely to address pump suppression. The issues resulting from backscatter, passband losses and fabrication difficultly make this the case.

Improvement to this work that could be suggested include investigation of nanowires of smaller width to investigate its effect on the limitations discussed. The $400nm$ nanowire modelled here showed strong effects in the resulting transmission spectra at relatively short lengths of nanowire. As suggested by figure 4.3, shorter width would reduce the significant passband losses at short nanowire lengths L_{nw}. The resulting decreased rate of change of absorption with L_{nw} would allow for the designing of longer nanowires. The significant backscatter effects should also be considered. Results in this project are inconclusive, but it could be proposed that reduced width of nanowire would reduce these effects. Similar simulations [66] suggest smaller widths result in lower coefficients of reflectance. Further simulations are suggested. A focus on the backscatter affecting the extinction of the peaks and comparison with existing models [78] would enlighten this limitation.

Additionally, further experimental work is suggested. As mentioned, a key recommendation of this project is the investigation of smaller width nanowire with longer lengths. As noted in [66], and repeated here, sweeping of directional coupler gaps would be required due to errors in the simulation techniques. This mainly arises form the assumption of low loss silicon, $\alpha_{si} \approx 0$, which would not be the case as surface roughness and impurities would come into play. This would increase round trip losses and therefore require higher reflectance in the directional coupler. Critical coupling would have to be found for optimum extinction, by reducing coupling gaps (C). It is suggested that undeposited rings be produced in the overcoupled regime (small C, $\alpha < \sqrt{\eta}$). Then critical coupling could be achieved by post-processing a nanowire on top, increasing α.

Various increasing lengths would be required to find the optimum.

Additionally, enhancing the extinction by including narrowband filters of other geometries may produce high extinction. This could include the addition of BR or as MZI, However the MZI requirement of tuning would increase complexity of design.

CHAPTER 5

CONCLUSIONS

In this project, the prospect of utilising MRRs for pump suppression filtering was investigated. Pump filtering is required for non-linear processes such as SFWM used for the generation of single photons. These filters could be used as part of an integrated photonic chip. Such a chip could be used in a range of maturing quantum information technologies. This project focused on the simulation of such devices, continuing work by Mack Johnson [66]. The filtering system in question consists of a micro-ring resonator fabricated in Silicon-on-Insulator with the addition of a absorptive material placed atop the ring waveguide.

Systems as described were simulated using Lumerical software and an FDTD method. Three materials of nanowire were chosen, chromium (Cr), molybdenum silicide ($MoSi$) and niobium nitrite (NbN). The first material was originally proposed to test the concept by fabrication. The other two are used in SNSPDs. Single ring systems were compared using features such as FWHM, Q factor, passband losses and extinction. The nanowires were of width $400nm$ with height $4.7nm$ and varying length form $0.25 - 3\mu m$. These simulations were repeated for systems with multiple rings, up to three.

The maximum extinction was found to be $24.8dB$ for a single ring system with $MoSi$ nanowire of length $3m$. Results for the other materials were comparable. The maximum FWHM for the $MoSi$, NbN and Cr rings were also present for rings with the $3m$ nanowires. These were found to be $0.85nm$, $0.60nm$ and $0.76nm$, respectively.

Similar measurements were made for multiple ring systems. Systems with the same geometry where simulated with a number of rings up to three. The increase in the ring number had the expected effect of increasing the extinction and the FWHM. The maximum extinction was found to be present in $MoSi$ system of three rings with the maximum investigated length of deposited nanowire, $3\mu m$. This was recorded as $46.8dB$. The corresponding values for Cr and NbN were

found to be 43.1dB and 30.0dB respectively. The maximum value of the FWHM was found in the same ring systems for each material. For $MoSi$, Cr and NbN the FWHM were found to be 1.8nm, 1.7nm and 1.4nm, respectively.

All these findings suggest that the addition of the nanowire may increase the applicably of MRR to pump suppression in specific circumstances. These would be for when control over the linewidth is desirable at the design stage without the use of active tuning. However, due the fabrication issues that are present in the proposed process flow, along with the strong filtering requirements required for application to the quantum regime, it is not suggested that the configuration be used for the filtering problem described in this work.

The wire demonstrated two key effects of note. These are increasing the linewidth and the extinction. The increase of the extinction shown in this work is not so large as to justify the sole use of the scheme. A suggestion of further work is made by the simulation and possible fabrication of these rings in conjunction with other filtering schemes such as Bragg reflectors, MZIs or CROWs. Similar combinations have been shown with promising results [55, 59]. This proposed addition, however, may limit the usefulness of any increasing linewidth for increasing purity as the lower bound for the linewidth would most probably be set by the inclusion of the additional devices and variation in the geometry of the nanowire would have little effect in the final filtering characteristics. Additionally, the limits on the fabrication tolerances of current EBL based techniques set stringent limitations on the geometry allowed, and thus, severely limits the real world application of such nanowire devices. Passband loss where also seen to increase with increased deposition. Finally, backscatter effects would come into play, limiting any possible extinction from such rings due to observable peak splitting. Simulations here where not conclusive to quantify this effect and further investigation is suggested. All these considerations would most probably out-way the benefits of the system. These benefits include the suppression of the electric field in the rings, reducing the generation of unwanted photon pairs, as well as design control over the linewidth with possible application to increasing purity [61].

Further work that is suggested from here would include the simulation of other similar schemes with the design goals of maximising extinction. A setup similar to [59] with the inclusion of Bragg reflectors is suggested as a starting point. Generally, it is also suggested that other methods than those proposed be investigated. Notable simulation work which could be applied to the filtering problem in SOI could be that of inverse design [91] to open up new ways of addressing the problem for quantum applications

APPENDIX A

In the following appendix, python code used to create and run all the simulations presented in the simulations section of this thesis are presented. The first script runs simulations for the investigation of absorptive nanowire. The second simulates the rings, both single and mutiple rings. Although originally planned to be in Lumerical FDTD, the VarFDTD solver was chosen in the interest of time and computational resources. All the scripts presented hear require Python 3.6 along side Numpy, Matplotlib, Imp and access to the Lumerical Suite API.

Additionally in this project, the python package MEEP was used to created illustrative simulations in figures 2.11 and 2.13.

A.1 Nanowire Absorption

The following script was used to create and run all simauations of the waveguide with aborptive nanowire

```
import imp
lumapi = imp.load_source("lumapi", "PATH_TO_LUMAPI\\lumapi.py")
import numpy as np
import matplotlib.pyplot as plt
mode = lumapi.MODE()
#import pandas
from scipy import interpolate

"""
The following function builds, runs and saves a simulation of an SOI waveguide with a nanowire deposited ontop.
The keyword arguments set out the parameters of the simulation. These parameters include all relevant geometry waveguide,
as well as the nanowire (Height, Width, Length). The data is collected by 9 monitors located at even postions allong the
length of the nanowire. This allows for simulation of the transmission. The materials for the waveguides and are set as
Silicon. The materials for the nanowire can be set by kwarg. This will require the addition of the optical property
data the Lumerical materials database before running.
```

```
"""

Lcs =  np.linspace(0.0000000001e-6, 2e-6, 5)

Lnws = np.linspace(0.0e-6, 1e-6, 5)

def WanveguideAndNanowireSim(HeightOfStructure = 0.22e-6,
                        WidthOfWaveguides = 0.5e-6,
                        Wnw = 0.2e-6,
                        Lnw = 1e-6,
                        Hnw = 4.7e-9,
                        x_span = 50e-6,
                        Lc = 2e-6,
                        radius = 3.1e-6,
                        gap = 0.266e-6,
                        Nanowire_Material ="k",
                        frequency_points = 100,
                        simulation_time = 5000e-15,
                        mesh_accuracy = 8
                        ):
    mode.switchtolayout()
    mode.selectall()
    mode.delete()

#-----------------Stuctures-----------------------------
    #-----------------BOX-----------------
    mode.addrect()
    mode.set("name","SiO2")
    mode.set("z", -5.11e-6)
    mode.set("x", x_span/2)
    mode.set("y", 0)
    mode.set("x span", 2*x_span)
    mode.set("y span",40e-6)
    mode.set("z span", 10e-6)
    mode.set("material", "SiO2 (Glass) - Palik")

    mode.addwaveguide()

    #-----------------Bus-----------------
    mode.set("z", 0)
    mode.set("x", 0)
    mode.set("y", 0)
    mode.set("name", "Bus")
    mode.set("Base Width", WidthOfWaveguides)
    mode.set("Base Height", HeightOfStructure)
    mode.set("Base Angle", 90)
    pole = np.array([[0,0],[x_span,0]])
    mode.set("poles", pole)
    mode.set("material", "Si (Silicon) - Palik")

    #-----------------Nanowire-----------------
    mode.addrect()
    mode.set("name", "Nanowire")
    mode.set("x span",Lnw )
    mode.set("y span",Wnw )
```

```
    mode.set("z span", Hnw)
    mode.set("x", x_span/2)
    mode.set("y", 0)
    mode.set("z", HeightOfStructure/2+Hnw/2)
    mode.set("material", Nanowire_Material)

#----------------varFDTD and Sources----------------------------

    mode.addvarfdtd()

    mode.set("mesh accuracy", mesh_accuracy)
    mode.set("simulation time", simulation_time)
    mode.set("x",x_span/2)
    mode.set("x span",x_span)
    mode.set("y",0)
    mode.set("y span",WidthOfWaveguides*10)
    mode.set("z",0)
    mode.set("z span",0.3e-6)

    mode.addmodesource()
    mode.set("x", 0e-6)
    mode.set("y", 0)
    mode.set("y span", 1e-6)
    mode.set("wavelength start", 1.5e-6)
    mode.set("wavelength stop", 1.6e-6)

    mode.setactivesolver('varFDTD')

    """
    mode.addprofile()

    mode.set("name", "Profile")
    mode.set("x", x_span/2)
    mode.set("y", 0)
    mode.set("y span", WidthOfWaveguides*10)
    mode.set("x span", x_span)
    """
#----------------Monitors---------------------------

    mode.addpower()
    mode.set("override global monitor settings", True)
    mode.set("frequency points", frequency_points)
    mode.set("name", "Out")
    mode.set("x span", 0)
    mode.set("y span", 2*WidthOfWaveguides)
    mode.set("y", 0)
    mode.set("x", x_span)

    #----------------Transmission Monitors----------------------------
    mode.addpower()
    mode.set("override global monitor settings", True)
    mode.set("frequency points", frequency_points)
    mode.set("name", "1")
    mode.set("x span", 0)
    mode.set("y span", 2*WidthOfWaveguides)
```

```
mode.set("y", 0)
mode.set("x", x_span/2 -(Lnw/2))

mode.addpower()
mode.set("override global monitor settings", True)
mode.set("frequency points", frequency_points)
mode.set("name", "2")
mode.set("x span", 0)
mode.set("y span", 2*WidthOfWaveguides)
mode.set("y", 0)
mode.set("x", x_span/2 -(Lnw/2)+Lnw/8)

mode.addpower()
mode.set("override global monitor settings", True)
mode.set("frequency points", frequency_points)
mode.set("name", "3")
mode.set("x span", 0)
mode.set("y span", 2*WidthOfWaveguides)
mode.set("y", 0)
mode.set("x", x_span/2-(Lnw/4))

mode.addpower()
mode.set("override global monitor settings", True)
mode.set("frequency points", frequency_points)
mode.set("name", "4")
mode.set("x span", 0)
mode.set("y span", 2*WidthOfWaveguides)
mode.set("y", 0)
mode.set("x", x_span/2-(Lnw/4)+Lnw/8)

mode.addpower()
mode.set("override global monitor settings", True)
mode.set("frequency points", frequency_points)
mode.set("name", "5")
mode.set("x span", 0)
mode.set("y span", 2*WidthOfWaveguides)
mode.set("y", 0)
mode.set("x", x_span/2)

mode.addpower()
mode.set("override global monitor settings", True)
mode.set("frequency points", frequency_points)
mode.set("name", "6")
mode.set("x span", 0)
mode.set("y span", 2*WidthOfWaveguides)
mode.set("y", 0)
mode.set("x", x_span/2 +Lnw/8)

mode.addpower()
mode.set("override global monitor settings", True)
mode.set("frequency points", frequency_points)
mode.set("name", "7")
mode.set("x span", 0)
mode.set("y span", 2*WidthOfWaveguides)
mode.set("y", 0)
```

```
    mode.set("x", x_span/2+(Lnw/4))

    mode.addpower()
    mode.set("override global monitor settings", True)
    mode.set("frequency points", frequency_points)
    mode.set("name", "8")
    mode.set("x span", 0)
    mode.set("y span", 2*WidthOfWaveguides)
    mode.set("y", 0)
    mode.set("x", x_span/2+(Lnw/4)+Lnw/8)

    mode.addpower()
    mode.set("override global monitor settings", True)
    mode.set("frequency points", frequency_points)
    mode.set("name", "9")
    mode.set("x span", 0)
    mode.set("y span", 2*WidthOfWaveguides)
    mode.set("y", 0)
    mode.set("x", x_span/2+(Lnw/2))
    #----------------Effective index----------------------------
    mode.addeffectiveindex()
    mode.set("name", "neff")
    mode.set("x", x_span/2)
    mode.set("y", 0)
    mode.set("y span", WidthOfWaveguides)
    mode.set("x span", x_span)

#----------------Running the Simulation----------------------------

    mode.save("FINALWaveAndNanoSim_"+str(simulation_time)+
                "_ma"+str(mesh_accuracy)+
                "_Wnw"+str(Wnw)+ "_Lnw"+str(Lnw))
    mode.run()

#----------------Retreiving the Data----------------------------
    return (np.absolute(np.max(mode.getresult("Out", "P")["P"])),

    mode.getresult("1", "T")["T"],
    mode.getresult("2", "T")["T"],
    mode.getresult("3", "T")["T"],
    mode.getresult("4", "T")["T"],
    mode.getresult("5", "T")["T"],
    mode.getresult("6", "T")["T"],
    mode.getresult("7", "T")["T"],
    mode.getresult("8", "T")["T"],
    mode.getresult("9", "T")["T"],
    mode.getresult("1", "E")["lambda"],

    np.absolute(np.max(mode.getresult("1", "E")["E"])),
    np.absolute(np.max(mode.getresult("9", "E")["E"])),
    np.absolute(np.max(mode.getresult("1", "H")["H"])),
    np.absolute(np.max(mode.getresult("9", "H")["H"])),

    mode.getresult("neff", "index")['index_y']
    )
```

```
                    #End of Functions
#-------------------------------------------------------------------------
#-------------------------------------------------------------------------
#-------------------------------------------------------------------------
#-------------------------------------------------------------------------
#-------------------------------------------------------------------------
#-------------------------------------------------------------------------



#--------------------Simulation Parameters-------------------------------
FreqPoints = 500

NumberOfLnws = 10
MaxLnw = 40

NumberOfWnws = 6
MaxWnw = 5

nanowire_mat = "NbN␣n_k␣"

#--------------------Array Intisilasaion ---------------------------------
WidthValueArray = np.linspace(0,MaxWnw, NumberOfWnws)

print('WidthValueArray', WidthValueArray)


LengthValueArray = np.linspace(0,MaxLnw,  NumberOfLnws)

print('LengthValueArray', LengthValueArray)
Transmission = np.zeros((NumberOfLnws,NumberOfWnws+1,9,FreqPoints))

power = np.zeros((NumberOfLnws,NumberOfWnws))
Lnws= np.zeros((NumberOfLnws,NumberOfWnws))
Wnws= np.zeros((NumberOfLnws,NumberOfWnws))

TEAttenCoefs = np.zeros((NumberOfLnws,NumberOfWnws))
TMAttenCoefs = np.zeros((NumberOfLnws,NumberOfWnws))
ReflectanceBS = np.zeros((NumberOfLnws,NumberOfWnws))


#--------------------Loops fpr Lnw and Wnw-------------------------------
for Lnw in range(0,NumberOfLnws):
    print(Lnw)
    for Wnw in range(0,NumberOfWnws):
        print(WidthValueArray[Wnw]*1e-7)

#-----------------------------------Simulation Input-----------------------------------------
        Data =WanveguideAndNanowireSim(frequency_points = FreqPoints,
        simulation_time = 5000e-15,
        mesh_accuracy = 8,
        Lnw= LengthValueArray[Lnw]*1e-6,
        Wnw= WidthValueArray[Wnw]*1e-7,
        Hnw = 4.7e-9,
```

```
        Nanowire_Material= nanowire_mat)
#-------------------------------------------------------------------
        p = float(Data[0])
        monitor1 = Data[1]
        monitor2 = Data[2]
        monitor3 = Data[3]
        monitor4 = Data[4]
        monitor5 = Data[5]
        monitor6 = Data[6]
        monitor7 = Data[7]
        monitor8 = Data[8]
        monitor9 = Data[9]


        Lambda = Data[10]

        Transmission[Lnw][Wnw][0] = monitor1
        Transmission[Lnw][Wnw][1] = monitor2
        Transmission[Lnw][Wnw][2] = monitor3
        Transmission[Lnw][Wnw][3] = monitor4
        Transmission[Lnw][Wnw][4] = monitor5
        Transmission[Lnw][Wnw][5] = monitor6
        Transmission[Lnw][Wnw][6] = monitor7
        Transmission[Lnw][Wnw][7] = monitor8
        Transmission[Lnw][Wnw][8] = monitor9


        power[Lnw,Wnw] = p

        Lnws[Lnw,Wnw] = LengthValueArray[Lnw]*1e-6
        Wnws[Lnw,Wnw] = WidthValueArray[Wnw]*1e-7


        TEAttenCoefs[Lnw, Wnw] = 10*np.log10((Data[11]**2)/(Data[12]**2))/(Lnw)
        TMAttenCoefs[Lnw, Wnw] = 10*np.log10((Data[13]**2)/(Data[14]**2))/(Lnw)

        neffabs=np.min(Data[15])
        neffwg= np.max(Data[15])
        print(neffabs, neffwg)
        ReflectanceBS[Lnw, Wnw] = 10*np.log10(np.absolute((neffwg-neffabs)/(neffabs+neffwg))**2)

    np.savetxt("ReflectanceBS"+ '_Lnw_'+ str(Lnw)+
    '_Wnw_'+ str(Wnw)+'_nanowire_' + nanowire_mat
    +'.csv', ReflectanceBS, delimiter=",")
    np.savetxt("TEAttenCoefsS"+ '_Lnw_'+ str(Lnw)+
    '_Wnw_'+ str(Wnw)+'_nanowire_' + nanowire_mat
    +'.csv', TEAttenCoefs, delimiter=",")
    np.savetxt("TMAttenCoef"+ '_Lnw_'+ str(Lnw)+
    '_Wnw_'+ str(Wnw)+'_nanowire_' + nanowire_mat
    +'.csv', TMAttenCoefs, delimiter=",")

    print(ReflectanceBS)
```

```
#------------------Atten Coef Plots-------------------------------
plt.plot(Wnws[4]*1e9, TEAttenCoefs[4], label = 'TE',marker='o')
plt.plot(Wnws[4]*1e9, TMAttenCoefs[4], label = 'TM',marker='o')

plt.legend()
plt.xlabel('Nanowire Width (nm)')
plt.ylabel('Attenuation Coefficent (dB/\u03bcm)')
plt.savefig("C:\\Users\\af15571\\OneDrive - University of Bristol\\MastersAttenuation_Coef_WaveAndNanoSim.png")
plt.show()


#------------------Reflectance Plots-------------------------------
plt.plot(Wnws[4]*1e9, ReflectanceBS[int(len(Wnws[0])/2)], label = 'TE',marker='o')

plt.title('Reflectance as a function of Nanowire Width')
plt.legend()
plt.xlabel('Nanowire Width (nm)')
plt.ylabel('Reflectance (db)')
plt.savefig("C:\\Users\\af15571\\OneDrive - University of Bristol\\Reflectance_WaveAndNanoSim.png")
plt.show()


#------------------Transmission Plots-------------------------------

MonNums = 9
TsAt1550 = np.zeros((NumberOfLnws, NumberOfWnws, MonNums))
XsOfMon = np.zeros((NumberOfLnws, NumberOfWnws, MonNums))
for Lnw in range(0,NumberOfLnws):
    for Wnw in range(0,NumberOfWnws):
        for MonNum in range(0,MonNums):

            TsAt1550[Lnw,Wnw,MonNum] = Transmission[Lnw,Wnw,MonNum][int(len(Transmission[1][1][0])/2)]
        XsOfMon[Lnw, Wnw] = np.linspace(0, (MaxLnw), MonNums)

for Wnw in range(1,NumberOfWnws):
    plt.plot(XsOfMon[4][Wnw]*1e6, TsAt1550[4][Wnw]*100, label = str(np.round(Wnws[0,Wnw]*1e6,1)) +' \u03bcm Wnw'
)
    plt.scatter(XsOfMon[4][Wnw]*1e6, TsAt1550[4][Wnw]*100 )

plt.legend()
plt.xlabel("Length of Nanowire (\u03bcm)")
plt.ylabel("Transmission (%)")
plt.axis((0, np.max(XsOfMon[4][Wnw]*1e6), 0, 100))
plt.savefig("C:\\Users\\af15571\\OneDrive - University of Bristol\\Transmission_WaveAndNanoSim.png")
plt.show()
```

A.2 Single and Multiple Rings

The following script was used to create all simulations of ring systems.

```
import imp
lumapi = imp.load_source("lumapi", "Path_to_lumapi/lumapi.py")
import numpy as np
import matplotlib.pyplot as plt
```

```
from scipy import interpolate
mode = lumapi.MODE()
result = mode.getresult()

gaps = [
# Insert Gaps to sweep through
]

Lnws = [
1e-6,
# Insert Lengths of gaps to sweep through
]

#number of rings to be tested
rings_to_be_tested = [1,2,3]

"""
The following function builds, runs and save a ring simulation. The keyword arguments set out the parameters
of the simulation. These parameters include all relevant geometry of the ring (bend radius, coupling length, etc.),
as well as the nanowire (Height, Width, Length). The materials for the waveguides and are set as Silicon.
The materials for the nanowire can be set by kwarg. This will require the addition of the optical property
data the Lumerical materials database before running.

"""
def MultipleRingResSimulation(HeightOfStructure = 0.22e-6, # Waveguide height
                      WidthOfWaveguides = 0.5e-6,          # Waveguide Width
                      Wnw = 0.2e-6,                        # Nanowire width
                      Lnw = 1e-6,                          # Nanowire length
                      Hnw = 4e-9,                          # Nanowire Height
                      x_span = 60e-6,                      # Size of computational cell in x direction
                      Lc = 2e-6,                           # Coupling Lengths
                      radius = 3.1e-6,                     # Bend Raduis of the ring
                      gap = 2.5e-7,                        # Gap in the directional coupler
                      Nanowire_Material ="NbN (n_k) ",     # Nanowire Material
                      frequency_points = 100,              # Number of Frequency points
                      simulation_time = 1000e-15,          # Simulation Run time
                      mesh_accuracy = 3,                   # Relative mesh accuracy
                      number_of_rings = 3,                 # Number of rings
                      seperation = 10e-6                   # Seperation between rings

                      ):
    mode.switchtolayout()
    mode.selectall()
    mode.delete()

    base_width = WidthOfWaveguides

#___________________________________Simulation structures ___________________________________

    # BOX
    mode.addrect()
    mode.set("name","SiO2")
    mode.set("z", -5.11e-6)
    mode.set("x", x_span/2)
    mode.set("y", 0)
```

```
mode.set("x span", 600e-6)
mode.set("y span",40e-6)
mode.set("z span", 10e-6)
mode.set("material", "SiO2 (Glass) - Palik")

# The cubic Bezier curve. Used to construct the curves

m=0.55191502449
#Bus
mode.addwaveguide()
mode.set("z", 0)
mode.set("x", 0)
mode.set("y", 0)
mode.set("name", "bus")
mode.set("Base Width", WidthOfWaveguides)
mode.set("Base Height", HeightOfStructure)
mode.set("Base Angle", 90)

pole = np.array([[0,radius+gap+WidthOfWaveguides],[x_span,radius+gap+WidthOfWaveguides]])
mode.set("poles", pole)
mode.set("material", "Si (Silicon) - Palik")

#_____________________________The Rings_____________________________
for ring in range(number_of_rings):
    centre_to_centre = seperation + Lc+2*radius                    # Distance from one ring centre to another
    x_location = (2*ring*centre_to_centre+x_span)/2 -x_span/4       # Centre of the current ring
    px1 = radius*np.array([0,m,1,1])+Lc/2+x_location               # Poles for the curving waveguides
    py1 = radius*np.array([1,1,m,0])
    p1 = np.column_stack((px1,py1))
    px2 = radius*np.array([0,m,1,1])+Lc/2+x_location
    py2 = radius*np.array([-1,-1,-m,0])
    p2 = np.column_stack((px2,py2))
    px3 = radius*np.array([-1,-1,-m,0])-Lc/2+x_location
    py3 = radius*np.array([0,-m,-1,-1])
    p3 = np.column_stack((px3,py3))
    px4 = radius*np.array([-1,-1,-m,0])-Lc/2+x_location
    py4 = radius*np.array([0,m,1,1])
    p4 = np.column_stack((px4,py4))

    #Top straight waveguide
    mode.addwaveguide()
    mode.set("z", 0)
    mode.set("x", 0)
    mode.set("y", 0)
    mode.set("name", "InnerTop")
    mode.set("Base Width", WidthOfWaveguides)
    mode.set("Base Height",HeightOfStructure)
    mode.set("Base Angle", 90)
    pole = np.array([[-Lc/2+x_location,radius],[Lc/2+x_location,radius]])
    mode.set("poles", pole)
    mode.set("material", "Si (Silicon) - Palik")


    #Bottom (coupler) waveguide
    mode.addwaveguide()
```

```
mode.set("z", 0)
mode.set("x", 0)
mode.set("y", 0)
mode.set("name", "InnerBottom")
mode.set("Base Width", WidthOfWaveguides)
mode.set("Base Height", HeightOfStructure)
mode.set("Base Angle", 90)
pole = np.array([[-Lc/2+x_location,-radius],[Lc/2+x_location,-radius]])
mode.set("poles", pole)
mode.set("material", "Si (Silicon) - Palik")

#Four curves for the ring
mode.addwaveguide()
mode.set("z", 0)
mode.set("x", 0)
mode.set("y", 0)
mode.set("name", "Arc1")
mode.set("Base Width", WidthOfWaveguides)
mode.set("Base Height", HeightOfStructure)
mode.set("Base Angle", 90)
mode.set("poles", p1)
mode.set("material", "Si (Silicon) - Palik")

mode.addwaveguide()
mode.set("z", 0)
mode.set("x", 0)
mode.set("y", 0)
mode.set("name", "Arc2")
mode.set("Base Width", WidthOfWaveguides)
mode.set("Base Height", HeightOfStructure)
mode.set("Base Angle", 90)
mode.set("poles", p2)
mode.set("material", "Si (Silicon) - Palik")

mode.addwaveguide()
mode.set("z", 0)
mode.set("x", 0)
mode.set("y", 0)
mode.set("name", "Arc3")
mode.set("Base Width", WidthOfWaveguides)
mode.set("Base Height", HeightOfStructure)
mode.set("Base Angle", 90)
mode.set("poles", p3)
mode.set("material", "Si (Silicon) - Palik")

mode.addwaveguide()
mode.set("z", 0)
mode.set("x", 0)
mode.set("y", 0)
mode.set("name", "Arc4")
mode.set("Base Width", WidthOfWaveguides)
mode.set("Base Height", HeightOfStructure)
mode.set("Base Angle", 90)
mode.set("poles", p4)
mode.set("material", "Si (Silicon) - Palik")
```

```
        #Nanowire
        mode.addrect()
        mode.set("name", "nanowire")
        mode.set("x span",Lnw )
        mode.set("y span",Wnw )
        mode.set("z span", Hnw)
        mode.set("x", x_location)
        mode.set("y", -radius  )
        mode.set("z", HeightOfStructure/2+Hnw/2)
        mode.set("material", Nanowire_Material)

#_____________________________________Solvers and Sources_____________________________________


    #varFDTD mesh and solver region
    mode.addvarfdtd()
    mode.set("mesh accuracy", mesh_accuracy)
    mode.set("simulation time", simulation_time)
    mode.set("x",x_span/2)
    mode.set("x span",x_span)
    mode.set("y",0)
    mode.set("y span",x_span/3)
    mode.set("z",0)
    mode.set("z span",0.3e-6)


    #Source
    mode.addmodesource()
    mode.set("x", 0e-6)
    mode.set("y", radius+gap+WidthOfWaveguides)
    mode.set("y span", 3e-6)
    mode.set("wavelength start", 1.520e-6)
    mode.set("wavelength stop", 1.580e-6)
    mode.setactivesolver('varFDTD')
    mode.addprofile()

#_____________________________________Monitors_____________________________________
    #Profile field monitor
    mode.set("name", "Profile")
    mode.set("x", x_span/2)
    mode.set("y", 0)
    mode.set("y span", x_span/3)
    mode.set("x span", x_span)

    #Through monitor (through the coupling region)
    mode.addpower()
    mode.set("override global monitor settings", True)
    mode.set("frequency points", frequency_points)
    mode.set("name", "Through")
    mode.set("x span", 0)
    mode.set("y span", 3e-6)
```

```
    mode.set("y", radius+gap+WidthOfWaveguides)
    mode.set("x", x_span/2)

    # Out monitor (out of the system, far end of the bus from the source)
    mode.addpower()
    mode.set("override global monitor settings", True)
    mode.set("frequency points", frequency_points)
    mode.set("name", "Out")
    mode.set("x span", 0)
    mode.set("y span", 3e-6)
    mode.set("y", radius+gap+base_width)
    mode.set("x", x_span)

#_____________________________________Save and run_____________________________________
    mode.save("RingRes_st"+str(simulation_time)+
                "_ma"+str(mesh_accuracy)+
                "_Gap"+str(np.round(gap, 2))+
                "_Lnw"+str(np.round(Lnw, 2))+
                "_Wnw"+str(np.round(Wnw, 2)))
    mode.run()
    mode.save("RingRes_st"+str(simulation_time)+
                "_ma"+str(mesh_accuracy)+
                "_Gap"+str(np.round(gap, 2))+
                "_Lnw"+str(np.round(Lnw, 2))+
                "_Wnw"+str(np.round(Wnw,2)))

    return result("Profile","E"), result("Out","T"),  result('Out', 'P'), result('Through', 'T'), result('Through', 'E')

x = np.zeros((1,1))
y = np.zeros((1,1))

nanowire_mat = "NbN (n_k) "
minTrans = []

#_____________________________________Loop for the sweep by rings and Lnw_____________________________________
for ring_number in rings_to_be_tested:
    for i in range(len(Lnws)):
        gap = gaps[i]
        Lnw = Lnws[i]

        ProfileE, OutT, OutP, ThroughT, ThroughE = MultipleRingResSimulation(
                            frequency_points = 4000,
                            simulation_time = 60000e-15,
                            mesh_accuracy = 1,
                            gap=  gap,
                            Lnw= Lnw,
                            radius= 10e-6,
                            Lc= 10e-6,
                            x_span= 180e-6,
                            Wnw= 0.4e-6,
                            number_of_rings= ring_number,
                            Nanowire_Material= nanowire_mat,
                            Hnw= 4.7e-9
                            )
```

```
        #_____________________________Colour map of E field_____________________________
        x  = ProfileE["x"]*1e6 # data on uniform grid, convert m to um
        y  = ProfileE["y"]*1e6 # data on uniform grid, convert m to um
        Ex = ProfileE["E"][:,:,0,0,0] # data on uniform grid, selecting the x-component of first frequency
        Ex_abs = abs(Ex)
        xi = np.linspace(np.amin(x),np.amax(x),len(x))
        yi = np.linspace(np.amin(y),np.amax(y),len(y))
        f= interpolate.interp2d(y,x,Ex_abs)
        Exi_abs = f(yi, xi)
        imageE = np.transpose(Exi_abs)
        print(ProfileE)

        plt.imshow(imageE,interpolation="bicubic", aspect='equal')
        plt.savefig('colourmap_gap'+str(ring_number)+'_lnw'+str(Lnw)+ '.pdf')
        plt.show()
        plt.close()



        #_____________________________Transmission Spectra_____________________________
        plt.plot(OutT['lambda']*1e6,10*np.log10(OutT['T']), label="Rings = " + str(ring_number) + " m ")
        plt.title('Transmission for  ' + str(ring_number)+' rings')
        plt.xlabel('Wavelength')
        plt.ylabel('Transmission')
        Wavelength = np.array(OutT['lambda']*1e6)
        Transdb = np.array(10*np.log10(OutT['T']))
        minTrans.append(min(Transdb))
        np.savetxt("Wavelength_ring"+ str(ring_number)
        + '_Lnw_'+ str(Lnw) +'_nanowire_' + nanowire_mat +'.csv', Wavelength, delimiter=",")
        np.savetxt("Transmission_ring"+ str(ring_number) + '_Lnw_'+ str(Lnw) +'.csv', Transdb, delimiter=",")

        print( "Nanowire Length", Lnw, "Min Transmission (%)", np.amin(OutT['T']), "Gap")
        type(ProfileE)
        x = np.append(x,float(Lnw))
        y = np.append(y, float(np.amin(OutT['T'])))

plt.legend()
plt.savefig('TransmissionVwavelength_'
+str(ring_number)+'Lnw'+str(Lnw)+".png")
plt.close()
np.savetxt("Multiple_rings_gap_min"+ '_Lnw_'+
str(Lnw)+'_nanowire_' + nanowire_mat +'.csv',
np.array(minTrans), delimiter=",")
```

BIBLIOGRAPHY

[1] H. Häffner, C. F. Roos, and R. Blatt.
Quantum computing with trapped ions, dec 2008.

[2] M. Saffman.
Quantum computing with atomic qubits and Rydberg interactions: Progress and challenges, oct 2016.

[3] G. Wendin.
Quantum information processing with superconducting circuits: A review, sep 2017.

[4] T. D. Ladd, F. Jelezko, R. Laflamme, Y. Nakamura, C. Monroe, and J. L. O'Brien.
Quantum computers.
Nature, 464(7285):45–53, 2010.

[5] Hoi Kwong Lo, Marcos Curty, and Kiyoshi Tamaki.
Secure quantum key distribution, 2014.

[6] Philip Sibson, Jake E. Kennard, Stasja Stanisic, Chris Erven, Jeremy L. O'Brien, and Mark G. Thompson.
Integrated silicon photonics for high-speed quantum key distribution.
Optica, 4(2):172, feb 2017.

[7] Richard P Feynman.
Simulating Physics with Computers.
Technical Report 6, 1982.

[8] Michael A. Nielsen and Isaac L. Chuang.
Quantum Computation and Quantum Information: 10th Anniversary Edition.
Cambridge University Press, USA, 10th edition, 2011.

[9] Peter W Shor.
Polynomial-Time Algorithms for Prime Factorization and Discrete Logarithms on a Quantum Computer *.
Technical report.

[10] Lov K. Grover.
A fast quantum mechanical algorithm for database search.
In *Proceedings of the Twenty-Eighth Annual ACM Symposium on Theory of Computing*, STOC '96, page 212–219, New York, NY, USA, 1996. Association for Computing Machinery.

[11] Austin G Fowler, Matteo Mariantoni, John M Martinis, and Andrew N Cleland.
Surface codes: Towards practical large-scale quantum computation.
Physical Review A, 86(3):32324, sep 2012.

[12] Richard Soref.
The past, present, and future of silicon photonics.
IEEE Journal on Selected Topics in Quantum Electronics, 12(6):1678–1687, nov 2006.

[13] Jeremy L O'brien.
Optical Quantum Computing.
Technical report.

[14] Paul G Kwiat, Andrew J Berglund, and Joseph B Altepeter.
Experimental Verification of Decoherence-Free Subspaces.
290(October):498–502, 2000.

[15] JL O'Brien, GJ Pryde, AG White, TC Ralph, and D Branning.
Demonstration of an all-optical quantum controlled-not gate.
Nature, 426 (6964):264 – 267, November 2003.
Publisher: Nature Publishing Group.

[16] E Knill, R Laflamme, and G Milburn.
A scheme for efficient quantum computation with linear optics.
Nature, 409:46–52, 02 2001.

[17] G.T. Reed and A.P. Knights.
Silicon Photonics: An Introduction.
Wiley, 2004.

[18] Nobuyuki Matsuda, Peter Karkus, Hidetaka Nishi, Tai Tsuchizawa, William J. Munro, Hiroki Takesue, and Koji Yamada.
On-chip generation and demultiplexing of quantum correlated photons using a silicon-silica monolithic photonic integration platform.
Optics Express, 22(19):22831, 2014.

[19] Jianwei Wang, Alberto Santamato, Pisu Jiang, Damien Bonneau, Erman Engin, Joshua W. Silverstone, Matthias Lermer, Johannes Beetz, Martin Kamp, Sven Höfling, Michael G. Tanner, Chandra M. Natarajan, Robert H. Hadfield, Sander N. Dorenbos, Val Zwiller, Jeremy L. O'Brien, and Mark G. Thompson.
Gallium arsenide (GaAs) quantum photonic waveguide circuits.
Optics Communications, 327(April):49–55, 2014.

[20] Caterina Taballione, Tom A.W. Wolterink, Jasleen Lugani, Andreas Eckstein, Bryn A. Bell, Robert Grootjans, Ilka Visscher, Jelmer J. Renema, Dimitri Geskus, Chris G.H. Roeloffzen, Ian A. Walmsley, Pepijn W.H. Pinkse, and Klaus J. Boller.
8×8 Programmable Quantum Photonic Processor Based on Silicon Nitride Waveguides.
Optics InfoBase Conference Papers, Part F114-FIO 2018(19):22–24, 2018.

[21] J. P. Sprengers, A. Gaggero, D. Sahin, S. Jahanmirinejad, G. Frucci, F. Mattioli, R. Leoni, J. Beetz, M. Lermer, M. Kamp, S. Hfling, R. Sanjines, and A. Fiore.
Waveguide superconducting single-photon detectors for integrated quantum photonic circuits.
Applied Physics Letters, 99(18), October 2011.

[22] Kevin K. Lee, Desmond R. Lim, Hsin Chiao Luan, Anuradha Agarwal, James Foresi, and Lionel C. Kimerling.
Effect of size and roughness on light transmission in a Si/SiO2 waveguide: Experiments and model.
Applied Physics Letters, 77(11):1617–1619, sep 2000.

[23] Joshua W. Silverstone, Damien Bonneau, Jeremy L. O'Brien, and Mark G. Thompson.
Silicon Quantum Photonics.
jul 2017.

[24] R. Dekker, N. Usechak, M. Först, and A. Driessen.
Ultrafast nonlinear all-optical processes in silicon-on-insulator waveguides.
Journal of Physics D: Applied Physics, 40(14), 2007.

[25] Edward D Palik.
Handbook of optical constants of solids.
Academic Press, Orlando SE - xviii, 804 pages : illustrations ; 25 cm., 1985.

[26] J. Komma, C. Schwarz, G. Hofmann, D. Heinert, and R. Nawrodt.
Thermo-optic coefficient of silicon at 1550 nm and cryogenic temperatures.
Applied Physics Letters, 101(4), 2012.

[27] Stewart A. Clark, Brian Culshaw, Emma J.C. Dawnay, and Ian E. Day.
Thermo-optic phase modulators in SIMOX material.
In Giancarlo C. Righini and Seppo Honkanen, editors, *Integrated Optics Devices IV*, volume 3936, pages 16 – 24. International Society for Optics and Photonics, SPIE, 2000.

[28] C M Wilkes, X Qiang, J Wang, R Santagati, S Paesani, X Zhou, D A B Miller, G D Marshall, M G Thompson, and J L O'Brien.
60 dB high-extinction auto-configured Mach–Zehnder interferometer.
Opt. Lett., 41(22):5318–5321, nov 2016.

[29] R Foord, R Jones, C J Oliver, and E R Pike.
The Use of Photomultiplier Tubes for Photon Counting.
Appl. Opt., 8(10):1975–1989, oct 1969.

[30] G. S. Buller and R. J. Collins.
Single-photon generation and detection, 2010.

[31] Chandra M. Natarajan, Michael G. Tanner, and Robert H. Hadfield.
Superconducting nanowire single-photon detectors: Physics and applications, jun 2012.

[32] G. N. Gol'tsman, O. Okunev, G. Chulkova, A. Lipatov, A. Semenov, K. Smirnov, B. Voronov, A. Dzardanov, C. Williams, and Roman Sobolewski.
Picosecond superconducting single-photon optical detector.
Applied Physics Letters, 79(6):705–707, 2001.

[33] M. D. Eisaman, J. Fan, A. Migdall, and S. V. Polyakov.
Invited Review Article: Single-photon sources and detectors, jul 2011.

[34] Simone Ferrari, Carsten Schuck, and Wolfram Pernice.
Waveguide-integrated superconducting nanowire single-photon detectors.
Nanophotonics, 7(11):1725–1758, 2018.

[35] Lu Zhang, Lixing You, Xiaoyan Yang, Junjie Wu, Chaolin Lv, Qi Guo, Weijun Zhang, Hao Li, Wei Peng, Zhen Wang, and Xiaoming Xie.
Hotspot relaxation time of NbN superconducting nanowire single-photon detectors on various substrates.
Scientific Reports, 8(1), dec 2018.

[36] Nicola A. Tyler, Jorge Barreto, Gerardo E. Villarreal-Garcia, Damien Bonneau, Döndü Sahin, Jeremy L. O'Brien, and Mark G. Thompson.
Modelling superconducting nanowire single photon detectors in a waveguide cavity.
Optics Express, 24(8):8797, 2016.

[37] Dondu Sahin, Alessandro Gaggero, Jan Willem Weber, Ivan Agafonov, Marcel A. Verheijen, Francesco Mattioli, Johannes Beetz, Martin Kamp, Sven Hofling, Mauritius C.M. Van De Sanden, Roberto Leoni, and Andrea Fiore.
Waveguide nanowire superconducting single-photon detectors fabricated on GaAs and the study of their optical properties.
IEEE Journal of Selected Topics in Quantum Electronics, 21(2), mar 2015.

[38] Xiaoyan Yang, Lixing You, Lu Zhang, Chaolin Lv, Hao Li, Xiaoyu Liu, Hui Zhou, and Zhen Wang.
Comparison of superconducting nanowire single-photon detectors made of NbTiN and NbN thin films.
IEEE Transactions on Applied Superconductivity, 28(1):26–31, 2018.

[39] J. Chiles, S. M. Buckley, A. Lita, V. B. Verma, J. Allmaras, B. Korzh, M. D. Shaw, J. M. Shainline, R. P. Mirin, and S. W. Nam.
Superconducting microwire detectors based on WSi with single-photon sensitivity in the near-infrared.
Applied Physics Letters, 116(24):1–5, 2020.

[40] I. Charaev, Y. Morimoto, A. Dane, A. Agarwal, M. Colangelo, and K. K. Berggren.
Large-area microwire MoSi single-photon detectors at 1550 nm wavelength.
Applied Physics Letters, 116(24), 2020.

[41] Christian Maurer, Christoph Becher, Carlos Russo, Jürgen Eschner, and Rainer Blatt.
A single-photon source based on a single Ca+ ion.
New Journal of Physics, 6:1–19, jul 2004.

[42] Alberto Politi, Martin J Cryan, John G Rarity, Siyuan Yu, and Jeremy L O'Brien.
Silica-on-silicon waveguide quantum circuits.
Science (New York, N.Y.), 320(5876):646–649, may 2008.

[43] Charles Santori, Matthew Pelton, Glenn Solomon, Yseulte Dale, and Yoshihisa Yamamoto.
Triggered single photons from a quantum dot.
Physical Review Letters, 86(8):1502–1505, 2001.

[44] J B Christensen, J G Koefoed, K Rottwitt, and C J McKinstrie.
Engineering spectrally unentangled photon pairs from nonlinear microring resonators by pump manipulation.
Opt. Lett., 43(4):859–862, feb 2018.

[45] Andrew J Shields.
Semiconductor quantum light sources.
Nature Photonics, 1(4):215–223, 2007.

[46] Mateusz Piekarek, Damien Bonneau, Shigehito Miki, Taro Yamashita, Mikio Fujiwara, Masahide Sasaki, Hirotaka Terai, Michael G. Tanner, Chandra M. Natarajan, Robert H. Hadfield, Jeremy L. O'Brien, and Mark G. Thompson.
Passive high-extinction integrated photonic filters for silicon quantum photonics.
2016 Conference on Lasers and Electro-Optics, CLEO 2016, 42(4):815–818, 2016.

[47] Jay E. Sharping, Kim F. Lee, Mark A. Foster, Amy C. Turner, Bradley S. Schmidt, Michal Lipson, Alexander L. Gaeta, and Prem Kumar.
Generation of correlated photons in nanoscale silicon waveguides.
Optics Express, 14(25):12388, 2006.

[48] Nicholas C. Harris, Davide Grassani, Angelica Simbula, Mihir Pant, Matteo Galli, Tom Baehr-Jones, Michael Hochberg, Dirk Englund, Daniele Bajoni, and Christophe Galland.
Integrated source of spectrally filtered correlated photons for large-scale quantum photonic systems.
Physical Review X, 4(4):1–10, 2014.

[49] S. Signorini and L. Pavesi.
On-chip heralded single photon sources.
AVS Quantum Science, 2(4):041701, 2020.

[50] Lucia Caspani, Chunle Xiong, Benjamin J. Eggleton, Daniele Bajoni, Marco Liscidini, Matteo Galli, Roberto Morandotti, and David J. Moss.
Integrated sources of photon quantum states based on nonlinear optics.
Light: Science and Applications, 6(11):e17100–12, 2017.

[51] Diego Pérez-Galacho, Carlos Alonso-Ramos, Florent Mazeas, Xavier Le Roux, Dorian Oser, Weiwei Zhang, Delphine Marris-Morini, Laurent Labonté, Sébastien Tanzilli, Éric Cassan, and Laurent Vivien.
Optical pump-rejection filter based on silicon sub-wavelength engineered photonic structures.
Optics Letters, 42(8):1468, 2017.

[52] Dajian Liu, Hongnan Xu, Ying Tan, Yaocheng Shi, and Daoxin Dai.
Silicon photonic filters.
Microwave and Optical Technology Letters, (January):1–17, 2020.

[53] J. B. Christensen, J. G. Koefoed, K. Rottwitt, and C. J. McKinstrie.
Engineering spectrally unentangled photon pairs from nonlinear microring resonators through pump manipulation.
arXiv, 43(4):4–7, 2017.

[54] Cale M. Gentry, Omar S. Magaña-Loaiza, Mark T. Wade, Fabio Pavanello, Thomas Gerrits, Sen Lin, Jeffrey M. Shainline, Shellee D. Dyer, Sae Woo Nam, Richard P. Mirin, and Miloš A. Popović.
Monolithic source of entangled photons with integrated pump rejection.
2018 Conference on Lasers and Electro-Optics, CLEO 2018 - Proceedings, pages 3–4, 2018.

[55] Jun Rong Ong, Ranjeet Kumar, and Shayan Mookherjea.
Ultra-high-contrast and tunable-bandwidth filter using cascaded high-order silicon microring filters.
IEEE Photonics Technology Letters, 25(16):1543–1546, 2013.

[56] Marco Liscidini, J. E. Sipe, and L. G. Helt.
Continuous wave photon pair generation in silicon-on-insultator waveguides and ring resonators and erratum: comment.
Optics Express, 24(8):9130, 2016.

[57] Rakesh Ranjan Kumar, Xinru Wu, and Hon Ki Tsang.
Compact high-extinction tunable CROW filters for integrated quantum photonic circuits.
Optics Letters, 45(6):1289, 2020.

[58] Dorian Oser, Sébastien Tanzilli, Florent Mazeas, Carlos Alonso-Ramos, Xavier Le Roux, Grégory Sauder, Xin Hua, Oliver Alibart, Laurent Vivien, Éric Cassan, and Laurent Labonté.
High-quality photonic entanglement out of a stand-alone silicon chip.
npj Quantum Information, 6(1):1–6, 2020.

[59] Nicholas C. Harris, Christophe Galland, Daniele Bajoni, Mihir Pant, Davide Grassani, Tom Baehr-Jones, Michael Hochberg, and Dirk Englund.
On-chip heralded single photon source with demultiplexing and pump filtering.
Optics InfoBase Conference Papers, 2:3–4, 2014.

[60] Huiye Qiu, Jianfei Jiang, Ping Yu, Tingge Dai, Jianyi Yang, Hui Yu, and Xiaoqing Jiang.
Silicon band-rejection and band-pass filter based on asymmetric Bragg sidewall gratings in a multimode waveguide.
Optics Letters, 41(11):2450, 2016.

[61] Giuseppe Cantarella, Charalambos Klitis, Marc Sorel, and Michael J. Strain.
Silicon photonic filters with high rejection of both TE and TM modes for on-chip four wave mixing applications.
Optics Express, 25(17):19711, 2017.

[62] Giuseppe Brunetti, Nicola Sasanelli, Mario N. Armenise, and Caterina Ciminelli.
High performance and tunable optical pump-rejection filter for quantum photonic systems.
Optics and Laser Technology, 139:106978, 2021.

[63] W. Bogaerts, P. de Heyn, T. van Vaerenbergh, K. de Vos, S. Kumar Selvaraja, T. Claes, P. Dumon, P. Bienstman, D. van Thourhout, and R. Baets.
Silicon microring resonators.
Laser and Photonics Reviews, 6(1):47–73, 2012.

[64] L Vivien and L Pavesi.
Handbook of Silicon Photonics.
Series in Optics and Optoelectronics. Taylor & Francis, 2013.

[65] Ardavan F. Oskooi, David Roundy, Mihai Ibanescu, Peter Bermel, J. D. Joannopoulos, and Steven G. Johnson.
Meep: A flexible free-software package for electromagnetic simulations by the FDTD method.
Computer Physics Communications, 181(3):687–702, mar 2010.

[66] Mack Johnson.
Low Q-factor Silicon Photonic Cavities for Optical Filtering and Single-Photon Detection.
PhD thesis, 2019.

[67] M Bachmann, P A Besse, and H Melchior.
Overlapping-image multimode interference couplers with a reduced number of self-images for uniform and nonuniform power splitting.
Appl. Opt., 34(30):6898–6910, oct 1995.

[68] D. G. (Dominik G.) Rabus.
Integrated ring resonators : the compendium.
Springer, 2007.

[69] G. Lifante.
Integrated Photonics: Fundamentals.
Wiley, 2003.

[70] E A J Marcatili.
Dielectric Rectangular Waveguide and Directional Coupler for Integrated Optics.
Bell System Technical Journal, 48(7):2071–2102, 1969.

[71] Arun Kumar, K Thyagarajan, and A K Ghatak.
Analysis of rectangular-core dielectric waveguides: an accurate perturbation approach.
Opt. Lett., 8(1):63–65, jan 1983.

[72] Chin Yi Tsai.
Interband and Intraband Absorption Coefficients of Silicon: Theoretical Frameworks and Formulations.
IEEE Journal of Selected Topics in Quantum Electronics, 26(2), 2020.

[73] Dan-Xia Xu, Pavel Cheben, Andre Delâge, Siegfried Janz, Boris Lamontagne, Edith Post, and Winnie N Ye.
Polarization-insensitive MMI-coupled ring resonators in silicon-on-insulator using cladding stress engineering.
In Joel A Kubby and Graham T Reed, editors, *Silicon Photonics II*, volume 6477, pages 92–102. International Society for Optics and Photonics, SPIE, 2007.

[74] Robert G. Hunsperger.
Integrated optics: Theory and technology: Sixth edition.
Springer US, 2009.

[75] Weiping Huang.
Coupled-Mode Theory.
pages 1505–1518, 1991.

[76] J. Heebner, R. Grover, and T. Ibrahim.
Optical Microresonators: Theory, Fabrication, and Applications.
Springer Series in Optical Sciences. Springer New York, 2007.

[77] Jian Li, Robert A. Kirkwood, Luke J. Baker, David Bosworth, Kleanthis Erotokritou, Archan Banerjee, Robert M. Heath, Chandra M. Natarajan, Zoe H. Barber, Marc Sorel, and Robert H. Hadfield.
Nano-optical single-photon response mapping of waveguide integrated molybdenum silicide (MoSi) superconducting nanowires.
Optics Express, 24(13):13931, 2016.

[78] Joaquin Matres and Wayne V. Sorin.
Simple model for ring resonators backscatter.
Optics Express, 25(4):3242, feb 2017.

[79] Kane Yee.
Numerical solution of initial boundary value problems involving maxwell's equations in isotropic media.
IEEE Transactions on Antennas and Propagation, 14(3):302–307, 1966.

[80] Lumerical.
Lumerical Inc.
page https://www.lumerical.com/products.

[81] Dennis M Sullivan.
Electromagnetic simulation using the FDTD method.
John Wiley & Sons, 2013.

[82] Allen Taflove, Steven G Johnson, and Ardavan Oskooi.
Advances in FDTD Computational Electrodynamics: Photonics and Nanotechnology.
(May), 2013.

[83] Allen Taflove and Susan C. Hagness.
Computational Electrodynamics: The FDTD Method (2nd Ed.).
(June 2000):439, 2000.

[84] Robert Lee, David Kingsland, and Jin Fa Lee.
A Perfectly Matched Anisotropic Absorber for Use as an Absorbing Boundary Condition.
IEEE Transactions on Antennas and Propagation, 43(12):1460–1463, 1995.

[85] Manfred Hammer and Olena V. Ivanova.
Effective index approximations of photonic crystal slabs: A 2-to-1-D assessment.
Optical and Quantum Electronics, 41(4):267–283, 2009.

[86] A.W. Snyder and J. Love.
Optical Waveguide Theory.
Springer US, 2012.

[87] Archan Banerjee, Robert M. Heath, Dmitry Morozov, Dilini Hemakumara, Umberto Nasti, Iain Thayne, and Robert H. Hadfield.
Optical properties of refractory metal based thin films.
Optical Materials Express, 8(8):2072, 2018.

[88] A. Samarelli, D. S. Macintyre, M. J. Strain, R. M. De La Rue, M. Sorel, and S. Thoms.
Optical characterization of a hydrogen silsesquioxane lithography process.
Journal of Vacuum Science Technology B: Microelectronics and Nanometer Structures, 26(6):2290–2294, 2008.

[89] Giuseppe Cantarella, Charalambos Klitis, Marc Sorel, and Michael J. Strain.
Integrated microrings for on-chip filtering and efficient FWM generation.
2016 Photonics North, PN 2016, 16(7):7948, 2016.

[90] Fengnian Xia, Mike Rooks, Lidija Sekaric, and Yurii Vlasov.
Ultra-compact high order ring resonator filters using submicron silicon photonic wires for on-chip optical interconnects.
Optics Express, 15(19):11934, 2007.

[91] Logan Su, Dries Vercruysse, Jinhie Skarda, Neil V. Sapra, Jan A. Petykiewicz, and Jelena Vučković.
Nanophotonic inverse design with SPINS: Software architecture and practical considerations.
Applied Physics Reviews, 7(1), 2020.